JAERI-M
91-170

JAERI TANDEM, LINAC & V.D.G. ANNUAL REPORT 1990

April 1, 1990 – March 31, 1991

October 1991

Department of Physics

日本原子力研究所
Japan Atomic Energy Research Institute

JAERI-Mレポートは，日本原子力研究所が不定期に公刊している研究報告書です。
入手の問合わせは，日本原子力研究所技術情報部情報資料課（〒319－11茨城県那珂郡東海村）あて，お申しこしください。なお，このほかに財団法人原子力弘済会資料センター（〒319-11茨城県那珂郡東海村日本原子力研究所内）で複写による実費頒布をおこなっております。

JAERI-M reports are issued irregularly.
Inquiries about availability of the reports should be addressed to Information Division, Department of Technical Information, Japan Atomic Energy Research Institute, Tokai-mura, Naka-gun, Ibaraki-ken 319-11, Japan.

編集兼発行　日本原子力研究所
印　　刷　日立高速印刷株式会社

JAERI-M 91-170

JAERI TANDEM, LINAC & V.D.G.
Annual Report
1990

April 1, 1990 - March 31, 1991

Department of Physics
Tokai Research Establishment
Japan Atomic Energy Research Institute
Tokai-mura, Naka-gun, Ibaraki-ken

(Received October 1, 1991)

This annual report describes research activities which have been performed with the JAERI tandem accelerator, the electron linear accelerator and the Van de Graaff accelerator from April 1, 1990 to March 31, 1991. Summary reports of 38 papers, and list of publications, personnel and cooperative researches with universities are contained.

Keywords : JAERI TANDEM, e-LINAC, V.D.G., Atomic Physics, Solid State Physics, Radiation Ettects in Materials, Nuclear Chemistry, Nuclear Physics, Neutron Physics

Editors : Mitsuhiko Ishii
Chiaki Kobayashi
Akira Iwamoto
Yukio Kazumata
Yuuki Kawarasaki
Fujiyasu Nomura

JAERI－M 91－170

原研タンデム，リニアック，バンデグラフ加速器 1990年度年次報告

日本原子力研究所東海研究所
物理部

（1991年10月1日受理）

本年次報告は，原研タンデム，リニアック及びバンデグラフ加速器で，1990年4月1日から1991年3月31日までの間に東海研で行われた研究活動をとりまとめたものである。

1）加速器運転と開発研究　2）固体物理及び材料の放射線効果　3）原子物理　4）核化学　5）核物理　6）中性子物理の6部門にまたがる38編の研究報告，公表された文献，関与した職員及び大学等との協力研究のリストを収録している。

東海研究所：〒319-11　茨城県那珂郡東海村白方字白根2-4
（編集者）石井三彦，小林千明，岩本　昭，数又幸生
河原崎雄紀，野村藤靖

PREFACE

This report covers research and development activities during the period April 1, 1990 until March 31, 1991 at the accelerator facilities of JAERI, Tokai : the 20UR tandem accelerator, the 2 MeV V.d.G. accelerator and the 200 MeV electron linear accelerator.

During this period, the tandem accelerator, the main facility of the three, has been operated over 4,700 hours and has supplied stable beams to experiments in the fields of : (1) Solid State Physics and Radiation Effects in Materials, (2) Atomic Physics, (3) Nuclear Chemistry, (4) Nuclear Physics and (5) Neutron Physics. Fifty three experimental programs have been carried out in collaboration with universities and industries; more than sixty individuals outside JAERI have worked with about sixty members of JAERI staff.

The superconducting-booster has continued to be constructed on schedule. Twelve superconducting cavities have reached the stage of electrochemical polishing and RF-power test. A new building for the tandem booster has been under construction and will be completed in December 1991. Installation of the tandem booster and helium refrigerators will start in January 1992, aiming at generating first beams in early 1993.

A seminar on application of accelerators to atomic and condensed matter physics was held on January 22-23, 1991 at JAERI, Tokai. Participants over fifty took part in it and discussed experimental results and related topics, some of which are presented in this report. The details of the seminar will be published in JAERI-M Report. Also the second workshop for instrumentation for the tandem-booster was held on February 28 - March 1, 1991 at JAERI, Tokai. Forty three participants, including twenty five from universities, talked about future experimental programs and instruments required for them. The activities of the workshop have been published in JAERI-M 91-115.

M. Ishii

Mitsuhiko Ishii
Deputy Director
Department of Physics

Contents

I ACCELERATOR OPERATION AND DEVELOPMENT

1.1 TANDEM ACCELERATOR OPERATION

Tandem Accelerator Group

Department of physics, JAERI

Accelerator operation

The scheduled operation for experiments was performed through the past one year containing three short periods for the scheduled maintenance.

The accelerator has run smoothly and almost all of the experimental programs were performed. The following are summary of the operation from April 1,1990 to March 31,1991. The accelerator running time was 4774.8 hours.

1) Time distribution by terminal voltage

>17 MV	0 days	0.0 %	11-12 MV	0 days	0.0 %
16-17	63	31.3	10-11	6	3.0
15-16	67	33.3	9-10	9	4.5
14-15	20	10.0	8- 9	2	1.0
13-14	17	8.5	< 8	0	0.0
12-13	17	8.5			

2) Time distribution by projectile

H	18 days	9.0 %	S	11 days	5.5 %
D	18	9.0	Cl	12	6.0
Li	3	1.5	Fe	3	1.5
B	5	2.5	Ni	34	17.0
C	8	4.0	Cu	2	1.0
O	35	17.4	Ge	11	5.5
F	15	7.5	Br	2	1.0
Si	14	7.0	Ag	3	1.5
P	1	0.5	I	5	2.5

3) Time distribution by activity

Operation for research	201 days
Atomic and solid state physics	(35 days)

Radiation effects in materials	(14	)
Nuclear chemistry	(33	)
Nuclear physics	(73	)
Fast neutron physics	(29	)
Radiation chemistry	(7	)
Detector development	(4	)
Accelerator development	(6	)
Voltage conditioning	22	
Operation training	4	
Scheduled maintenance (2 tank openings)	78	
Unexpected repair (1 tank opening)	7	
Holidays and vacation	53	

Troubles that interrupted the experimental schedule

1) Failure in the terminal electronics components due to full sparking (1 tank opening needed),
2) Instability of the GVM rotation due to the bearings break,
3) Failure in the negative ion injector.

Improvement and development

New control computer system that utilizes parallel processing method is under development. The old system will be renewed with the new system soon. The construction of the tandem booster is well under way as has been scheduled. Those two items will be reported later paragraph.

1.2 SUPERCONDUCTING BOOSTER

Booster Project Group

Department of Physics, JAERI

1. Introduction

The project of our superconducting tandem-booster was progressive in the fiscal year of 1990 also. Four of ten linac units of the booster with their control circuits have been manufactured and the rest six units have been in the works. The construction of the building has started. Orders for a refrigerating system and a sub-bunching unit composed of 260 MHz superconducting resonators have been placed with Mitsubishi Electric Corp.

Beam tests have been performed with existing two units, a buncher and a de-buncher, to examine a beam acceleration in combination with beam bunch phase detection.

Resonator performances were examined with four of the sixteen resonators of the four linac units.

2. Beam tests

We did beam acceleration tests using two units of buncher and de-buncher and a beam bunch phase detector. We used a resonator of the buncher for beam bunching and a resonator of the de-bunching unit for acceleration. They were separated 2.7 m apart. At 1.4 m downstream of the latter one, a normal conducting copper quarter wave resonator as a beam bunch phase detector was situated and followed by a scattering chamber with a Au target foil and a soild state particle detector for detection of energy and time spectra.

The tests were useful to find some difficulties in the units and to yield improvements to them and the construction of the linac.

From this experiment, we confirmed that the normal conducting quarter wave resonator is applicable to the beam bunch diagnostic system in the linac with enough sensitivities in amplitude and phase. In our plan, three beam bunch phase detectors will be installed in the linac. Two sets of energy and time measurement system composed of Au foils and

solid state particle detectors will be also placed at the entrance and the exit of the linac.

3. Booster linac system

The former four of the ten linac units were delivered to JAERI in the beginning of 1991 after two years long fabrication at Mitsubishi Electric Corp. Figure 1 shows one of the units opened out. Two booster control modules, each of which can operate 8 resonators and two cryostats, were also delivered from Applied Superconductivity Inc. in March 1991.

During the fabrication, preliminery resonator performance tests were performed with four resonators first fabricated. One of them had an accelerating field higher than 10 MV/m. Another one, however, had resonator Q as low as 1×10^8. The surface of its outer conductor was found to be covered with tiny white dirty-looking spots. In order to remove the spots, we had no other way than to mechanically polish the whole outer conductor surface and finish with electropolishing. The resonator Q was eventually improved to the level that we could satisfy. From various investigations, we judged that the problem was attributed to the final electropolishing in JAERI rather than to the fabrication processes in the industry. As a result, all the four resonators had levels higher than the acceptable performance of 5 MV/m with an rf input of 4 watts.

Resonator surface treatment and assembling work with the four linac units have started in March 1991. Four three-person assembling groups were organized and every one was assigned to a unit.

The fabrication of the rest six linac units are in progress in the industry without any serious problem. It is proceeding faster than originally expected.

Three out of nine quadrupole doublet lenses needed in the linac were fabricated this year. The rest six will be manufactured in the next year.

4. Bunching system

An addition of a 260 MHz sub-buncher to the 130 MHz main buncher will increase the bunching efficiency or beam intensity 3 or 4 fold. The design of 260 MHz superconducting quarter wave resonators was confirmed with a full-size copper model. The optimum beam velocity for the resonators is 0.1c as just the same as for the 130 MHz resonators. The sub-buncher will be composed of two of them and a cryostat. Order has been given so far.

5. Refrigerating system

We drew up the order specification according to the conclusion of design work done before. After a long contract negociation, the order was given to Mitsubishi Electric Corp. at nearly the end of this fiscal year. Cold boxes of Sulzer's Model TCF-50 will take part in the system. The components of the system will be fabricated in a year and the installation will start in early 1992 in the booster building.

6. Booster building

The full design was completed and the construction started in October 1990. After the building area was excavated, a concrete bottom was established in March 1991. Figure 2 shows a view of construction at that time. The building construction will be completed by the end of 1991. It will be ready to bring in and install the refrigerating system and the booster units at the very beginning of 1992.

One of the tandem target rooms, "Heavey Ion Target Room No.1", is to be a part of accelerator room of the booster. During the construction of the building and the booster, one can not use the room as a target room.

7. Others and future plans

The beam line components are to be prepared in the later part of the booster construction period because of budget consideration. Only an analyzing magnet as one of the biggest components is to be built in the next fiscal year.

With respect to the central control system for the booster, a new system for the tandem accelerator will take care of it also. The new

system is under development, introducing a new computer technology of paralell processing among multi-processors.

After the installation of the refrigerating system and the booster units, the whole system must be inspected as a qualified refrigerator unit by the administrative office of refrigerators by the end of the former half of the fiscal year of 1992. It will take nearly one year to accomplish further work; resonator treatments and assembling of the booster units, installation of beam line components and a run of individual and overall tests.

8. Staff of the project

The members who contributed to the work in the fiscal year of 1990 were as follows: C. Kobayashi, S. Takeuchi, T. Ishii, H. Ikezoe, B. Min, T. Yoshida, K. Ohkoshi, Y. Sugiyama, S. Kanazawa, M. Watanabe, S. Kikuchi, Y. Tomita, Y. Satoh, S. Hanashima, K. Horie, S. Kanda, Y. Tsukihashi, S. Abe, S. Tajima, S. Ichikawa, M. Ohshima and K. Ideno. One should notice that an engineering work section(Kosaku-ka) has been in cooperation for the fabrication of the booster units.

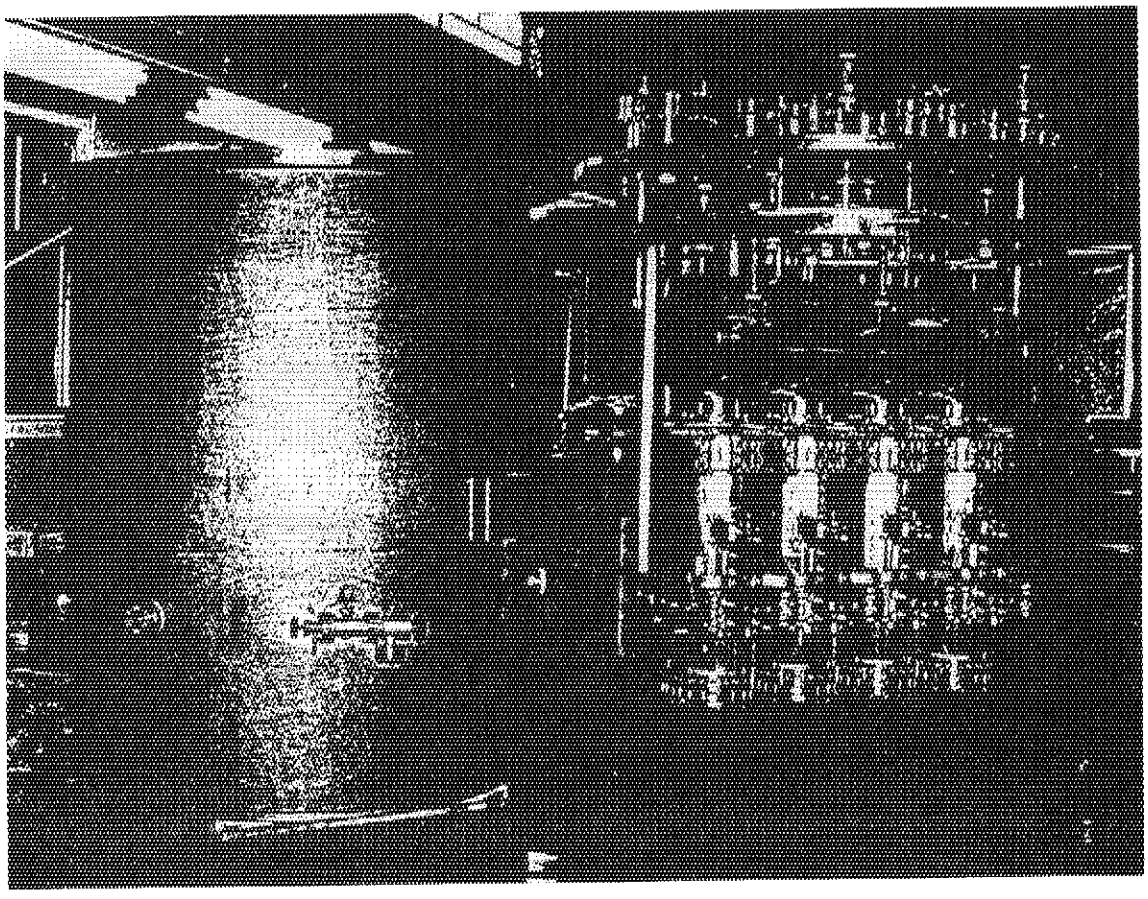

Fig. 1. A booster linac unit.

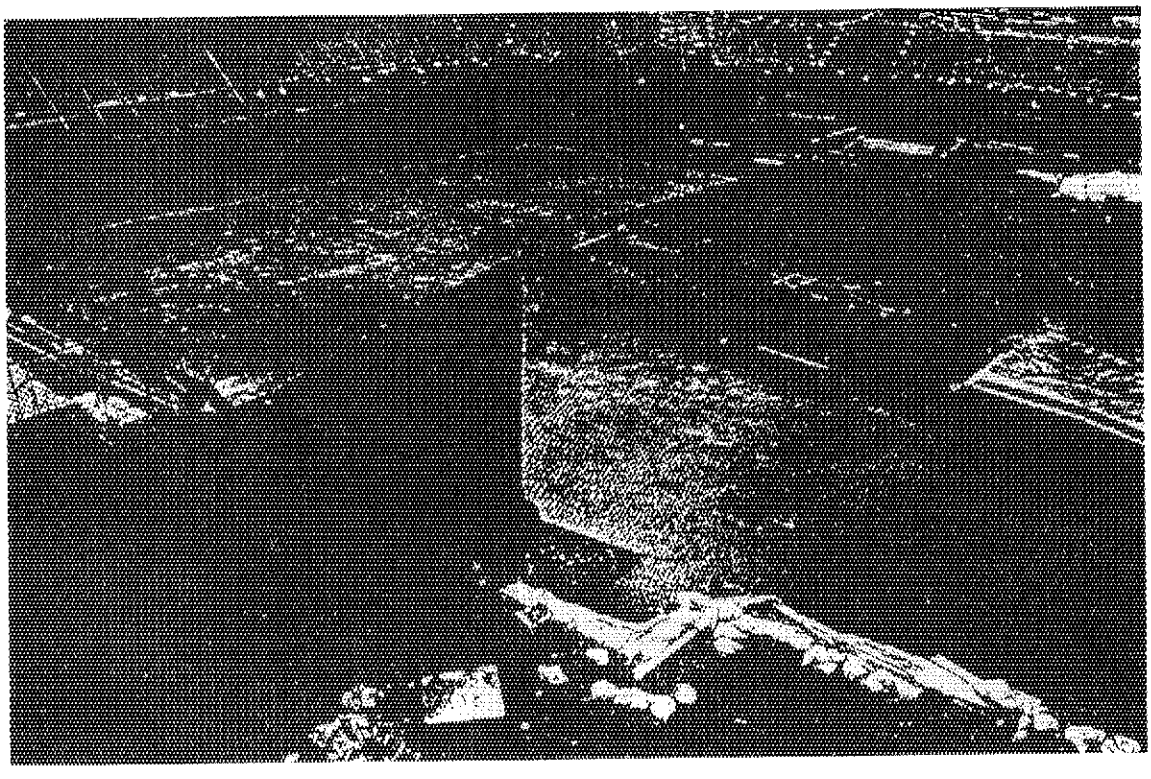

Fig. 2. Construction site of the booster building.

1.3 STATUS OF JAERI-LINAC

Katsuo MASHIKO, Tokio SHOJI, Nobuhiro ISHIZAKI,
Hidekazu TAYAMA and Hideaki YOKOMIZO*

Departments of Physics, JAERI,
*Office of Synchrotron Radiation Facility Project

Abstract

The JAERI 120 MeV electron linear accelerator (linac) was stably operated for the experimental researches with the 415.1 hour beam time from April, 1990 to the first week of August, 1990. The linac was, then, stopped due to the construction work for the extension of the linac building during the period from the third week of August to the end of March in 1991.

During this period, the linac group made various maintenance works for the electron gun, the accelerating structures, the beam transport system, the microwave pulse amplifier and the overhaul for all the electronic circuits. The linac is now being restored to the original performance by the middle of April, 1991.

The Office of Synchrotron Radiation Facility Projects (Spring-8 Office) has planned to expand the old linac building for the accelerator R&D works which will be carried out by the Accelerator Systems Development Group (Accelerator group). The construction of the steel-frame 706.34 m^2 building has been completed in March 10, 1991. The members of Accelerator group moved in the linac building by the end of March.

The office furnishings, experimental apparatuses, equipments and radioactive waste materials (about 5 ton) left in the old linac building were either disposed or moved.

1.Operation

The linac was stably operated for 415.1 hours with a repetition rate of less than 150 pps during the 1990 fiscal year from April, 1990 to the first week of August, 1990. A summary of the linac operating conditions is shown in Table 1 for each experimental program.

The linac was stopped for the building construction from the third week of August to the end of March in 1991 due to the radiation safety reason.

Research Program	Time (h)	Ratio (%)	Energy (MeV)	Rate (pps)	Length (ns)	Current (μA)
Neutron Radiography (Time of Flight Method)	104.9	25.3	120	150	25	12
Slow Positron Experiment (Emission of monoenergetic Positron)	54.0	13.0	100	50	1000	10
First Positron Experiment	75.0	18.1	~100	~25	1000	10
JSR Injection	147.4	35.5	~150	0.5~1	1000	<1
Tuning and Test Operation	33.8	8.1	100~180	50~150	1000	~30
Total	415.1	100.0				

Table 1 Machine Time and Output Beam for Research Program in 1990

note (a) Interval of the linac operation : April 1,1990 ~ August, 1990
(b) Interval of the linac shut down : August 6, 1990 ~ March 31,1991
(c) Neutron Cross Section discontinued : April, 1990 ~

2.Maintenance

The scheduled overhaul of the linac was carried out during the building construction period (August 6, 1990 to March 31, 1991).

Main items for the overhaul are the following:

(1)Electron gun

The new (home-made) electron gun system with the ceramics guide tube and the new type of cathode (EIMAC Y-796) was installed. The cathode pulse transformer (home-msde), a load resistor and the 900 l insulation oil in the tank were replaced and the average current circuit was repaired.

(2)Accelerating structure system

The beam transport systems connecting each accelerator structure were reassembled and realigned with new twelve quadrupole magnets. The following replacements in the various parts were made: vacuum elements for seven of the ion getter pumps, three of the RF windows for the wave guides, two of the 10 l/min ion getter pumps for the #4 and #5 waveguides.

The misalignment in the linac was found in the horizontal direction of maximum 2.5 mm and in the vertical direction of 1.5 mm. The major reasons for this misalignment were thought to be :(1) the looseness of bolts due to the thermal expansion and shrinking cycle caused by the large temperature change (5° - 45°C), (2) the shift of the position due to oscillation by earthquake, (3) setting errors for the individually replaced accelerator structures. The setting accuracy after the present alignment is estimated to be ± 0.1 mm.

(3) Beam transport system

The beam transport tubes for three directions, which are called as T_C (center (neutron) target), T_E (energy-analysis target) and T_R (right target), were disassembled and realigned with new five quadrupole magnets in the T_R and the magnetic steering coils for T_C and T_R. The bending magnet for the neutron target, T_C, the neutron target assembly and its cooling water pump were also replaced.

(4) Microwave pulse oscillator amplifier

The driver circuit of microwave pulse oscillator was sent to the manufacturing company and was repaired. The PFN circuit (home-made) of the cathode pulse for the Booster klystron was replaced and its RF output pulse shape was readjusted. The first stage RF phase shifters both for the buncher klystron and the #1 klystron were replaced with the new rotary type phase shifters.

3. Expansion for the linac building

The SPring-8 Office made the expansion of the building in order to prepare the spaces for the R&D works and performance tests for various parts of Synchrotrons Radiation Facility. The layout of the expanded building is shown in Fig. 1 which is located in the south of the old linac building.

The expanded building is constructed in the steel-frame structure with the whole area of 706.34 m^2. It has the experimental room #2 (the target room) of the area of 472.4 m^2 and the height of 11.8 m. The crane in the old linac building can also cover the newly constructed area. The maximum floor load is the same as the old part to be 10 ton/m^2. The 4 m wide × 3.8 m high large shutter is installed for bringing in large size apparatuses.

One unit of the pure water supply for cooling is prepared with the capacity of 234,000 kcal, 780 l/min. The electric power supply is three units of 100 kVA of 3 ϕ, 200 V system. The experimental area #1 consists of spaces of five spans.

4. Disposal of radioactive waste materials and the rearrangement of the office spaces.

The changes of the office arrangement and rearrangement of experimental equipments were made due to the expansion of the building and the change of the working staffs. Thirty three 200 l drum cans of radioactive waste materials (about 5 ton), thirty two carton boxes of incombustible materials and fifty five carton boxes of combustible wastes produced in the old linac building were disposed with the necessary formal procedures.

The staffs of Accelerator Group of SPring-8 Office have moved in the linac building before March 31, 1991. The Linac Group members of Accelerator Division, Department of Physics and the linac experimenters are also still sharing some office spaces in the building.

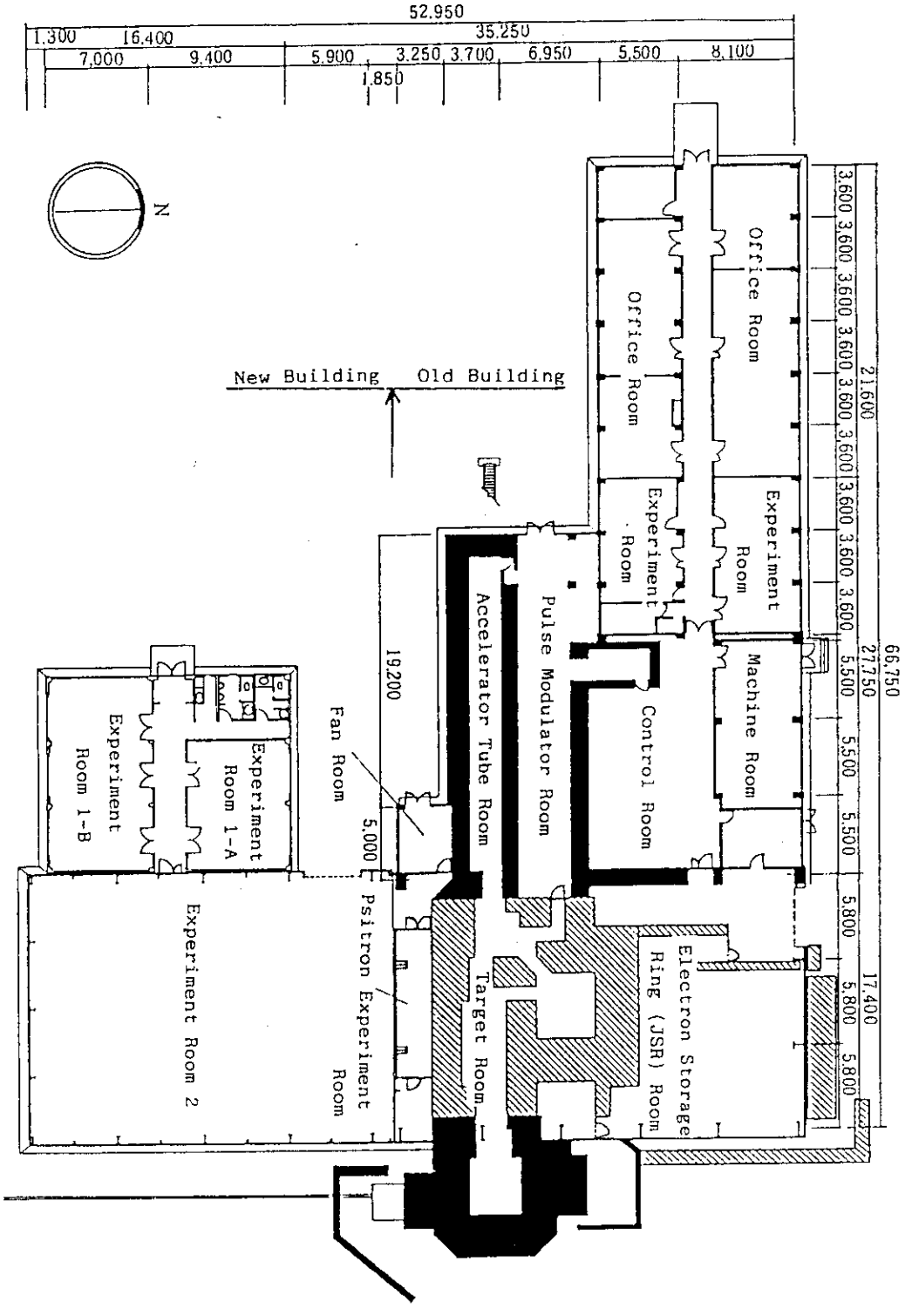

Fig. 1 The layout of the expanded building

Ⅱ SOLID STATE PHYSICS AND RADIATION EFFECTS IN MATERIALS

2.1 Evaluation of Dispersion of Heavy Ion Particles

Yoshihide KOMAKI, Niro ISHIKAWA, Tsutomu SAKURAI, Shigemi FURUNO, Hitoshi OHTSU, Katsutoshi FURUKAWA, Shinichi OHNO, Toshihito HIRUTA *, Koji TANUMA *, Masao FUKASAWA*, Kazuhiko IZUI**, and Tetsuo TSUKAMOTO***

Department of Chemistry, *Department of Engineering Services JAERI, **Nagasaki University, ***ORIGIN ELECTRIC Co.,Ltd.

Introduction

Heavy ion irradiation technology has been developed not only in the study of physical characteristics of damaged materials, but also in the creation of new materials by use of irradiation damage. Ion injection on the inorganic and the organic materials or functional polymeric membranes and heavy ion lithography are the typical examples. For these purposes it is important to evaluate the degree of dispersion of ion beams and the exact quantity of incident ions on the specimens.

The authors have studied the preparation of polymeric filters through the heavy ion irradiation followed by chemical etching[1),2)]. The number of holes in the membrane corresponds to that of the incident ion particles, the diameter of hole depending on the kinds of ions and the etching behavior. The uniformity of dispersion of ions and the control of the number of incident particles are important for preparation of the filters.

In general two methods are used for irradiating with ions over the wide area of the target. One is scanning ion beam over the fixed specimen and the other is driving the specimen across the fixed ion beam. Prior to the preparation of an apparatus for the latter method, the authors tried to evaluate the degree of dispersion and the uniformity of distribution of incident ion particls by measuring the defocused ion beam with the help of many micro Faraday cups (FC)set widely over the irradiation area and analysing the beam currents computationally.

Experimental apparatus

The apparatus consists of a detection system for the electric current produced by heavy ions, an linearly up and down driving system for the irradiation line, an image processing system for the measured ion current

and an electric remote control system as shown in Fig. 2. The detection system consists of assembly of 12 pieces of micro Faraday cups set in a ceramics(Makor)block, which has the same area as the irradiation area of 25 mm in diameter. In front of the multi FC, a suppressor made of stainless steel with 12 holes is placed to avoid scattering of secondary electrons, as shown in Fig. 1. Each cup of the multi FC system is connected to 12 preamplifiers respectively, and detects independently ion beam current.

In order to detect very small ion beam current without any noise, the preamplifiers are set rigidly with the multi FC system and a bundle of cable wires from the multi FCs to the preamplifiers is fixed in resin. The system consisting of the multi FCs and the preamplifiers moves linearly into the ion beam line by the distance of 40 mm in a bellows, when ion current is measured, and moves out of the ion beam line during irradiation experiments. This system has two measurement ranges of 10^{-11}A and 10^{-9}A of micro FC for the purpose of the measurement of very small ion beam current. By these devices, even faint current of the order of 10^{-11}A was successfully detected without any noise.. As shown in Fig. 2 the system was operated at the distance of about 100 m between the target room and the control room. The amount of the currents induced by ion beam is displayed as numerical voltages and figurized in color after computational processing.

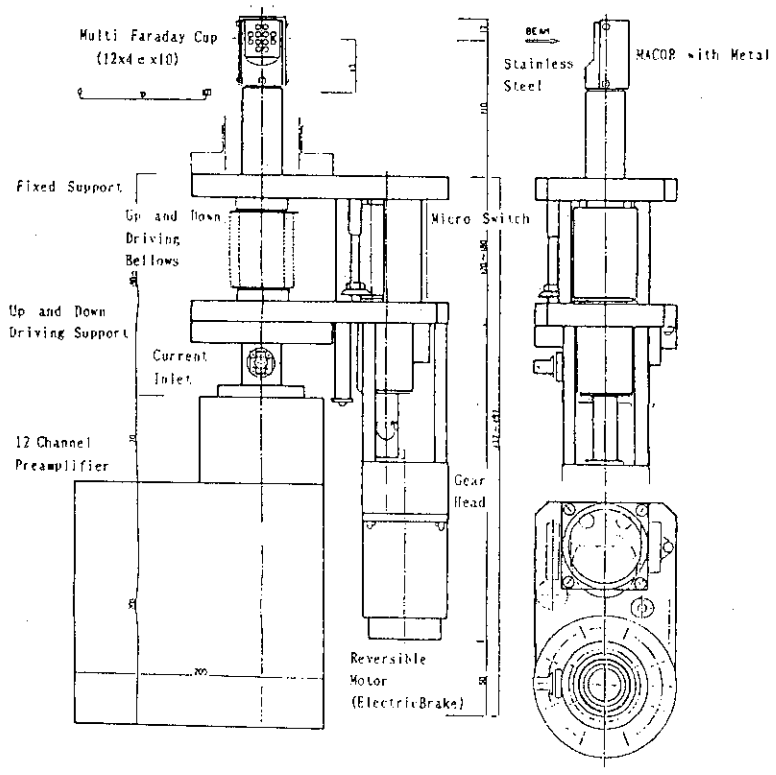

Fig. 1. Drawing of Multi Faraday Cup

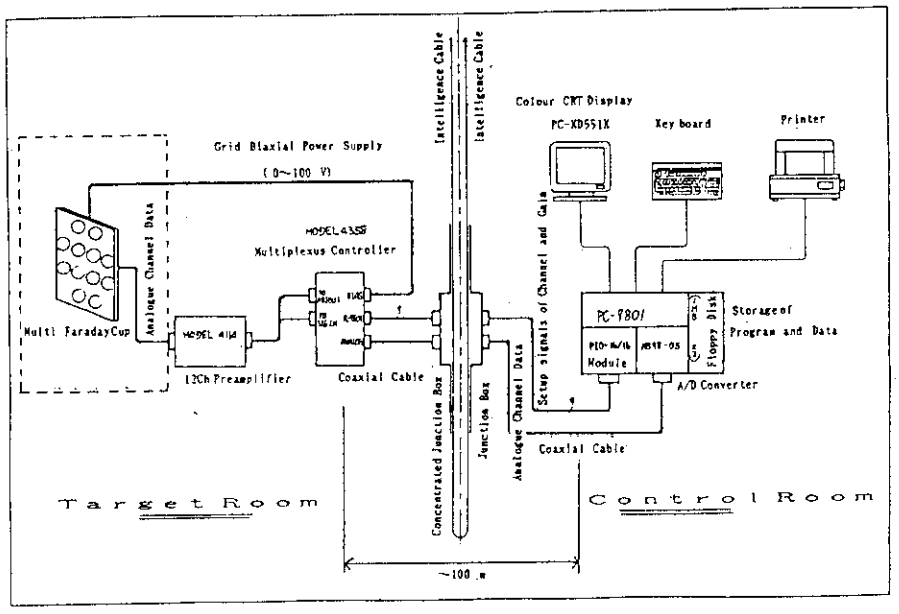

Fig. 2. System Components for Measurement of Micro Heavy Ion Beams

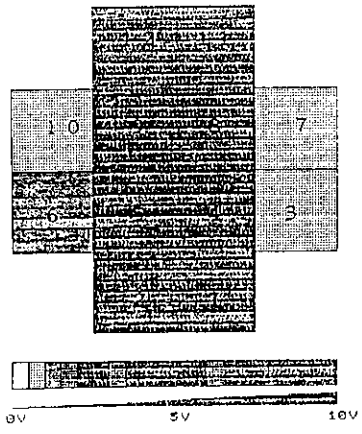

90/12/12 12:14:40
RANGE= -11 GAIN= 1

Channel	Data	percent	B	G
1 ch	4.71 V	79 %	0.00 V	
2 ch	5.08 V	85 %	0.00 V	
3 ch	0.90 V	15 %	0.00 V	
4 ch	5.59 V	94 %	0.00 V	
5 ch	5.59 V	94 %	0.00 V	
6 ch	1.06 V	18 %	0.00 V	
7 ch	0.73 V	12 %	0.00 V	
8 ch	5.97 V	100 %	0.00 V	
9 ch	5.16 V	86 %	0.00 V	
10 ch	0.88 V	15 %	0.00 V	
11 ch	4.35 V	73 %	0.00 V	
12 ch	3.80 V	64 %	0.00 V	

Fig. 3. Distribution of Heavy Ion Beam and Channel Data
- Ni ion

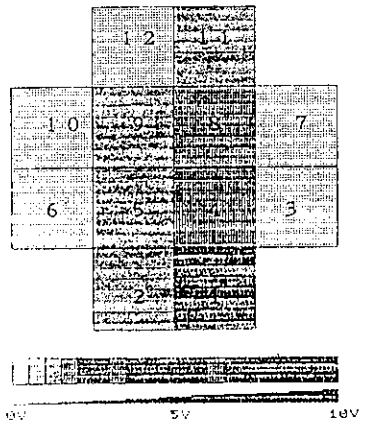

91/01/09 11:22:38
RANGE= -11 GAIN= 1

Channel	Data	percent	B	G
1 ch	2.01 V	100 %	0.00 V	
2 ch	1.45 V	72 %	0.00 V	
3 ch	0.50 V	25 %	0.00 V	
4 ch	1.82 V	91 %	0.00 V	
5 ch	1.31 V	65 %	0.00 V	
6 ch	0.72 V	36 %	0.00 V	
7 ch	0.51 V	25 %	0.00 V	
8 ch	1.55 V	77 %	0.00 V	
9 ch	1.11 V	55 %	0.00 V	
10 ch	0.60 V	30 %	0.00 V	
11 ch	1.20 V	60 %	0.00 V	
12 ch	0.87 V	43 %	0.00 V	

Fig. 4. Distribution of Heavy Ion Beam and Channel Data
- Ag ion

Results of operation test

Prior to the irradiation of the membrane(sheets of 13 mm in diameter fixed on the support 25 mm in diameter), the examples of distribution of the defocused ion beam were observed on Multi FC, as are shown in Figs. 3 and 4. The figures were displayed originally in color and at the same time gave the output voltages, percent and background voltages(BG). As BG values usually were negligible, each voltage gave the sum of voltage due to ion beam and that due to secondary electron emission. One could get information about the distribution of ions from the figures, though it is not the absolute value of voltage induced by ions. Figure 3 shows the example of uneven distribution of ion beam. Figure 4 shows the satisfactory distribution of ion beam as a whole. Ion beam with an extremely ununiform distribution can be corrected by monitoring the change in color or value of voltage on CRT. Table 1 shows the comparison between the currents on multi FC and on the neighboring FC at Tandem accelerator. The current from multi FC showed roughly the same as the current from FC at Tandem accelerator.

References

1) Y. Komaki, N. Ishikawa, T. Sakurai, N. Morishita and M. Iwasaki : Nucl. Instrum and Methods, B34(1988)332

2) Y. Komaki, Y. Matsumoto, N. Ishikawa and T. Sakurai : POLYMER COMMUNICATIONS 30(1989)43

Table 1 Comparison of currents observed by multi FC and FC at beam line

No	C $\times 10^{-9}$, s		Ion, Day		V/cup mean, A=V/R R=10^{-11}		B=Axf1xf2 $\times 10^{-9}$	B/C
1	3.0	10	Ni	1/9	0.95	$\times 10^{-11}$	4.30	1.4
2	21	7	Ag	12/12	3.94	$\times 10^{-11}$	17.8	0.9
3	20	5	Ag	12/4	3.79	$\times 10^{-11}$	17.2	0.9
4	6.3	10	Ag	7/24	2.15	$\times 10^{-11}$	9.73	1.5
5	6.5	10	Ni	3/1	1.88	$\times 10^{-11}$	8.51	1.3

f_1 : ratio of the area of A to total area, 61.8

f_2 : 12 (Cups)

2.2 INCIDENT ANGLE DEPENDENCE OF RESIDUAL DEFECT IN SILICON SURFACE BARRIER DETECTOR

Ikuo KANNO, Hiroshi IKEZOE†, Tsutomu OHTSUKI‡,
Shu A. HAYASHI*, Satoshi KANAZAWA** and Itsuro KIMURA**

Department of Reactor Engineering, JAERI, †Department of Physics, JAERI, ‡Tohoku University, *Institute for Atomic Energy, Rikkyo University, **Kyoto University

In the pulse height defect of a silicon surface barrier detector (SSB), the residual defect, which is the defect other than the window defect and the nuclear stopping defect, has been a theme of studies. The residual defect was recognized as the result of recombinations of electrons and holes which consisted the plasma column created by an incident charged particle. In many studies, the number of recombinations was estimated using some parameters such as recombination life time, however, none of them were very successful[1),2)],especially, in explaining the dependences of the residual defect on the bias voltage and the resistivity of SSB.

Recently, one of the authors reported that the residual defect was derived theoretically from the dielectric property of the plasma column.[3)] The residual defect was calculated using the length of the plasma column which was created by an incident charged particle and the depletion layer thickness of an SSB which was employed for measurements. This model contained one parameter, called screening factor, which represented the degree of dielectricity of the plasma column, and was determined by an experiment.

The incident angle dependence of the residual defect is another theme of interest. Some experimental works reported the incident angle dependence of the pulse height defect[4),5)], however, the results were confusing due to the mixture of the window defect, the nuclear stopping defect and the residual defect. The residual defect should be studied on the incident angle dependence, because we can calculate the window defect and the nuclear stopping defect.

Experiments were performed at the Tandem Accelerator Facility of Japan Atomic Energy Research Institute (JAERI). Nickel-58 ions with incident energies of 101.7MeV and 133.9MeV and ^{127}I ion of 129.8MeV were detected by SSBs with the resistivities of 362Ωcm, 1500Ωcm and 2100Ωcm. The incident angle, θ, was changed as normal to the incident surface, 30, 45 and 60 degrees from the normal line for the ^{58}Ni ion of

133.9MeV, whereas, measurements were carried out only for normal incidence in the cases of the ^{58}Ni ion of 101.7MeV and the ^{127}I ion of 129.8MeV. The pulse heights were measured with changing bias voltage.

Measured energies, $E_{exp.}$, are shown in Fig.1 by symbols, for ^{58}Ni ions of 101.7MeV and 133.9MeV with normal incidence and for the ^{127}I ion of 129.8MeV. The full widths at half maximum of the energy spectra are shown by the bars. In Fig.2, $E_{exp.}$ of the ^{58}Ni ions of 133.9MeV with incident angles of 0, 30, 45 and 60 degrees are plotted. The summary of the results of Figs. 1 and 2 are shown in Table 1. From these experiments, we conclude (1) the experimental results taken by the SSB of 362Ωcm, which has high electric field strength, are excellently reproduced by the model of dielectric plasma column, (2) in the case of non-zero angle incidence, the length and the electron-hole density of the plasma column are regarded as the projected length and the projected electron-hole density, (3) the screening factor, which represents the rate of plasma column screening electrons and holes, is almost proportional to the electron-hole density. The experimental results taken by the SSBs of 1500Ωcm and 2100Ωcm, which have lower electric field strengths, are smaller than expected from the model of dielectric plasma column. We think this results are caused by the effect due to lower electric field strength, such as recombinations and trappings.

References

1) Finch, E.C.: Nucl. Instrum. and Meth., **142**, 539 (1977).
2) Hansen, N.J.: Nucl. Instrum. and Meth., **96**, 373 (1971).
3) Kanno, I.: J. Nucl. Sci. Technol., **28**, 87 (1991).
4) Konecny, E. and Hetwer, K.: Nucl. Instrum. and Meth., **36**, 61 (1965).
5) Smith, G.D.: Dissertation, TID-26636.

Table 1 Quantities for the calculation of dielectric effect of plasma column created by heavy ions. θ: incident angle, Δ_w: window loss, Δ_n: nuclear stopping loss, E_0: energy spent to produce electron-hole pairs, $l \cdot cos\theta$: projected plasma column length, $E_0/l^3 cos\theta$:approximate electron-hole density of plasma column, f: screening factor.

Particle	Energy (MeV)	θ (deg.)	Δ_w (MeV)	Δ_n (MeV)	E_0 (MeV)	$l \cdot cos\theta$ (μm)	$E_0/l^3 cos\theta$ (10^{10}MeV/cm^3)	f
Ni-58	101.7	0	0.4	0.9	100.4	17.1	2.00	0.23
	133.9	0	0.5	0.9	132.5	21.1	1.41	0.16
		30	0.6	0.9	132.4	18.3	1.63	0.17
		45	0.7	0.9	132.3	14.9	1.99	0.22
		60	1.0	0.9	132.0	10.6	2.82	0.31
I-127	129.8	0	0.8	3.4	125.6	17.0	2.57	0.25

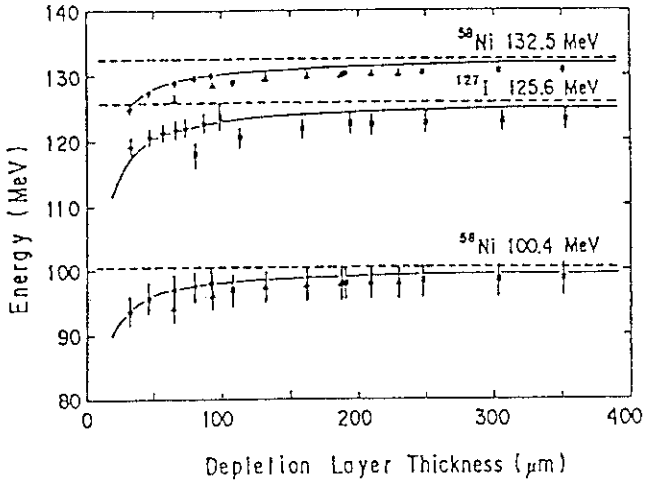

Fig.1 Measured energies of heavy ions in the case of normal incidence. Measurements were carried out with 362 Ωcm (•), 1500 Ωcm (▲) and 2100 Ωcm (■) SSB. Solid and dashed lines show the predicted energy by the dielectric effect model and the energies spent to produce electron-hole pairs.

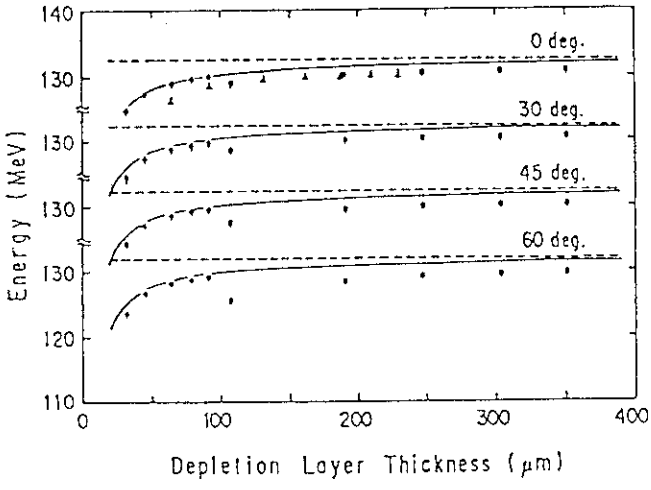

Fig.2 Same as in Fig.1 but for ^{58}Ni ion with incident energy of 133.9MeV with incident angles of 0, 30 45 and 60 degrees.

2.3 IRRADIATION EFFECTS ON IONIC CONDUCTIVITY OF PURE AND AL-DOPED LITHIUM ORTHOSILICATE

Kenji NODA, Yoshinobu ISHII, Tetsuya NAKAZAWA,
Hisayuki MATSUI*, Mikio HORIKI*, Manabu HOSHINO*,
Naomi OBATA*, and Hitoshi Watanabe*

Department of Fuels and Materials Research, JAERI, *Faculty of Engineering, Nagoya University

1. Introduction

Lithium orthosilicate (Li_4SiO_4) is a candidate of tritium breeders for D-T fusion reactors. Al-doped Li_4SiO_4 ($Li_{3.7}Al_{0.1}SiO_4$) was recently developed to improve the tritium release performance of Li_4SiO_4 at low temperatures[1]. In this material, the tritium diffusivity is considered to be increased by introduction of lithium-ion vacancies due to doped Al.

A large number of irradiation defects will be introduced in the lithium ceramics as tritium breeders during operation of fusion reactors. These defects not only will induce swelling and cracking but also will affect transport phenomena such as tritium diffusion.

Ionic conductivity of lithium ceramics is controlled by lattice defects including irradiation defects, solute atoms and impurities. The conductivity reflects the lithium diffusion and is also considered to be closely related to tritium diffusion[2]. From this standpoint, in-situ measurements of ionic conductivity of Li_2O have been carried out to evaluate irradiation effects on the tritium migration behavior[3,4].

In the present study, ionic conductivity of Li_4SiO_4 and $Li_{3.7}Al_{0.1}SiO_4$ under and after irradiation and thermal recovery behavior of the conductivity were investigated to obtain information on the radiation damage and irradiation effects on the tritium diffusion.

2. Experimental

The Li_4SiO_4 and $Li_{3.7}Al_{0.1}SiO_4$ sintered pellets were fabricated by pressing the powder at hydrostatic pressure of $1.6X10^2$ MPa and heating them at 1353 K for 5 h in air. Thin disk specimens of the pellets (8 to 9 mm in diameter, about 0.4 mm in thickness) were irradiated at the prescribed temperatures with 120 MeV oxygen and 60 MeV lithium ions using

a tandem accelerator at JAERI. Ionic conductivity of the specimens was measured under and after irradiation with the two terminal AC method using a HP 4194 A impedance analyzer.

3. Results and discussion

The ionic conductivity of Li_4SiO_4 and $Li_{3.7}Al_{0.1}SiO_4$ in non-irradiated condition was measured in the temperature range 373 K to 613 K. The conductivity of $Li_{3.7}Al_{0.1}SiO_4$ is higher than that of Li_4SiO_4 in this temperature range by about two orders of magnitude.

Fig. 1 shows the conductivity of Li_4SiO_4 in the post-irradiation condition as a function of the fluence in the temperature range 413 K to 613 K for 120 MeV oxygen-ion irradiation. The conductivity increased with the fluence in the examined temperature range. In fig. 2, the conductivity of $Li_{3.7}Al_{0.1}SiO_4$ in the post-irradiation condition is shown versus the fluence in the temperature range 373 K to 503 K for 120 MeV oxygen-ion irradiation. The conductivity in the temperature range 373 K to 413 K increased with the fluence, while the fluence dependence was hardly observed in the temperature range 443 K to 503 K. Similar irradiation effects on the conductivity in the post-irradiation condition were observed for Li_4SiO_4 and $Li_{3.7}Al_{0.1}SiO_4$ irradiated with 60 MeV lithium ions.

The recovery behavior of conductivity for Li_4SiO_4 and $Li_{3.7}Al_{0.1}SiO_4$ was examined by isochronal annealing experiments. The increase of conductivity of Li_4SiO_4 due to the irradiation was not recovered even at the annealing temperature of 675 K.

Fig. 3 shows the recovery behavior of conductivity at 373 K for $Li_{3.7}Al_{0.1}SiO_4$ irradiated to 3.79×10^{19} ions.m^{-2} with 120 MeV oxygen ions as a function of the annealing temperature. The increase of conductivity due to the irradiation was recovered in the annealing temperature range 373 K to 473 K. This recovery is considered to lead to the conductivity of $Li_{3.7}Al_{0.1}SiO_4$ in the post-irradiation condition which was unchanged with the fluence in the temperature range 443 K to 503 K as well as high values of the conductivity above 443 K in comparison with the increase of conductivity due to the irradiation.

On the assumption that the tritium diffusivity in Li_4SiO_4 and $Li_{3.7}Al_{0.1}SiO_4$ is closely related to the ionic conductivity, the irradiation effects on the tritium diffusivity are considered to be as follows. The tritium diffusivity in Li_4SiO_4 in the post-irradiation condition in-

creases with the fluence in the temperature range 413 K to 673 K. On the other hand, the tritium diffusivity in $Li_{3.7}Al_{0.1}SiO_4$ in the post-irradiation condition increases with the fluence in the temperature range 373 K to 413 K, while it hardly changes with the fluence in the temperature range 443 K to 503 K.

The tritium diffusivity in $Li_{3.7}Al_{0.1}SiO_4$ in the post-irradiation condition is considered to be higher than that in Li_4SiO_4, since the conductivity of $Li_{3.7}Al_{0.1}SiO_4$ in the post-irradiation condition is higher than that of Li_4SiO_4. Actually, the advantage of $Li_{3.7}Al_{0.1}SiO_4$ in the tritium release performance in the post-irradiation condition for Li_4SiO_4 was shown in the study of Vollath et al[1].

The conductivity of both Li_4SiO_4 and $Li_{3.7}Al_{0.1}SiO_4$ under irradiation was higher than that before and after irradiation, and it increased with the ion flux. The ratios between the increments of conductivity under irradiation $\Delta\sigma$ for Li_4SiO_4 or $Li_{3.7}Al_{0.1}SiO_4$ at various temperatures and the conductivity in the post-irradiation condition σ are shown as a function of the ion flux for 120 MeV oxygen-ion irradiation in fig. 4. The values of conductivity for $Li_{3.7}Al_{0.1}SiO_4$ under irradiation were higher than those for Li_4SiO_4 at the same irradiation flux and temperature levels by about two orders of magnitude. From these results, it is considered on the assumption that the tritium diffusivity in Li_4SiO_4 and $Li_{3.7}Al_{0.1}SiO_4$ is closely related to the ionic conductivity, that there is a possibility of enhancement of the tritium diffusion in Li_4SiO_4 and $Li_{3.7}Al_{0.1}SiO_4$ under irradiation and that the tritium diffusivity in $Li_{3.7}Al_{0.1}SiO_4$ under irradiation is higher than that for Li_4SiO_4.

References

1) D. Vollath and H. Wedemeyer: Advances in Ceramics 27 (1990) 3.
2) H. Ohno, S. Konishi, T. Nagasaki, T. Kurasawa, H. Katsuta and H. Watanabe: J. Nucl. Mater. 133-134 (1985) 181.
3) K. Noda, Y. Ishii, H. Ohno, H. Watanabe and H. Matsui: Advances in Ceramics 27 (1990) 227.
4) K. Noda, Y. Ishii, H. Matsui, H. Ohno and H. Watanabe: J. Nucl. Mater. 179-181 (1991) 835.

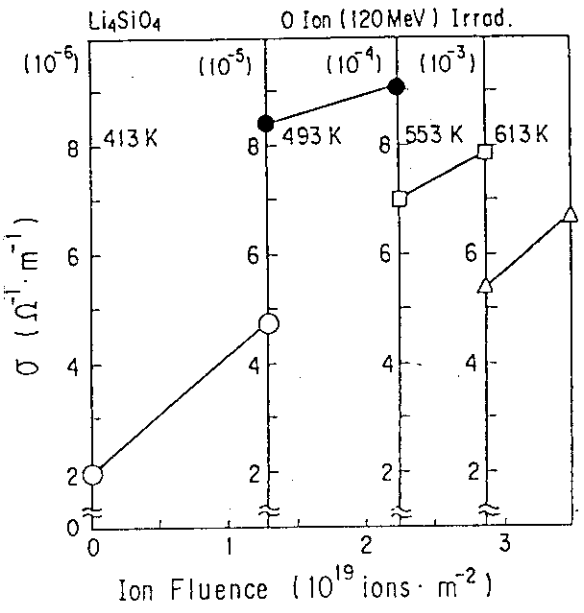

Fig.1 Ionic conductivity of Li_4SiO_4 in the post-irradiation condition versus oxygen-ion fluence.

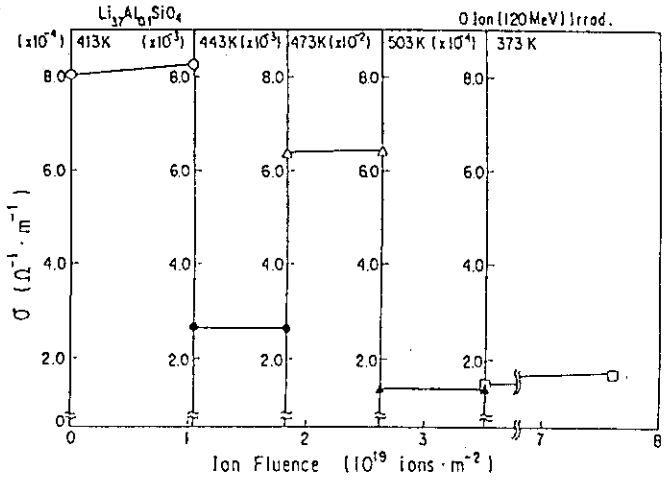

Fig.2 Ionic conductivity of $Li_{3.7}Al_{0.1}SiO_4$ in the post-irradiation condition versus oxygen-ion fluence.

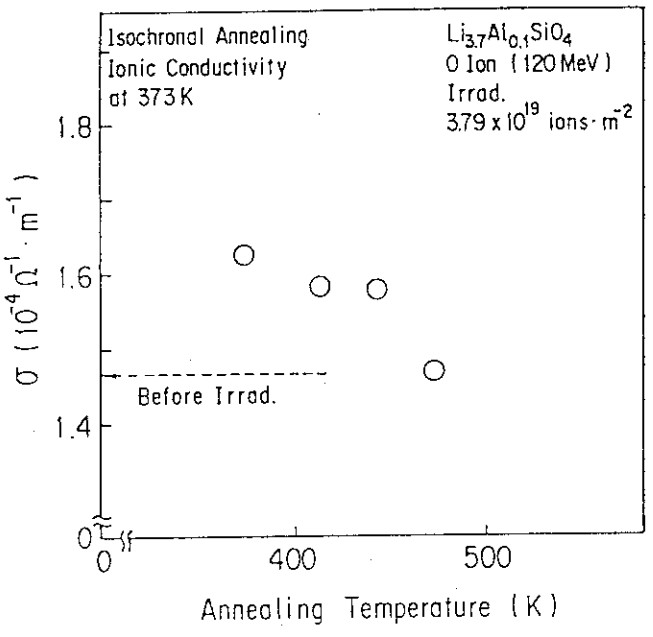

Fig.3 Recovery behavior of ionic conductivity of $Li_{3.7}Al_{0.1}SiO_4$ in isochronal annealing experiments.

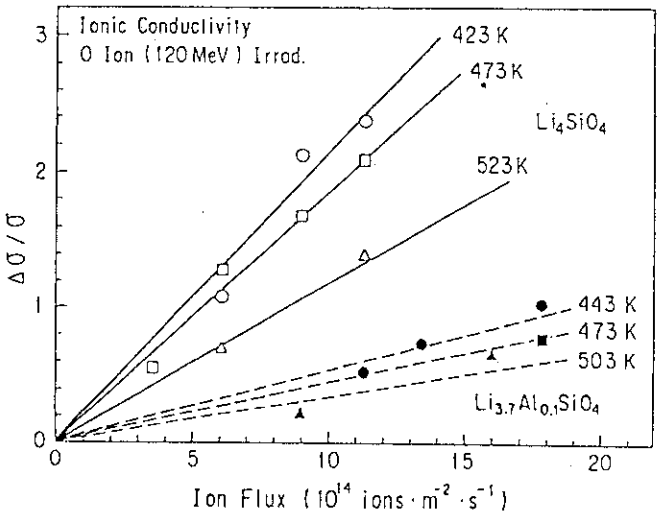

Fig.4 Normalized increments of conductivity under irradiation versus oxygen-ion flux.

2.4 IRRADIATION BEHAVIOR OF TRITIUM-BREEDING CERAMICS

Hisayuki MATSUI, Mikio HORIKI, Manabu HOSHINO,
Kenji NODA*, Yoshinobu ISHII*, and Hitoshi WATANABE*

Department of Nuclear Engineering, Nagoya University,
*Division of Material Development, JAERI

Introduction

Development of tritium breeding blanket is one of the most important subjects in fusion technology (D-T fusion). In a half decade, several kinds of ceramics containing Li have been investigated. Among a variety of the Li ceramics, lithium orthosilicate (Li_4SiO_4) is considered to be a desirable candidate for the breeding material and R/D on that material have been continuing mainly in europe. In order to improve tritium release performance, an advanced breeding material was fabricated by doping of Al to the above ceramics ($Li_{3.7}Al_{0.1}SiO_4$). A replacing of Li (monovalent) by Al (divalent) causes an introduction of Li vacancy. Thus, we can expect an enhancement of the diffusion of Li atoms which is closely related to tritium diffusion.

In the present study (the fysical year, 1990), we investigated effects of irradiation-induced defects on the electrical conductivity of the above ceramics. In-situ conductivity measurements were done under irradiations by highly energetic self-ions (e.g.,120 MeV O^{7+} and 60 MeV Li^{3+} ions) at various temperatures. The aim of the study was to obtain knowledge of irradiation damage on those materials, from which we could evaluate the change of transport phenomena concerning to Li atoms, and, thus, tritium diffusion as well. The information concerning to induced defect structure will allow us a fruitful discussion on the mechanism of matter transport.

Experiments

Pure and Al-doped lithium orthosilicates (hereafter, we denote "pure" as Li_4SiO_4 and "Al-doped" as $Li_{3.7}Al_{0.1}SiO_4$) were synthesized in powder form by the methanol process developed by Vollath et al[1]. After pressing the powder at hydrostatic pressure of 1.6×10^2 MPa, sintered pellets were obtained by heating at 1353 K for 5 h in air. The pellet was cut out into thin disk (8 mm in diameter and about 0.4 mm in thickness).

The thin plates were irradiated with 120 MeV oxygen and 60 MeV lithium

ions using a tandem accelerator at JAERI. Measurement of ionic conductivity were done at various temperatures. In addition to post-irradiation measurements, in-situ measurements were also performed at various temperatures. The measurements of conductivity (converted from the electric resistance) were carried out by the two-terminal ac method, employing the HP4194A Inpedance Analyzer. A full automatic data collection system was used and a set of data of the resistance were compiled in a microcomputer. Details of the experimental procedures were reported before.

Results and Discussion

1. Ionic Conductivity of "Pure" and "Al-doped" Specimens

Ionic conductivity (σ) of "pure" and "Al-doped" lithium orthosilicates are illustrated in Fig. 1, in a relation between σT and the inverse of the absolute temperature, 1/T. The conductivity of the "pure" specimen is two order higher than that of Li_2O (single crystal)[2]. The "Al-doped" one shows much higher conductivity than the "pure" by two order of magnitude in the temperature between 373 and 613 K. The measured conductivity for both specimens are in a fairly good agreement with those for the Li_2O-Al_2O_3-SiO_2 system in a study by Jackowska et al[3]. The slope of the Arrehnius plot, which implies the activation energy of diffusion for Li, is small in the "Al-doped" ones, indicating a high mobility of Li. Thus the temperature dependences of the ionic conductivity of both specimens are reasonable.

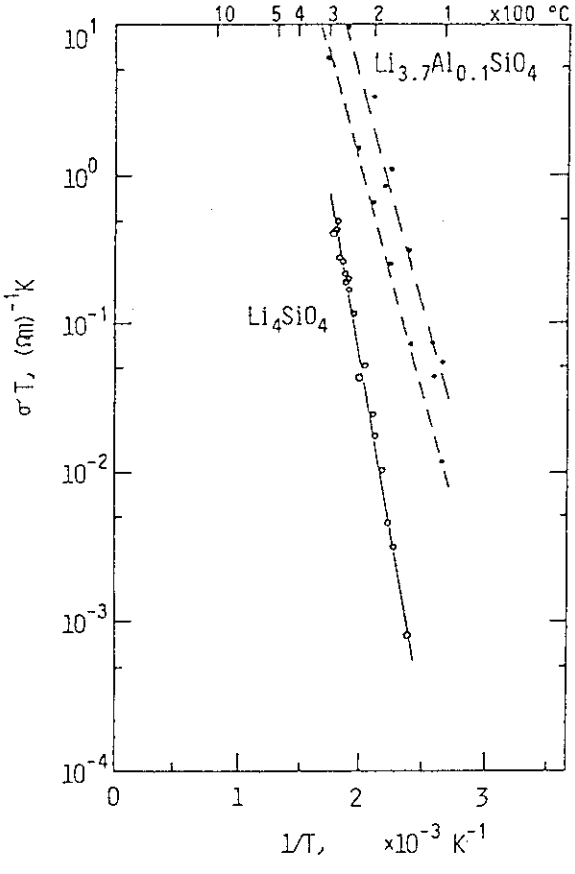

Fig. 1 Ionic Conductivity of "pure" and "Al-doped" Li_4SiO_4

2. Irradiation Effect

The change of the conductivity are shown in Fig. 2 and 3 for the "pure" and "Al-doped" Li_4SiO_4, respectively. The measurement was done in the "Post-Irradiation Condition".

In Fig. 2 ("pure" specimen irradiated by 120 MeV oxygen), the conductivity increased clearly with ion fluence in temperature region examined. In Fig. 3 ("Al-doped"), however, the fluence dependence was hardly found, especially at above 443 K. A similar effect was observed when 60 MeV Li-ions were bombarded to those ceramics. It seems that the "Al-doped" is resistive to the ion bombardment. It is reasonably considered that structural vacancies introduced by Al-doping may play some roles to annihilate the irradiation-induced defects.

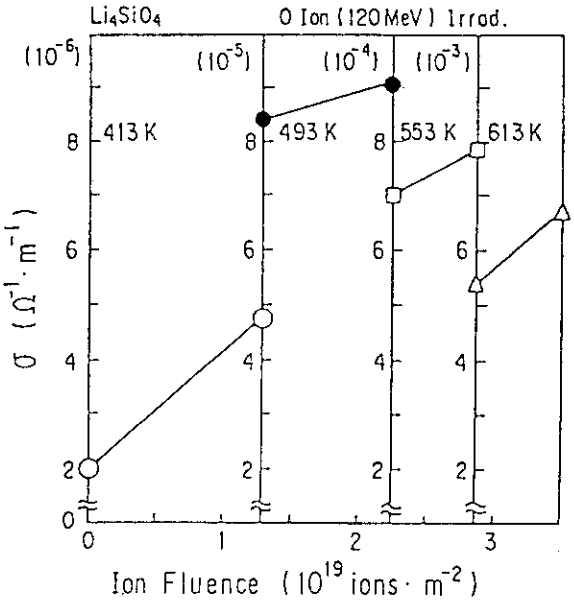

Fig. 2 Change of σ in Li_4SiO_4

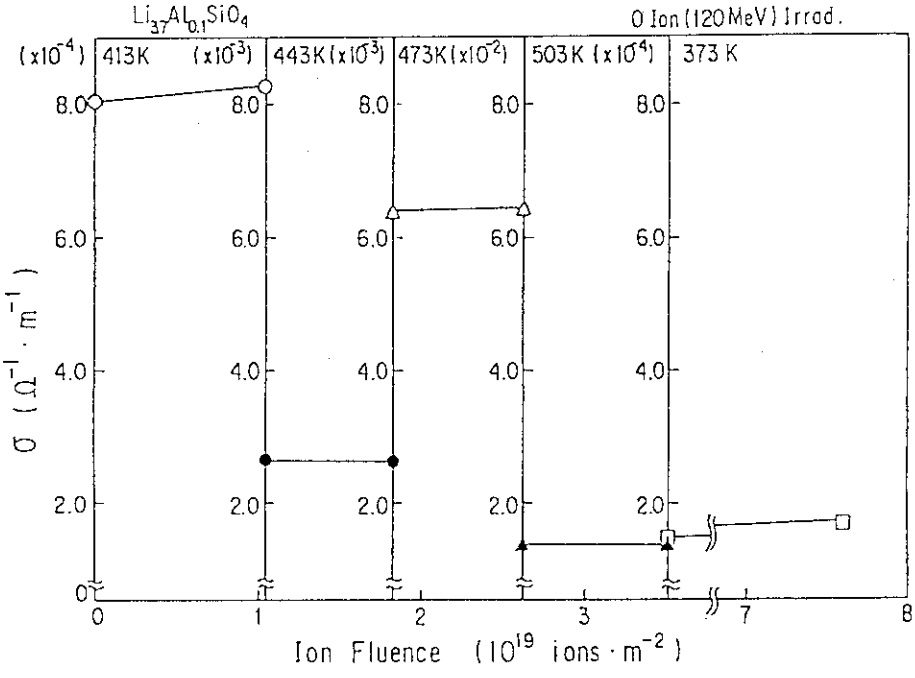

Fig. 3 Change of conductivity in $Li_{3.7}Al_{0.1}SiO_4$

As a summary, fractional change ($\sigma\Delta/\sigma$: %, normalized at a fluence of 4 x 10^{18} O-ions/m^2) of the ionic conductivity are listed in Table 1 for both specimens by 120 MeV O^{7+} ion irradiation at various temperatures. The table clearly indicates that the increase of conductivity, thus irradiation damage, is much less in the "Al-doped" than the "pure" specimen. It is also

clear that both ceramics reveal high irradiation damage at low temperature. As the increase of ionic conductivity suggests an enhancement of mobility of Li in this case, Li-vacancies are effectively induced by irradiation at low temperature. Those induced vacancies might annihilate at about 450 K, which was a lower temperature of the annihilation of F^+ center in Li_2O[4].

Table 1 Induced conductivity ($\Delta\sigma/\sigma$: %) at various temperatures.
120 MeV Oxygen Irradiation
(Normalized at 4×10^{18} ion/m^2)

Temperature (K / °C)	Li_4SiO_4	$Li_{3.7}Al_{0.1}SiO_4$
373 / 100	--	2.2
413 / 140	55.5	0.8
443 / 170	--	1.4
473 / 200	--	0.9
493 / 220	7.4	--
503 / 230	--	1.2
553 / 280	13.6	--
613 / 340	14.5	--

It was of interest that ionic conductivity of both ceramics was very high during the irradiation, as had been found in Li_2O[5] both by 120 MeV-O and 60 MeV-Li ions bombardments. In the present stage, an idea of an irradiation-enhanced phenomenon was most plausible. Because the Li mobility is closely related to the conductivity in lithium ceramics (e.g., Li_2O), an enhanced diffusion of Li assisted by excess vacancies plays a major role to the increase of the conductivity. In the irradiation by such a high energy particle, an excitation of electrons and/or holes is also expected. Therefore, more careful experiment and its precise interpretation will be needed for a fully understanding of the effects of radiation damage on the diffusion of Li, and, thus, the diffusion mechanism of tritium.

References

1) D.Vollath, H.Wedemeyer, H.Zimmermann and H.Werle: J. Nucl. Mater., 174 (1990) 86.
2) K.Noda, Y.Ishii, H.Ohno, H.Watanabe and H.Matsui: Advances in Ceramics, Vol. 25 (Am. Ceram. Soc., 1989) pp.155-164.
3) K.Jackowska and A.R.West: J. Mat. Sci., 18 (1983) 2380.
4) K.Noda, Y.Ishii, H.Matsui and H.Watanabe: Rad. Effects 97 (1986) 297.
5) K.Noda, Y.Ishii, H.Ohno, H.Watanabe and H.Matsui: Adv. in Ceramics (Am. Ceram. Soc., 1990) pp.227-247.

2.5 ELECTRICAL AND STRUCTURAL PROPERTIES OF Li-ION IRRADIATED β-LiAl

Kazuo KURIYAMA, Naoyuki MINEO, Hiromi TAKAHASHI, Yukio KAZUMATA*, and Hiroyuki SUGAI**

College of Engineering and Research Center of Ion Beam Technology, Hosei University, *Department of Physics, JAERI, **Department of Radioisotopes, JAERI

LiAl alloy is an useful material for solid-blanket of nuclear fusion.[1] Electrical conductivity of β-LiAl below room temperature has been reported.[2-4] The important feature of the conduction mechanism for β-LiAl is governed by positive carriers(holes)[5,6] in the valence band. The electrical conductivity based on these holes is affected considerably by the defect structure[7] in β-LiAl(about 48-56at.%Li). The defect structure at room temperature consists of two types of defect: vacancies in the lithium sublattice (V_{Li}), and lithium antistructure atoms in the aluminum sublattice (Li_{Al}). The purposes of the present work are (i) to measure electrical resistivity of β-LiAl before and after Li-ion irradiation and (ii) to survey the modification of Li vacancies in Li-ion irradiated β-LiAl.

Samples were prepared by a resistance furnace melting of 99.9% lithium and 99.999% aluminum. The details of sample preparation have been previously described.[8,9] A typical X-ray diffraction pattern of β-LiAl before irradiation shows in Fig.1. Ion irradiations were performed by a tandem accelerator at JAERI. 60MeV-$^7Li^{3+}$ ion was used in this study. Samples were irradiated with Li-ions in a range 1.3×10^{15} - 4.0×10^{15} /cm^2 at 140 K.

The electrical resistivity measurement was made using Van der Pauw technique.[10] In order to evaluate the depth profiles of electrical properties, a few μm were removed from the irradiated side of the samples for each measurement. The variation of sheet resistance(ΔR_s) in depth(d) was estimated by

$$\Delta R_s(d) = R_s(\text{irra.}) - R_s(\text{unirra.}),$$

where, R_s(irra.) and R_s(unirra.) are a sheet resistance after and before irradiation, respectively. Since this is destructive method, the specimens, cut from same batch used for irradiation, were used for the resistance measurements in each depth before irradiation. Figure 2 shows typical depth profiles of sheet resistance(R_s(unirra.)) before irradiation. This indicates that the values mea-

sured are constant in depth within experimental error. Therefore, R_S(unirrad.) values were calculated from ρ/w, where ρ is the resistivity of the unirradiated sample and w is the sample thickness after polishing.

In the present experiment, the metallic precipitations were not observed in the as-irradiated surface and the polished surface, while the precipitations were observed in our previous work[11]. This phenomenon may arise from the aluminum segregation in starting materials. Figure 3 shows typical depth profiles of ΔR_S after irradiation with 60MeV- $^7Li^{3+}$ ion of 1.5 x $10^{15}cm^{-2}$ together with the calculated range (0.56mm) of Li-ions at 60 MeV for β-LiAl. The depth profile of ΔR_S has a maximum just behind the range of Li-ions. This indicates that the radiation damage extends over the range of Li-ions. The Li-ion irradiation is likely to influence the electrical properties, accompanied by the radiation damage. However, there is a problem for obtaining the reproducible data, which will arise from the accuracy of electrical measurements. In order to verify the relations between the damage due to Li-ion irradiation and the depth profile of ΔR_S, irradiation experiments with different kinds of Li-ion energy and other ions are required.

References

1) J.R.Powell, F.T.Miles, A. Aronson, and W.E.Winsche, BNL-18236, Brookhaven National Laboratory(1973).

2) K.Kuriyama, T.Kamijoh, and T.Nozaki, Phys.Rev.B 22, (1980)470; K.Kuriyama, S.Yanada, T.Nozaki, and T.Kamijoh, Phys. Rev. B 24, (1981)6158.

3) T.Asai, M.Hiratani, and S.Kawai, Solid State Commun. 48, (1983)173.

4) L.H.Hall, T.O.Brun, G.W.Crabtree, J.E.Robinson, S.Susman, and T.Tokuhiro, Solid State Commun. 48,(1983)547.

5) K.Kuriyama, T.Nozaki, and T.Kamijoh, Phys. Rev. B 26, (1982)2235.

6) M.Yahagi, Phys.Rev.B 24, (1981)7401.

7) K.Kishio and J.O.Brittain, J.Phys.Chem.Solids 40, (1979)993.

8) K.Kuriyama, S.Saito, and K.Iwamura, J. Phys. Chem. Solids 40, (1979)457.

9) M.Yahagi, J. Cryst. Growth 49, (1980)396.

10) L.J.Van der Pauw, Philips Tech. Rev. 20, (1958)220.

11) K.Kuriyama, N.Mineo, H.Sugai, H.Naramoto, Y.Kazumata, and H.Motohashi, JAERI Tandem, Linac and V.D.G Annual Report 1989, pp.84-87.

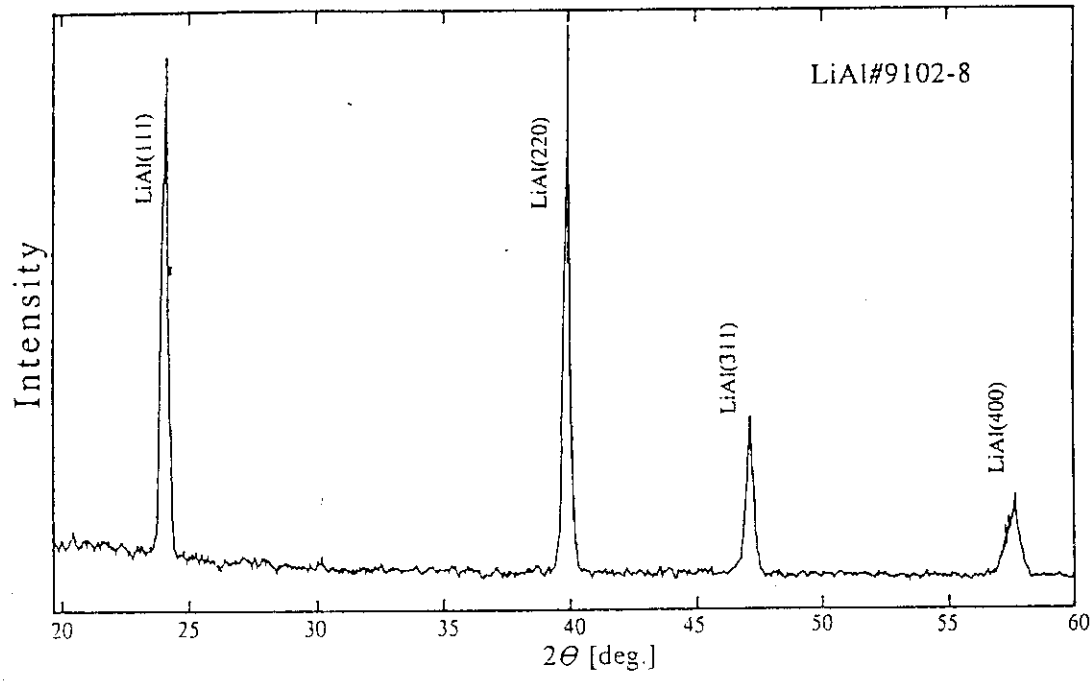

Fig.1 A typical X-ray diffraction pattern of β-LiAl before irradiation.

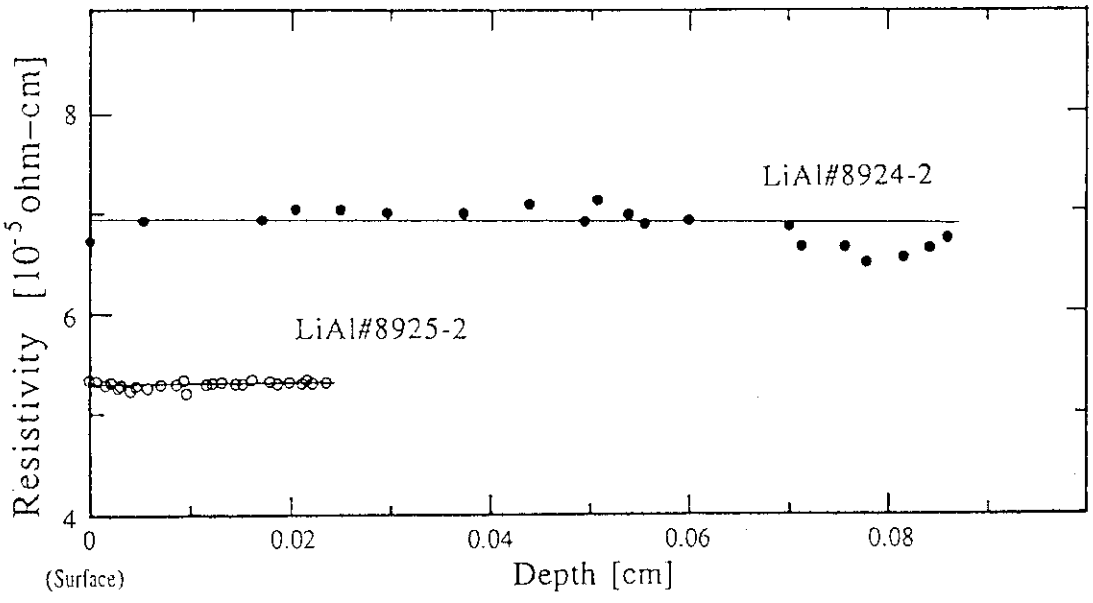

Fig.2 The depth profile of sheet resistance of unirradiated β-LiAl.

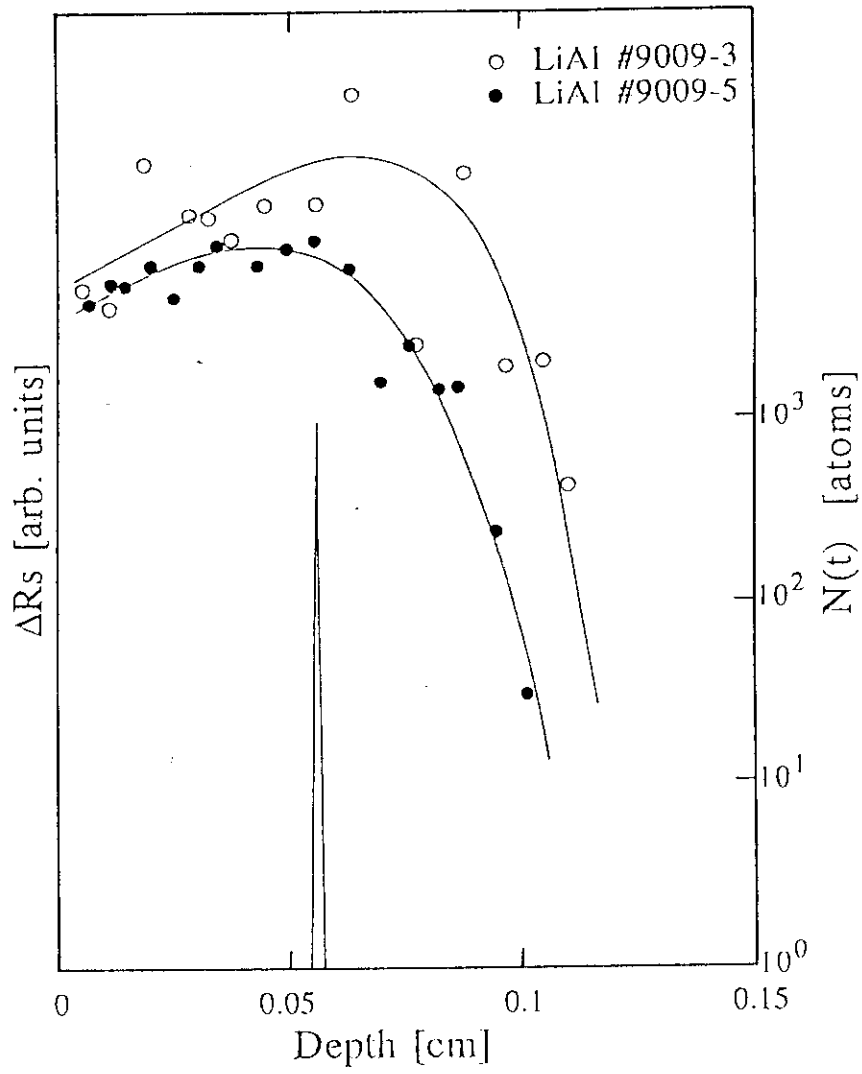

Fig.3 A typical depth profile of ΔR_s and the calculated range of $^7Li^{3+}$-ion at 60MeV in β-LiAl.

2.6 ION BEAM ANALYSIS OF ION-IRRADIATED NICKEL

Tohru MITAMURA, Mititaka TERASAWA, Hajime IWASAKI, Keiji KOTERASAWA, Kiyoshi KAWATSURA*, Masao SATAKA**, Makoto IMAI**, Hiroshi MAETA**, Akiyoshi CHAYAHARA**, Mamoru SATOU**,

Himeji Institute of Technology, *Kyoto Institute of Technology, **Japan Atomic Energy Research Institute, ***Government Industrial Research Institute, Osaka

Rutherford backscattering (RBS) and particle induced X-ray emmision (PIXE) measurements were carried out for nickel single crystal specimens to which phosphorous atoms have been implanted. It was found that subsequent irradiation of Ni^{10+} ions to this P implanted nickel specimen enhanced segregations of the phosphorous atoms. In this radiation induced segregation (RIS) process, it seemed that parts of the phosphrous atoms locate at a definite interstitial site, probably, being combined with displaced nickel atoms to form a Ni-P mixed dumbbell.

Introduction

Elucidation of mechanisms of radiation damages in nuclear reactor materials is important in order to evaluate operation life of nuclear fission reactors and also to develop materials for nuclear fusion reactors. The radiation effect in austenitic stainless steels, which are one of the main nuclear reactor materials, has been studied previously by the authors[1]. In the present study, nickel single crystal, which has the same crystal structure as austenitic atainless steel, i.e. fcc, was analysed. Nickel disk specimens (10 mm in diameter and 1.5 mm thick) were cut out from a single crystal rod so as to have the surface perpendicular to the<110> crystal axis. The surface of the disks were treated by mechanical polishing following electrolytic polishing. Concentration ofimpurity elements in the nickel single crystal metal is tabulated in table 1. Two specimens were prepared as follows;

Specimen A) Phoshphorous ions P^+ were implanted as an impurity element into a single crystal nickel disk. Implanted area is 5 mm in diameter. The energies of the P^+ ions, which were 50,75 and 150 keV were selected

Table.1 Composition of impurity elements in single crystal Ni

Element:	Al	Ca	Cu	Fe	Mg	Si	Ag	C
ppm :	<1	1	<1	10	<1	1	<1	40

so that the ions distribute homogeniously in the region from the surface to about 1000 A depth. From calculation of a computer code TRIM85, total amount of the P^+ ion fluence is 5.0×10^{15} P/cm^2 which corresponds to about 0.37 atomic % in the implanted region and the avarage radiation damages induced is about 7 dpa.

Specimen B) 140 MeV Ni^{10+} ions accelerated by the TANDEM accelerator of JAERI were irradiated to a specimen, which was also prepared by the same manner as the specimen A, to give homogenious radiation damages all over the range where the phosphorous ions were implanted. Total fuluence of the Ni^{10+} ions were 5.0×10^{15} Ni/cm^2 and the ion range in the nickel metal was about 9 μm from the surface. Displacement damage of about 3.7 dpa were homogeniously given to the phosphorous implanted region in the specimen, also calculated by the TRIM85 computer code.

Using channeling technique, measurements of RBS and also PIXE measurements were performed to evaluate the radiation damages and to investigate the lattice location of P. 1.8 MeV He^+ ion beams accelerated by a Van de Graaff accelerator of Government Industrial Research Institute, Osaka, were used as an analyzing beam. A surface barrier type solid state detector were set for detecting backscattered He^+ ions at an angle of 165 degree to the incident He^+ ion beam and a Si(Li) detector for induced X-ray detection at an angle of 135 degree.

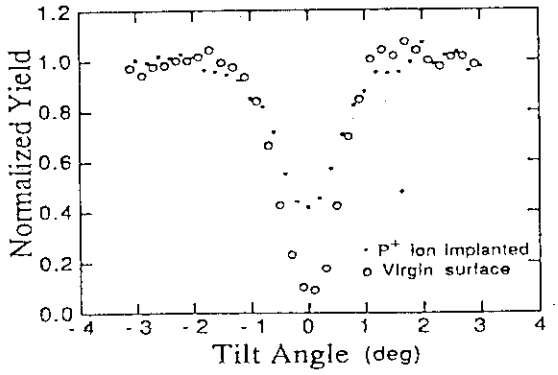

Fig.1 Normalized RBS yields obtained from the specimen A.

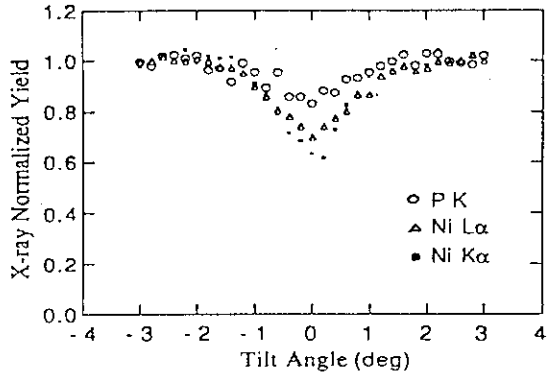

Fig.2 Normalized X-ray yields obtained from the specimen A.

Result and Discussion

Fig.1 shows the normalized RBS He^+ ion yields obtained from the specimen A. The solid dip-curve corresponds to the yield obtained from the unimplanted portion, and the dashed curve to the P^+ implanted portion. The minimum yield χ_{min}(unimp)=0.09 and double half-angle $2\psi_{1/2}$(unimp) =1.2° for the unimplanted portion. On the other hand, χ_{min}(P)=0.43 and $2\psi_{1/2}$(P) =1.2° for the P^+ ion implanted portion. A χ_{min}(cal) estimated from an equation proposed by Lindhard[2] is 0.023 for the fcc nickel metal. From this value, a ratio of the concentration of disorder atoms, N_D, to the one of bulk, N, in atoms per cubic centimeter is

$$N_D/N=(\chi_{min}(unimp)-\chi_{min}(cal))/1-\chi_{min}(cal)=0.069.$$

This would be a tentative criteria for degree of crystalization of the unimplanted specimen. Substituting the χ_{min}(unimp) and χ_{min}(cal) to χ_{min}(p) and χ_{min}(unimp), respectively, disorder concentration induced by P^+ ion implantation is obtained as 0.37, indi- cating about 40 % of atoms were displaced by P^+ion implantation. In fig.2, examples of angular distribution of the normalized X-ray yields obtained from the PIXE measurements are shown. The minimum yields of P K, Ni Kα and Ni Lα X-rays are 0.85, 0.63 and 0.74, respectively. Theminimum yields of Ni Kα X-ray from the unimplanted portion, not shown in the figure, was 0.26. Using this value, a ratio of the concentrationof disorder atoms to the one of bulk was calculated as 0.50. Although this value is a little larger than the value 0.47 which was obtained from the RBS measurements, agreement is rather good. Fig.3 shows comparisons of X-ray spectra obtained from the specimen A (fig.3a) and the specimen B (fig.3b). The upper spectra in the both figures correspond to random spectra where He^+ ion beams were incident to the specimens from random direction. The lower spectra correspond to aligned spectra where He^+ ion beams were incident along the <110> crystal axis. In the case of the specimen B, there appear two X-ray peaks corresponding to Si-K and S-K X-rays. These two peak intensities were held constant as a function of tilt angle of the specimen to the incident beam, hence theymight be surface contamination brought during Ni^{10+} irradiation. As shown in fig.3, intensity of the P K X-ray peak is almost the same as that of the Ni L X-ray in the spectra of the specimen A, which were onlyimplanted with P^+ ions. However, decrease in P-K X-ray intensity is seen in the spectra of the specimen B, which was implanted with P^+ ions following 140 MeV

Ni^{10+} ion irradiations. Peak intensity ratios, (P-K)/(Ni-K), in the random spectra of the specimen A and the specimen B are 0.19 and 0.09, respectively. P atom concentration reduces by half in the Ni^{10+} ion irradiated specimen B. It may be suggested that this ratio decrease is a consequence of RIS of P atoms induced by Ni^{10+} ion irradiations. In the aligned spectra, these peak intensity ratios are 0.29 and 0.22 for the specimen A and 2, respectively. Decrease in P K X-ray intensity in the aligned spectra is also shown, but it is less than that in the random spectra. This fact means that some of the P atoms locate at the interstitial site in the fcc lattice structure of nickel initially, and the P atoms tend to concentrate to the interstitial site during irradiation. P atoms may locate at the octahedral site of the fcc lattice structure or the site forming a dumbbell structue which is a combination of a P atom and a displaced Ni atom. The exact position of P atoms can not be assigned from the results of the present experiments. However, the relatively larger X-ray yield of P atoms in the <110> aligned spectrum may reflect the lattice position of P atoms in the RIS process.

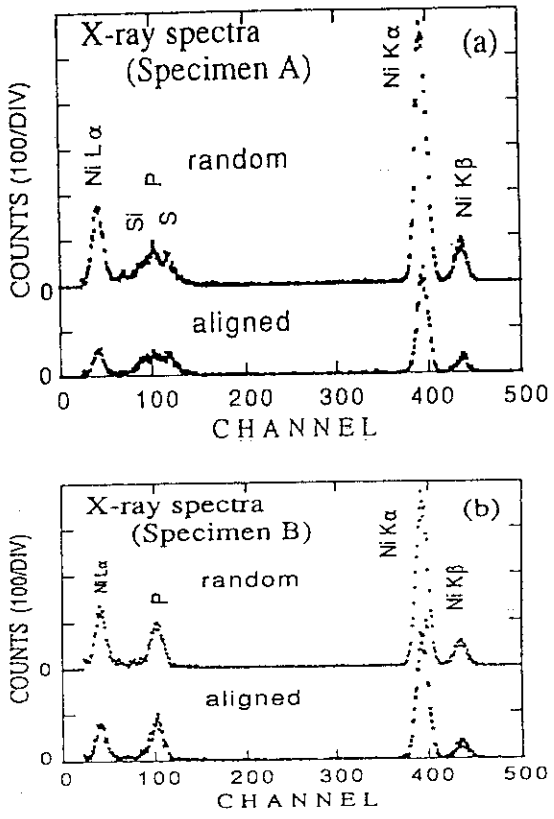

Fig.3 X-ray spectra obtained from (a) the specimen A, (b) the specimen B. In both figures, the upper and lower spectra coresponds to random and aligned spectra, respectively.

References

1)T.MITAMURA, M.TERASAWA, K.KOTEAZAWA, H.IWASAKI, K.KAWATSURA, T.NAKAI, Nucl. Instrum. & Methods B48(1990)470

2)Ion Beam Handbook for Material Analysis, Eds. J.W.Mayer and E.Rimini (Academic Press, New York, 1977) ch.3

2.7 CASCADE STRUCTURE IN ION-IRRADIATED COPPER AND GERMANIUM

Chiken KINOSHITA, Toshio NISHIO, Hiroaki ABE, Ken-ichi FUKUMOTO, Tadao IWATA*, Akihiro IWASE* and Yukio KAZUMATA*

Department of Nuclear Engineering, Kyushu University
*Department of Physics, JAERI

Introduction

When crystals are irradiated with fast neutrons, the kinetic energy of neutrons is transferred to primary knock-on atoms (PKA). PKA are ions consisting of constituent elements and have wide variety of kinetic energy (E_p). The high energy PKA produce "cascades" in which high concentration of point defects are localized. Therefore, in order to understand the radiation damage process of neutron irradiated materials, it is indispensable to get information about the structure of cascades and their kinetic behavior as a function of E_p. High energy ions also deposit E_p in accordance with the depth from the incident surface and produce corresponding cascades. The first objective of the present work is to establish a sectioning method for preparing TEM specimens which provide direct observation of cascades as a function of the depth of target materials. The second objective is to get knowledge of the structure of cascades through TEM observation.

Experimental

In this work, Cu and Ge were used as specimens, because they show clear contrasts corresponding to clusters through TEM observation.

(1) Bulk specimens of 99.998% Cu (2 x 2 x 20 mm) were prepared and one surface of the each specimen was subjected to 100 MeV I^{7+} irradiation to fluences of 8.3×10^{17} and 5.3×10^{19} ions/m^2 at room temperature using the TANDEM accelerator at JAERI. Irradiated specimens were electroplated with Cu until their diameter became about 8 mm, and then, they were cut into disks using an acid cutter. The final thinning was made by electropolishing, and TEM observation was perfomed using JEM-200BS in HVEM Laboratory, Kyushu University.

(2)Parallelopiped specimens of Ge (1 x 1.5 x 5 mm) were cut out of bulk material. One surface of each specimen was polished using abrasive papers

and finally done using paste of 0.25 μm diamond powders. The polished specimens were glued to an aluminum holder for irradiation using Aron Ceramics. The polished surface of each specimen was irradiated with 80 MeV Si^{9+} ions at a flux of 1 x 10^{14} ions/m^2s to a fluence of 3 x 10^{18} ions/m^2at ambient temperature using the TANDEM accelerator at Department of Physics, Kyushu University. After irradiation, the specimens were taken off the holder, and Aron Ceramics was scraped off the specimens. The irradiated surface was glued to a surface of an unirradiated specimen using an adhesive. The glued specimen was sealed into a Ni tube of 3 mm of diameter with Aron Ceramics. Discs of 300 μm thick were cut out of the tube. The disc was thinned using a dimpler, and the boundary between the irradiated and unirradiated surfaces near the center of the disc was thinned to electron transparency by chemical polishing using an aqueous solution of HNO_3, HF and CH_3COOH [1]. TEM observation was carried out using JEM-200BS at the HVEM Laboratory.

Results and Discussion

Weak-beam electron micrographs were taken along the direction of ion beam for irradiated specimens and show up tiny defect clusters (~ 5 nm). The volume density of defect clusters was measured, and it is shown in Fig. 1 as a function of the distance from the incident surface for a specimen irradiated to a low fluence of 3.4 x 10^{17} ions/m^2. The density of defect clusters increases with the increasing depth and reaches the maximum value at about 6.5 μm from the surface. The depth profiles of damage were calculated for 100 MeV I^{7+} irradiation through the TRIM code with 80 and 90 keV for the threshold energy of sub-cascades, and they are also shown in Fig.1. The calculated value through the TRIM code with about 80 keV for the threshold energy shows fairly good coincidence with experimental values. Fig.2 is the same as Fig.1, but for a specimen irradiated to a higher fluence of 2.4 x 10^{19} ions/m^2. In contrast to Fig.1, the density of defect clusters for a high fluence hardly shows the dependence on the depth from the surface. The result is attributed to the overlapping of defect clusters because of a too large fluence.

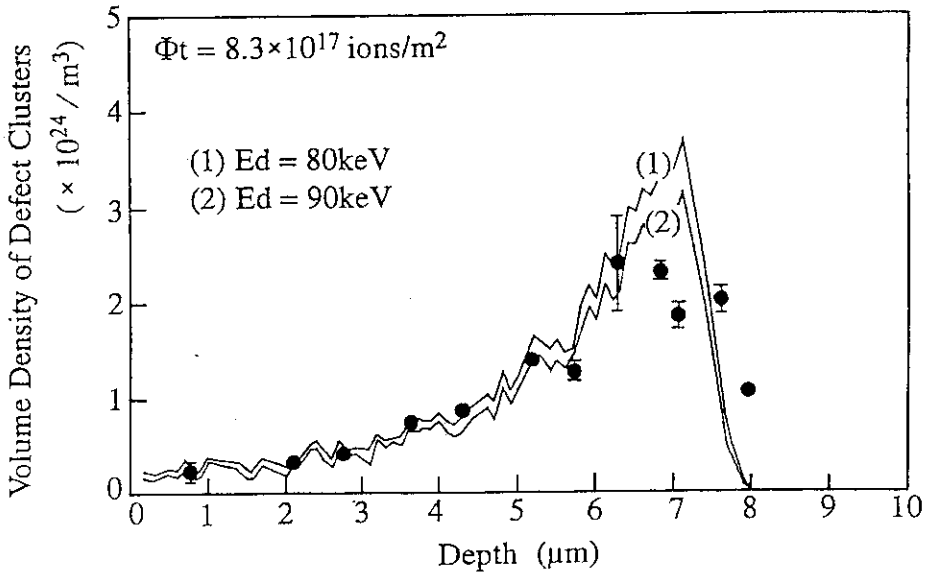

Fig. 1. The depth dependence of the volume density of defect clusters in Cu irradiated with 8.3 x 10^{17} 100-MeV I^{7+}/m^2. Solid lines (1) and (2) are calculated through the TRIM code with 80 and 90 keV for the threshold energy of sub-cascades, respectively.

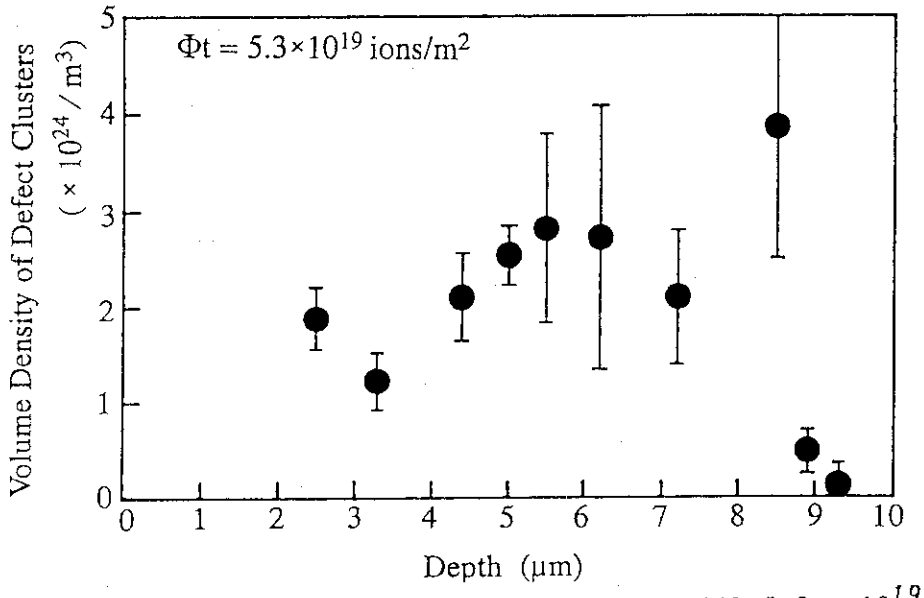

Fig. 2. Same as in Fig. 1, but for Cu irradiated with 5.3 x 10^{19} 100-MeV I^{7+}/m^2.

Weak-beam electron micrographs of irradiated Ge specimens were also taken along the direction of ion beam. Tiny defect clusters (3 ~ 4 nm) were observed and the size of the clusters did not vary with the distance from the incident surface. The volume density of defect clusters is shown

in Fig. 3 as a function of the distance from the incident surface with the depth profiles of damage calculated for 80 MeV Si^{9+} irradiation through the TRIM code with 0.1, 5 and 50 keV for the threshold energy of sub-cascades. The density of defect clusters increases with increasing distance and shows the maximum value at ~ 20 μm. The calculated value through the TRIM code with 50 keV for the threshold energy shows fairly good coincidence with experimental values.

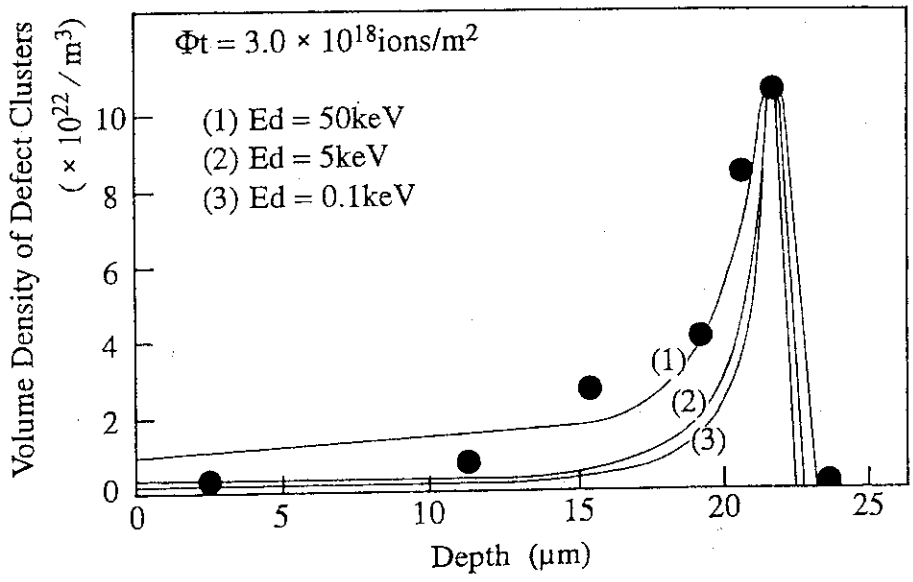

Fig. 3. Same as in Fig. 1, but for Ge irradiated with 3 x 10^{18} 80-MeV Si^{8+}/m^2. Solid lines are calculated through the TRIM code with 0.1, 5 and 50 keV for the threshold energy of sub-cascades.

Conclusion

Sectioning methods for preparing Cu and Ge TEM specimens, which are free from additional stress and contamination, are established and applied to the depth profile of the density of defect clusters. The depth profile is reproduced by the TRIM code with 90 ~ 100 keV for the threshold energy of subcascades of Cu and 50 keV for that of Ge.

Reference

(1) T. Nishio, Master thesis, Kyushu University, 1990.

2.8 X-RAY DIFFRACTION ON CARBON ION-IRRADIATED DIAMOND (II)

Hiroshi MAETA, Katsuji HARUNA*, Kazutosi OHASHI*,
Takuro KOIKE* AND Fumihisa ONO**

Department of Physics, JAERI, * Faculty of Engineering,
Tamagawa University, **College of Liberal Arts and
Sciences, Okayama University

1. Introduction

Diamond based semiconductor devices may turn out to be of great technological importance due to the outstanding physical properties, such as high thermal conductivity, good thermal and chemical stability . Ion implantation is a prime candidate technique for doping, but the issues of annealing radiation damage, avoiding graphitization, and driving implanted species into substitution sites have not been completely resolved.

In order to resolve this process, the damage due to self-implantation with 100 MeV C ions was studied by means of x-ray diffraction measurements of lattice parameters and diffraction profiles. We reported in previous paper[1] a increase of the lattice parameters and a remarkable increase of integrated intensities of x-ray diffraction profiles on a synthetic diamond single crystal after the ion-irradiations. In this work, we have report radiation effects of the diamond irradiated by 100 MeV carbon ion and 3 MeV electron so as to make the defects in diamond clear.

2. Experimental Procedures

The synthetic diamond single crystals used in this experiment were purchased of Sumitomo Denko Co.Ltd. The specimens were a type IIa crystals which are colored yellow and contain 1-10 ppm of nitrogen. The crystal size was 3.5 x 3.5x 0.3 mm^3 with the surfaces parallel to the (100) crystallographic plane. The specimens were irradiated with 100 MeV C^{+6} ion up to the fluences of 3.5 $x10^{15}$ ions/cm^2 at about liquid nitrogen temperature using TANDEM Accelerator. After the irradiation, the specimens were warmed

up to room temperature. The specimens were also irradiated at 60 C with 3 MeV electrons to a total dose of 1×10^{19} e/cm^2.

Measurements of lattice parameters have been made at room temperature by using the X-ray Bond method in which two counters were placed symmetrically. To attain the highest observable accuracy, a finely focused K line from an iron target was used, together with the highest possible reflection angle corresponding to the (100) planes. In the present experiment the (400) reflection was observed, for which $2\theta = 160.01°$. By using a fine slit of 0.2 mm in width, the Bragg reflections were measured at room temperature.

3. Results and Discussion

Figure 1 shows the relative change in lattice parameter before and after electron irradiations with the fluences of 3 Mev electrons. It can be seen that lattice expansion increased linearly with dose. This tendency is the same as that of C ion irradiation described in the previous report[1].

With self ion irradiation of 48 keV C ions the center of the irradiated region became amorphous at a fluence of 4×10^{16} ions/cm^2 [2]. In present work with the 100 MeV C^{+6} ion up to the fluences of 3.5×10^{15} ions/cm^2, the projected range was 102 μm. So, the damage was considered to be widely distributed .

The integrated intensities of the (400) diffraction profiles after the irradiations did change with fluence, extremely, after the ion irradiation. We measured the full width at half maximum (FWHM) of the diffraction profiles for the irradiated and nonirradiated diamond specimens. It can be seen that after the electron irradiation FWHM of profiles did not change. The results were summarized in Table 1 compared with that of ion irradiations.

The increases of the lattice parameter and unbroadening of profiles for the electron irradiated diamonds are presumed to be due to the formation of a point like defect and growth of defect clusters into dislocation loops. It is thought that the interstitial in diamond is mobile well below room temperature and the vacancy becomes mobile at 500 C [3]. Most of the radiation damage are present as interstitial dislocation loops and vacancies. The increase of integrated intensities is due to the extinction

effects which are associated with the point like defects and dislocation loops introduced by the ion and electron irradiations. This fact is confirmed by the results after the electron irradiation.

A more detailed analysis of the present results and a further experimental study are currently in progress.

References

[1] H. Maeta, K. haruna, K. Ohhashi, T. Koike and F. Ono ; JAERI Tandem, Linac & V.d.G. annual report 1989. p 65-68.

[2] R.S. Nelson, J.A. Hudson, D.J. Mazey, and R.C. Piller ; Proc Roy. Soc. Lond. **A 386**, 211 (1983).

[3] S. Gorbatkin, R. Zuhr, J. Roth and H. Naramoto : to be published.

Table I Full width at a half maximum (FWHM) and integrated intensisties of of self ion irradiated diamond with 100 MeV C^6 and 3 MeV electron.

100 MeV CARBON ION IRRADIATION

Fluence (10^{15} ions /cm^2)	FWHM (degree)	Integrated intensity I / I_0
unirradiated	0.17	1.0
0.68	0.20	4.2
2.4	0.23	4.9
3.6	0.23	5.8

3 MeV ELECTRON IRRADIATION

Fluence (10^{18} e /cm^2)	FWHM (degree)	Integrated intensity I / I_0
1.0	0.18	1.6
3.3	0.185	1.8
5	0.17	1.7
10	0.19	2.6

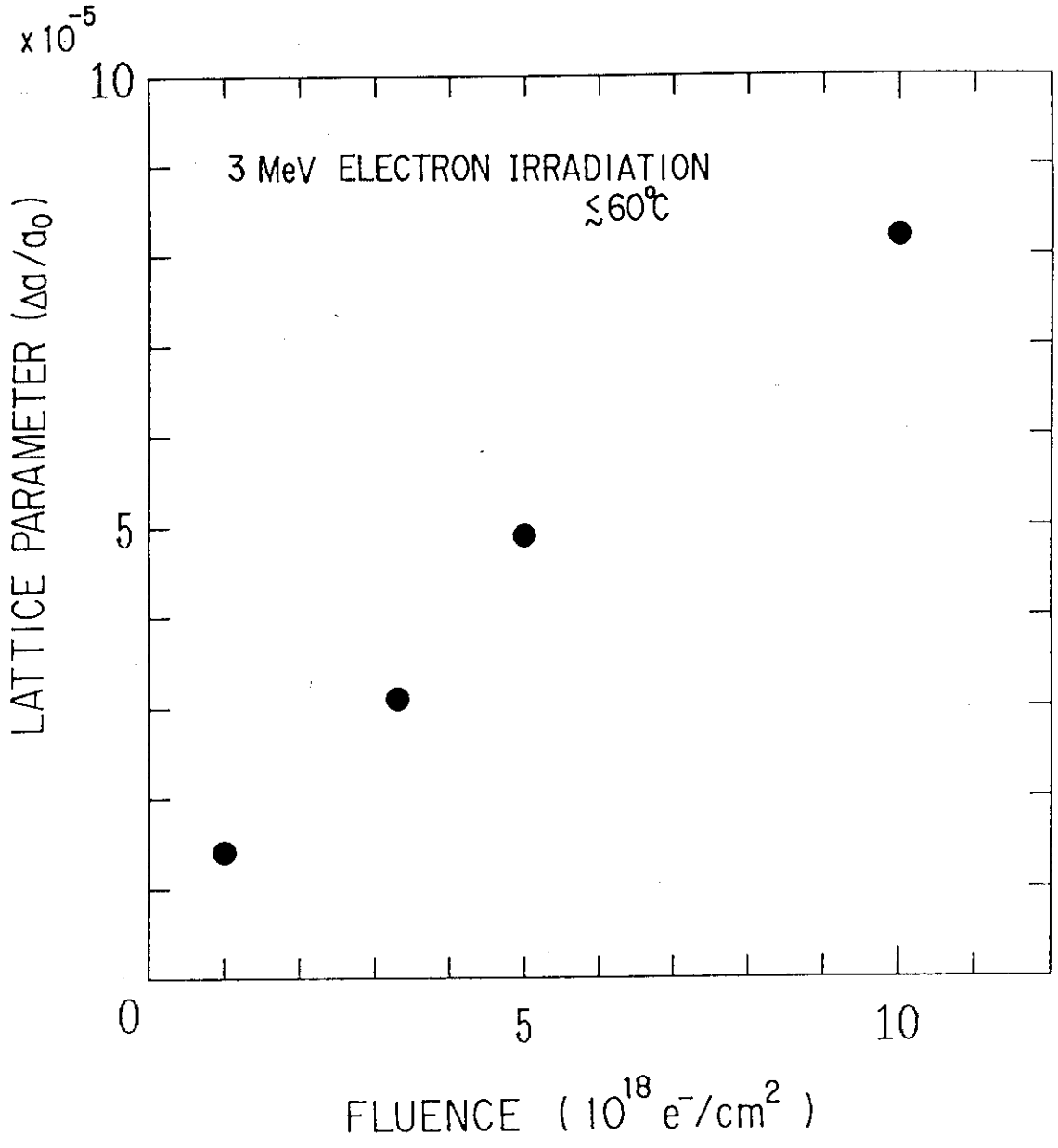

Fig. 1 The fractional increases of the lattice parameters of diamond with fluence of 3 MeV electron .

2.9 Effect of Electron-Excitation on Defect Production in Copper

Akihiro IWASE, Tadao IWATA, and Takeshi Nihira*

Department of Physics, JAERI, *Faculty of Engineering, Ibaraki University

In the previous paper[1], we showed that the damage efficiency in the ∿100 MeV heavy ion irradiations to Cu was extraordinarily enhanced compared with that in the low energy (∿1 MeV) ion irradiations. In this report, we present the result of defect production rate curves of Cu, and show that the electron-excitation by energetic ions can produce the lattice defects in Cu.

The specimens were thin foils of Cu about 0.2-0.25 μm thick. The irradiations of ∿1 MeV and ∿100 MeV ions were performed below 10 K using the 2MV VdG accelerator and the JAERI tandem accelerator, respectively. During the irradiations, the electrical resistivity change $\Delta\rho$ was measured as a function of ion-fluence Φ. Figure 1 shows the example of the analysis of defect production rate curves. The figure shows that the defect production rate curve can be expressed as the sum of two exponential functions of ion-fluence. From the slope and the value of defect production rate at Φ=0, we can determine the radiation annealing cross-section σ_r, and the defect production cross-section σ_d, respectively[1].

In Fig. 2, the damage efficiency for "defects 2" corresponding to the second part of defect production rate curve $\sigma_{d2}/\sigma_{d\ cal}$ is plotted as a function of the PKA median energy $T_{1/2}$, where $\sigma_{d\ cal}$ is the theoretical value of σ_d calculated under the assumption that only the elastic interaction produces the lattice defects. For low energy and high energy ions, $\sigma_{d2}/\sigma_{d\ cal}$ decreases monotonically with increasing $T_{1/2}$. On the contrary, the damage efficiency for "defect 1" corresponding to the first part of the defect production rate curve $\sigma_{d1}/\sigma_{d\ cal}$ cannot be well scaled by the PKA median energy.

In Fig. 3, the defect production cross section for "defect 1" σ_{d1} is plotted as a function of electronic stopping power S_e. As can be seen in Fig. 3, there exists a strong correlation between the electronic stopping power and the defect production cross-section σ_{d1}, and σ_{d1} is proportional to $\sim S_e^{1.7}$. This result means that the electron-excitation by energetic ions can produce the lattice defects in Cu . As a large amount of electron-excitation causes a large number of lattice defects, the total damage efficiency $(\sigma_{d1}+\sigma_{d2})/\sigma_{d\ cal}$ is remarkably enhanced for high energy heavy ion irradiations.

Reference

1) T. Iwata and A. Iwase, Rad. Eff. and Defects in Solids, 113 (1990) 135.

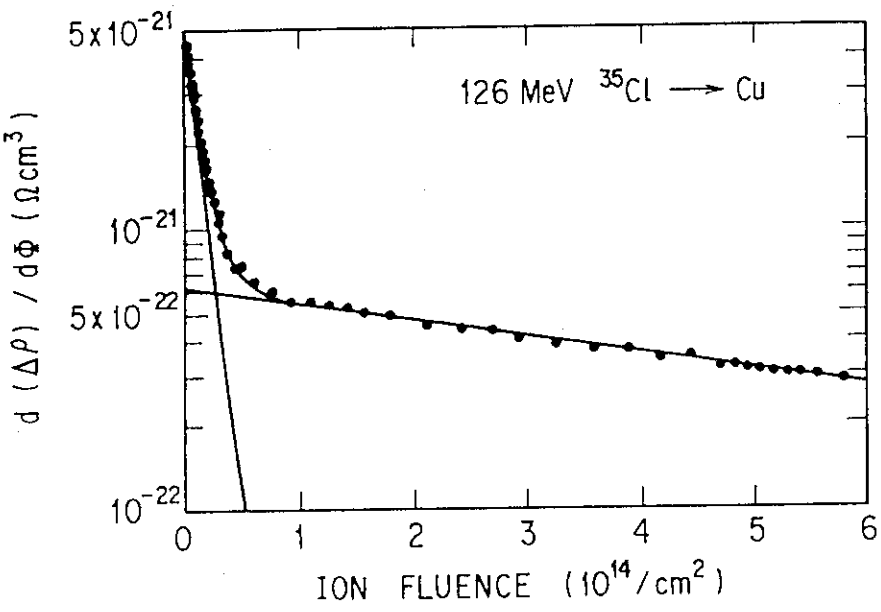

Fig. 1. Analysis of defect production rate as a function of ion-fluence in Cl-ion irradiated Cu. Experimental data (solid circles) can be fitted by the sum of two exponential functions of ion-fluence.

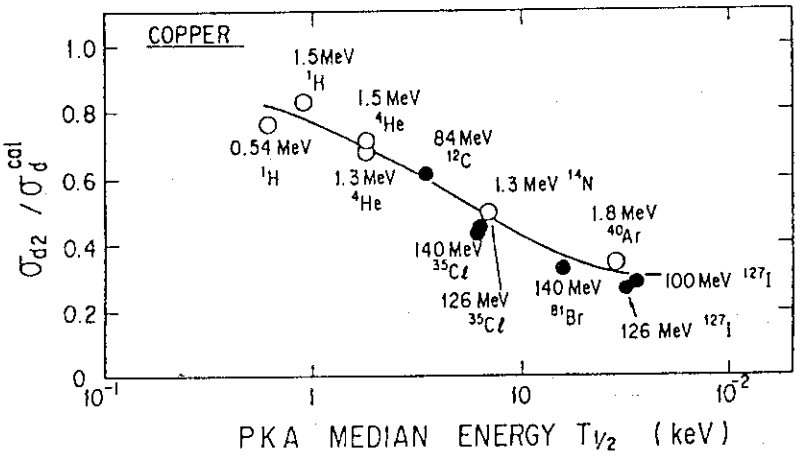

Fig. 2. Damage efficiency for "defect 2" as a function of $T_{1/2}$.

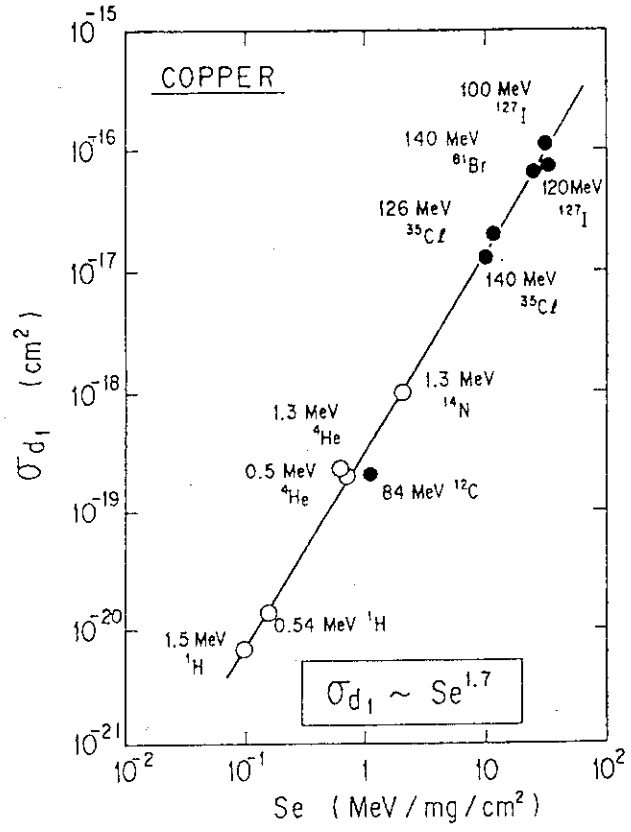

Fig. 3. Defect production cross-section for "defect 1" as a function of electronic stopping power.

2.10 Effect of 120 MeV O Ion Irradiation at Liquid Nitrogen Temperature on Superconducting Properties of Bi-Pb-Sr-Ca-Cu-O

Akihiro IWASE, Mitsuo Watanabe, Tadao Iwata and Takeshi Nihira*

Department of Physics, JAERI, *Faculty of Engineering, Ibaraki University

In this paper, we present the effect of 120 MeV oxygen ion irradiation at 77.3 K on transition temperature Tc, critical current Ic and electrical resistance just above Tc in the Bi-Pb-Sr-Ca-Cu-O superconductor.

The specimen was made by sintering Bi_2O_3, $SrCO_3$, $CaCO_3$, PbO and CuO for a nominal composition of $Bi_{0.7}Pb_{0.3}SrCaCu_2O_x$. The irradiation of 120 MeV O ions to the total fluence of $3.5\times10^{14}/cm^2$ was performed at 77.3 K. Figure 1 shows the electrical resistance of the specimen before and after the irradiation to the fluence of $3.5\times10^{14}/cm^2$ as a function of temperature. Figure 2 shows the electrical resistance around the transition region for several fluences. Figure 3(a) shows the transition temperature Tc and the electrical resistance just above the transition region (120 K) as a function of fluence. Figure 3(b) shows the dependence of the critical current at 77.3 K on ion fluence. The initial decrease rate of Tc and Ic are obtained as $\sim$7 deg/10^{14}O cm^{-2} and $\sim$0.3mA/10^{14}O cm^{-2}, respectively. In the case of $YBa_2Cu_3O_{7-x}$, the decrease rate of Tc was $\sim$1 deg/10^{14}O cm^{-2} [1], which is much smaller than that in the present experiment. Figure 4 shows that a linear correlation exists between Tc and the electrical resistance at 120 K. Such a linear correlation has been found also in $YBa_2Cu_3O_{7-x}$ [1]. The effects of annealing up to 300 K are shown in Fig.1 and Figs. 3-5. Figures 1 and 5 show that the annealing causes a slight change in temperature -resistance curve only below 100 K. The temperature dependence of electrical resistance above 100 K was not changed by annealing. This result is very different from that for $YBa_2Cu_3O_{7-x}$ [1]. In the case of

$YBa_2Cu_3O_{7-x}$, about 30 % of irradiation-induced resistance increment was recovered above ∿160 K during the annealing up to 300 K. In the present experiment, although the recovery of the electrical resistance was not found, the recovery of Tc and Ic was observed. After the irradiation to the fluence of $3.5 \times 10^{14}/cm^2$, Tc decreased to below 77.3 K. By the annealing up to 300 K, Tc recovered to ∿78 K, and Ic recovered from 0.085 mA to 0.12 mA (See Fig. 3(b) and Fig. 5).

Reference

1) A. Iwase, M. Masaki, T. Iwata, S. Sasaki and T. Nihira: Jpn. J. Appl. Phys. 27 (1988) L2071.

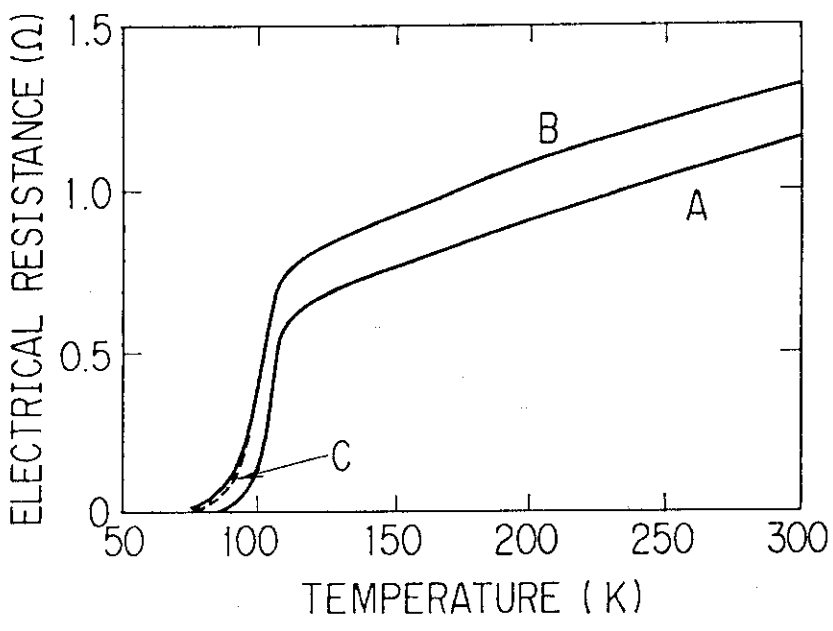

Fig. 1. Electrical resistance of Bi-Pb-Sr-Ca-Cu-O (A) before irradiation and (B) after O ion irradiation up to the fluence of $3.5 \times 10^{14}/cm^2$. Curve (C) presents the result after annealing up to 300 K. The measuring current is 0.1 mA.

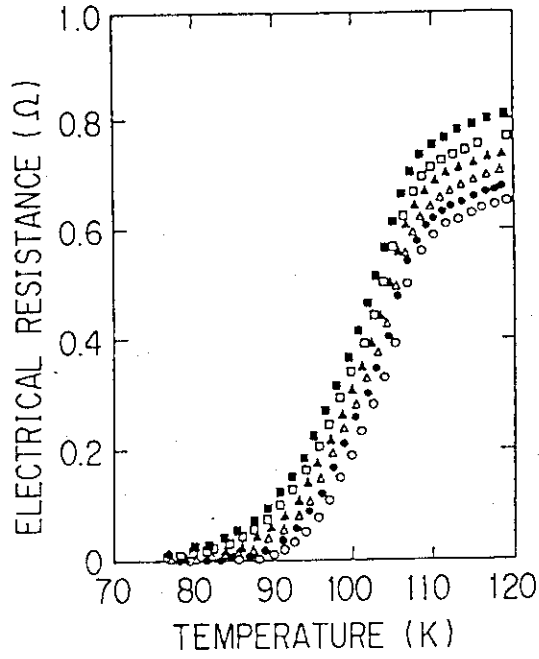

Fig. 2. Electrical resistance of Bi-Pb-Sr-Ca-Cu-O around the transition region for several O ion fluences. ○ Φ=0 (before irradiation), ● $3.12\times10^{13}/cm^2$, △ $7.58\times10^{13}/cm^2$, ▲ $1.38\times10^{14}/cm^2$, □ $2.22\times10^{14}/cm^2$ and ■ $3.47\times10^{14}/cm^2$. Measuring current is 0.1 mA.

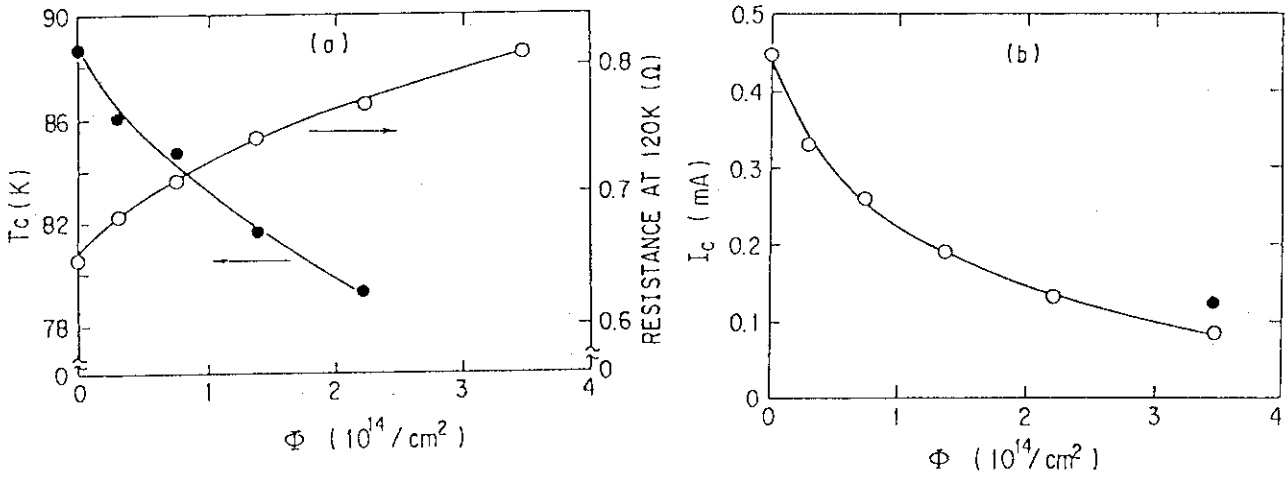

Fig. 3. (a) Electrical resistance at 120 K and transition temperature Tc as a function of O ion fluence. Measuring current is 0.1 mA. (b) Critical current Ic at 77.3 K as a function of O ion fluence. Solid circle presents the result after annealing up to 300 K.

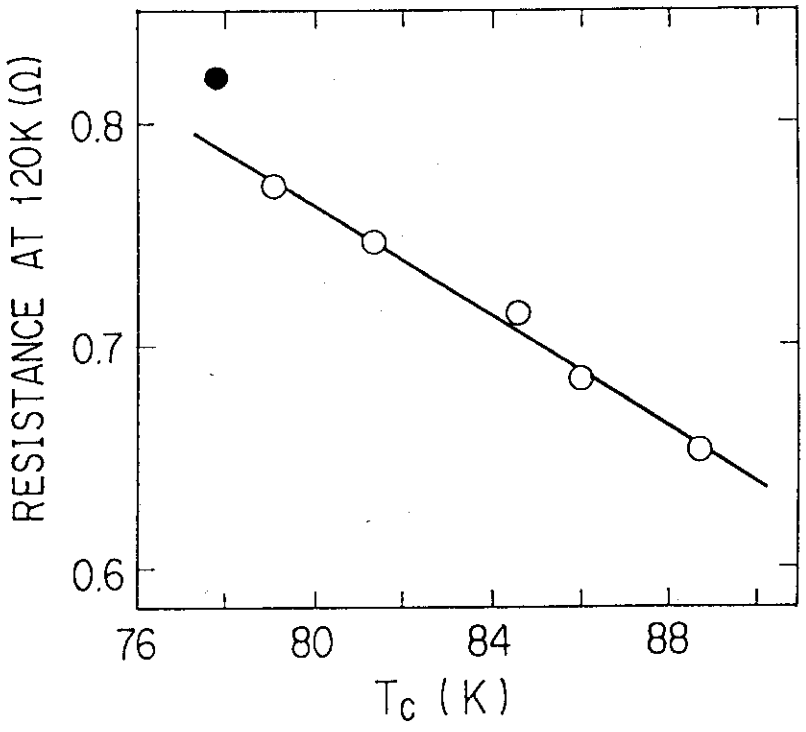

Fig. 4. Correlation between Tc and electrical resistance at 120 K. Solid circle presents the result after annealing up to 300 K.

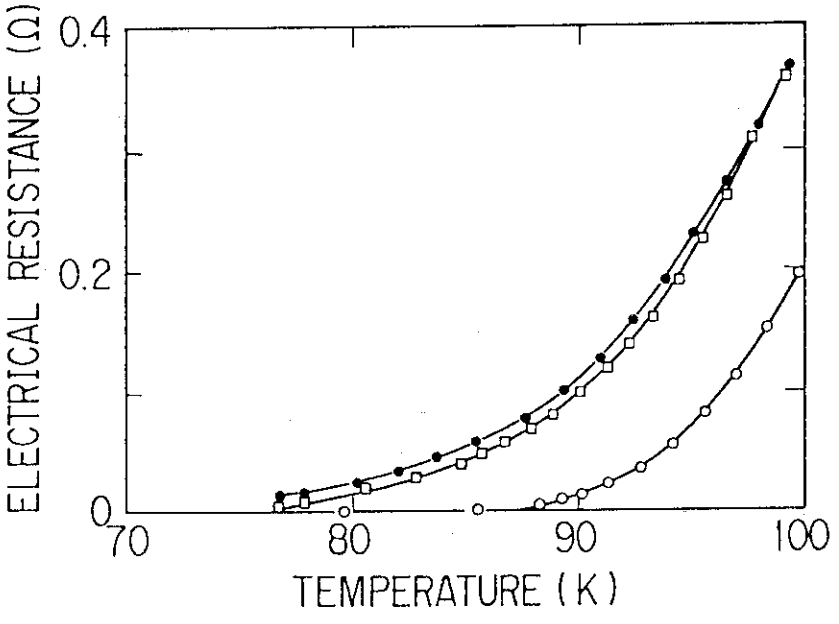

Fig. 5. Electrical resistance of Bi-Pb-Sr-Ca-Cu-O below 100 K before irradiation (open circles), after O ion irradiation to the fluence of $3.5 \times 10^{14}/cm^2$ (solid circles) and after annealing up to 300 K (open squares). Measuring current is 0.1 mA.

2.11 MAGNETIC FLUX MOTION OF SUPERCONDUCTING Bi-Sr-Ca-Cu-O FILMS AFTER ION IRRADIATION

Takeo ARUGA, Saburo TAKAMURA*, Taiji HOSHIYA**
and Mamoru KOBIYAMA***

Department of Fuels and Materials Research, *Department of Physics, **Oarai Research Establishment, JAERI,
***Faculty of Engineering, Ibaraki University

The movement of flux lines in high Tc superconductors is given by the balance between Lorentz force exerted by transport current and pinning force, and is controlled by thermally activated process[1]. If the interaction between flux lines and pinning centers introduced by ion irradiation is strong, the activation energy and therefore the critical current density as well, may be increased compared with those before irradiation. This report describes the results on thermally activated processes in the flux line motion, based on the temperature dependence measurement of electrical resistances in the low resistance region in Bi-Sr-Ca-Cu-O films after room-temperature He-ion irradiations.

The details of the sample and the experimental methods in the present work have been described elsewhere [2,3]. Magnetic field supplied was perpendicular to both the film surface and the current direction. The temperature dependence of electrical resistances was measured under various magnetic fields up to 2 T at a current density of $5\times10^5 A/m^2$, before irradiation and after the 400-keV He-ion irradiations at room temperature up to doses from 2 to 19 $\times10^{18}/m^2$. The ion dose of $10^{19}He/m^2$ is predicted to correspond to a defect concentration of 0.3% in the present sample.

The resistances measured with a temperature sweep under each magnetic field for the irradiations up to $1.9\times10^{19}/m^2$ are given as a function of temperatures in Fig.1. The transition curves obtained by the resistive method are broadened by the application of the magnetic field. However, the broadening becomes small with increasing the ion dose, although the transition temperatures decrease. As a result, the resistance-temperature curves rise more sharply for the higher doses,

which implies that the motion of flux lines is interrupted by pinning centers produced by the ion irradiation. From Arrhenius plots of the logarithm of electrical resistivities against T^{-1}, which give straight line sections, the thermally activated behaviors are apparent in the motion of the flux line. Effective activation energies estimated U^* are 0.086 eV (H=0.68T) and 0.080 eV(H=1.4T) before irradiation, and 0.10 eV (H=0.68T) and 0.085 eV(H=1.4T) after irradiation of $2.0\times10^{18}/m^2$, and 0.12 eV (H=0.68T) and 0.11 eV(H=1.4T) after irradiation of $5.0\times10^{18}/m^2$, respectively. Under the same magnetic field applied, the effective activation energies after irradiation are slightly larger than that before irradiation and increase with increasing doses. However, the energies for the higher field are the smaller, which suggests that the effective potential hight under the magnetic field decreases with increasing applied magnetic field; the potential well is tilted by the Lorentz force acting on the flux lines.

The temperature dependence of the electric voltage measured using another sample of a Bi-Sr-Ca-Cu-O film[4] at various electric currents between 0.02 and 110 mA and at magnetic fields up to 2 T perpendicular to the film plane is plotted in Fig. 2, as the relationship between the logarithm of electric voltages and the reciprocal temperatures, before and after the irradiation of $1.0\times10^{18}/m^2$. The effective activation energies U^* obtained from the slope of lines for equal measuring electric current and magnetic field are slightly smaller after the irradiation compared with that before irradiation, especially for the larger electric currents. The relationship between U^* and the effective transition temperature Tc^* defined as a temperature at which the electrical voltage has a value of $5\times10^{-6}V$, is shown in Fig. 3, before and after the irradiation.

It is noticed that the value of U^* before irradiation shows a tendency of saturation under the magnetic field above a temperature Ta which is indicated by arrows in Fig. 3. At temperatures above Ta, a new flux phase[5], for example, the flux liquid, may come into existence, and U^* has a constant value. The saturated U^* and Ta decrease with increasing magnetic field[6]. The flux liquid has been discussed in studying the elastic response of flux lattice to the pinning centers. The motion of flux lines changes from hysteretic to viscous at a temperature above which no increase in loss has been observed. The

melting temperature decreases with increasing magnetic field, which is demonstrated in the behavior of Ta in the present work. The value of U^* after irradiation rides on almost the same curve as that before irradiation, which implies that effective pinning energy would be decreased. When sufficient pinning centers exist before irradiation, an introduction of additional pinning centers may flatten the potential well to diminish the effectiveness for flux pinning. The definite enhancement of the critical current, therefore, can not be observed as long as the electrical resistance method is used.

References

1) Y. Yeshurun and A. P. Malozemoff, Phys. Rev. Lett. 60 (1988) 2202.
2) T. Aruga, S. Takamura, T. Hoshiya and M. Kobiyama, Jpn. J. Appl. Phys. 28 (1989) L964.
3) T. Hoshiya, S. Takamura, T. Aruga and M. Kobiyama, Jpn. J. Appl. Phys. 29 (1990) L1443.
4) T. Hoshiya, S. Takamura, T. Aruga and M. Kobiyama, Jpn. J. Appl. Phys. 29 (1990) L2026.
5) P. L. Gammel, L. F. Schneemeyer, J. U. Waszczak and D. J. Bishop, Phys. Rev. Lett. 61 (1988) 1666.
6) S. Takamura, T. Hoshiya and T. Aruga, Appl. Phys. Lett. 56 (1990) 1582.

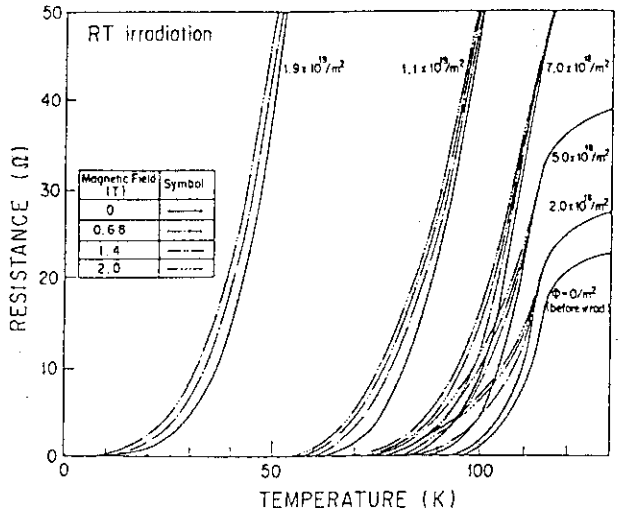

Fig. 1. Temperature dependence of electrical resistances under various magnetic fields applied before and after 400-keV He ion irradiation.

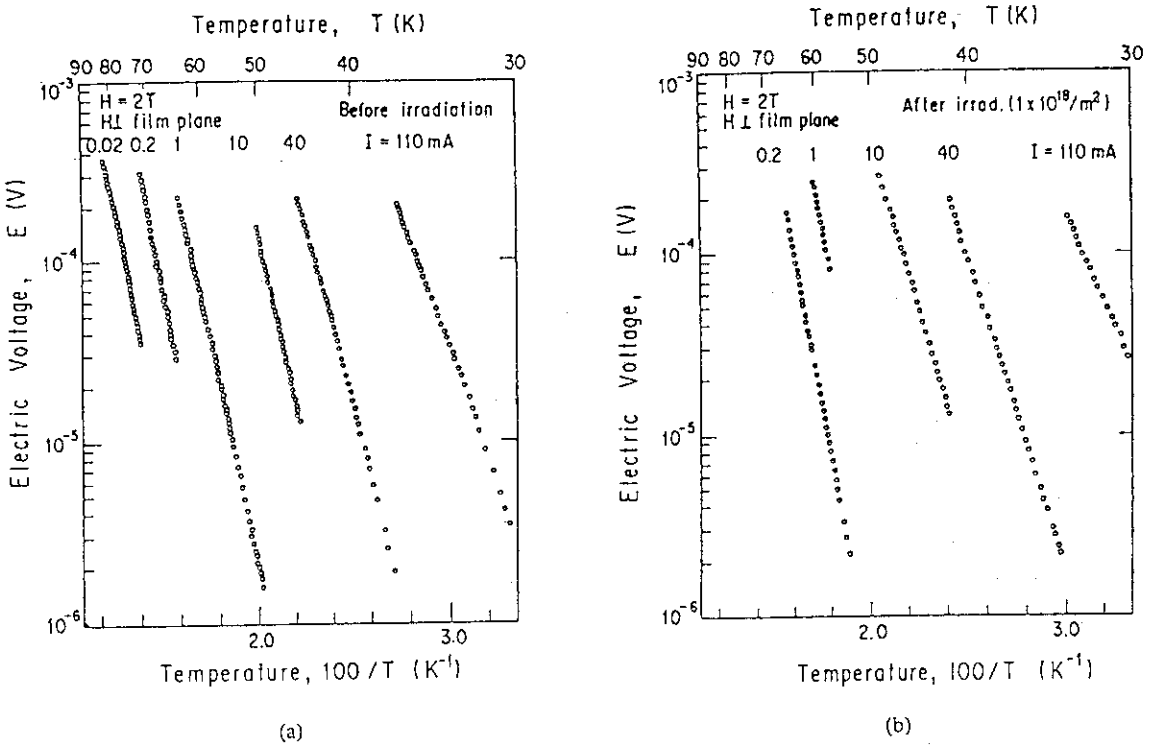

Fig. 2. Arrhenius plots of electric voltage (a) before and (b) after 400-keV He irradiation to a dose of $1x10^{18}/m^2$ with various electric currents under a magnetic field applied of 2 T.

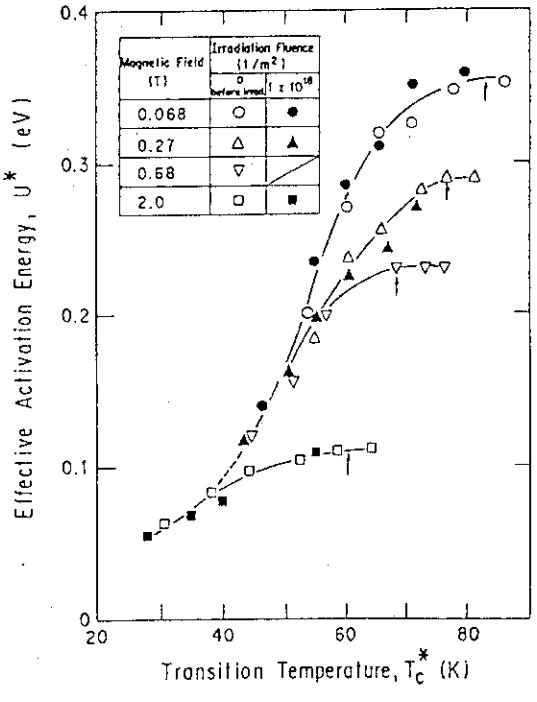

Fig. 3. Relationships between effective activation energy U^* and transition temperature Tc^* at which the electric voltage has a value of $1x10^{-6}V$ under various magneticfields applied before and after 400-keV He ion irradiation to a dose of $1x10^{18}/m^2$.

Ⅲ ATOMIC PHYSICS

3.1 RADIAL DOSE DISTRIBUTION FOR HIGH ENERGY HEAVY IONS IN ARGON GAS

Katsutoshi FURUKAWA, Shin-ichi OHNO,
Hideki NAMBA*, and Yoshihide KOMAKI

Department of Chemistry, *Department of Research (Takasaki)

1. Introduction

In microdosimetry of high-energy heavy ions, two kinds of information are of fundamental importance; (1) the ratio of the deposited energy going into kinetic energy of atoms to that going into electronic excitations or ionizations, and (2) the spatial distribution of the deposited energy around the track of an incident heavy ion.

As to information on (1), we aimed at experimental determinations of W-value, mean energy required to produce an ion-electron pair, of Ar gas as a function of primary energy of the incident particle in a previous report.[1] We tried then to compare the results with those obtained from the estimation using LSS theory[2] of how the initial energy is divided into electronic and "nuclear" energies of the irradiated material. A general agreement of the results with the theory was obtained in that the fraction of the energy that goes into kinetic energy of gas atoms due to "nuclear collision" becomes larger as the incident particle is heavier in mass and lower in energy. However, we also noticed there that our experimental results showed a significant deviation from the theory.

In the present report, we present our results on the measurements of the spatial distribution of the deposited energy around the track of an incident heavy-ion beam. For measurements, we employed the method which have been reported by Wingate and Baum[3] and which measures radial

distribution of ionization current produced in a small wall-less ionization chamber.

2. Experimental

A collimated beam of the heavy ion of the energy range 100-200 MeV from the JAERI Tandem accelerator is introduced in the vessel filled with a gas through a set of aperture (of the diameter of 0.2 and 0.5 mm) which serves also differential pumping system. A schematic view of the apparatus is shown in Fig. 1. Details of the chamber were reported previously.

The small wall-less ionization chamber (b) is consisted of two cylindrical meshes and a central wire supported by Teflon insulator. The inner cylindrical mesh (of diameter 15 mm, length 85 mm) which acts as H.V. electrode is made of Ni wire of diameter 0.005 mm, 50 meshes. The outer mesh acted as a shield and was made of SUS wire of diameter 0.21 mm, 30 meshes. The central wire which acts as the collecting electrode is made of 1 mm Cu wire.

The wall-less ionization chamber is placed in a large vessel filled with an Ar gas at variable pressure and it is movable by remote operation. The radial distance from the ion-beam track during measurements was adjusted by changing either the gas pressure or the radial position of the wall-less

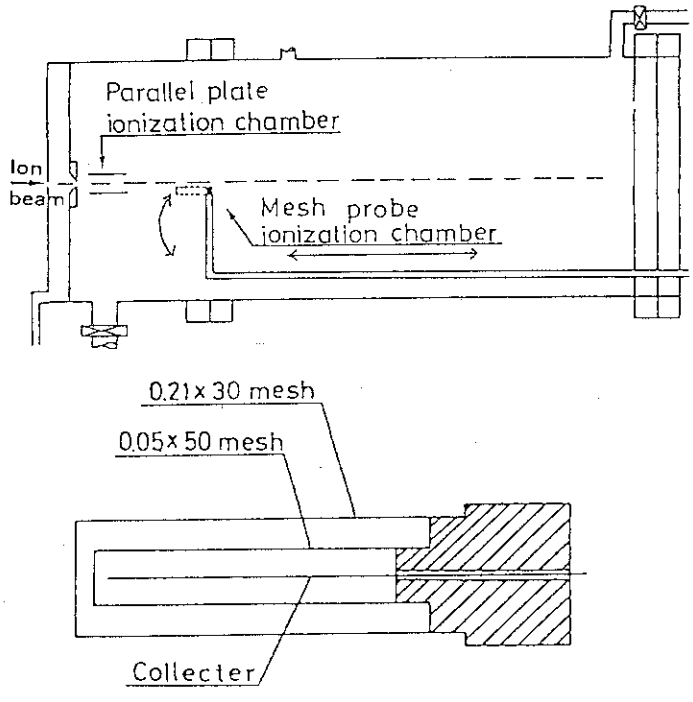

Fig.1 Schematic view of the ionization chamber

ionization chamber.

3. Results and Discussion

The results obtained have been normalized as follows. Simulated radial distance R:

$$R = R_{gas} (d_{gas}/d_{water})$$

where R_{gas} is the observed distance, d_{gas} and d_{water} are the density of Ar gas used and the density of the liquid water, respectively. Dose in eV/g at the distance of R is:

$$Dose = (I_p/I_i) (ZW_e/(v \cdot d_{gas})) (d_{water}/d_{gas})^2$$

where I_p and I_i are the ionization current in the small wall-less chamber and the incident ion-beam current, respectively and where Z the charge of the incident ion, W_e W-value of the gas for electron (= 26.2 eV), and v the volume of the small wall-less ionization chamber.

In Fig. 2 is shown the radial distribution of absorbed dose obtained in Ar gas by a small wall-less ionization chamber at the various distance from the path of the incident 200 MeV Ni-ion. In this study the mesh chamber was placed at the radial distance of 35 ~ 77 mm from the beam path. The pressure in the chamber was varied from 0.25 to 40 Torr. The radial distance is all normalized to the density of 1 g/cm^3 as above. The results indicate that the radial distribution of the normalized absorbed dose decreases nearly 1/2.5 power law to the normalized radial distance.

References

1) K. Furukawa, S. Ohno, H. Namba, Y. Komaki, Y. Yamada, and Y. Nakai: JAERI-M 90-139, p. 43 (1990).

2) J. F. Ziegler: "Handbook of Stopping Cross-Section for Energetic Ions of All Elements," Pergamon Press, N. Y.

(1979).

3) C. L. Wingate and J. W. Baum: Radiat. Res., 65, 1 (1976).

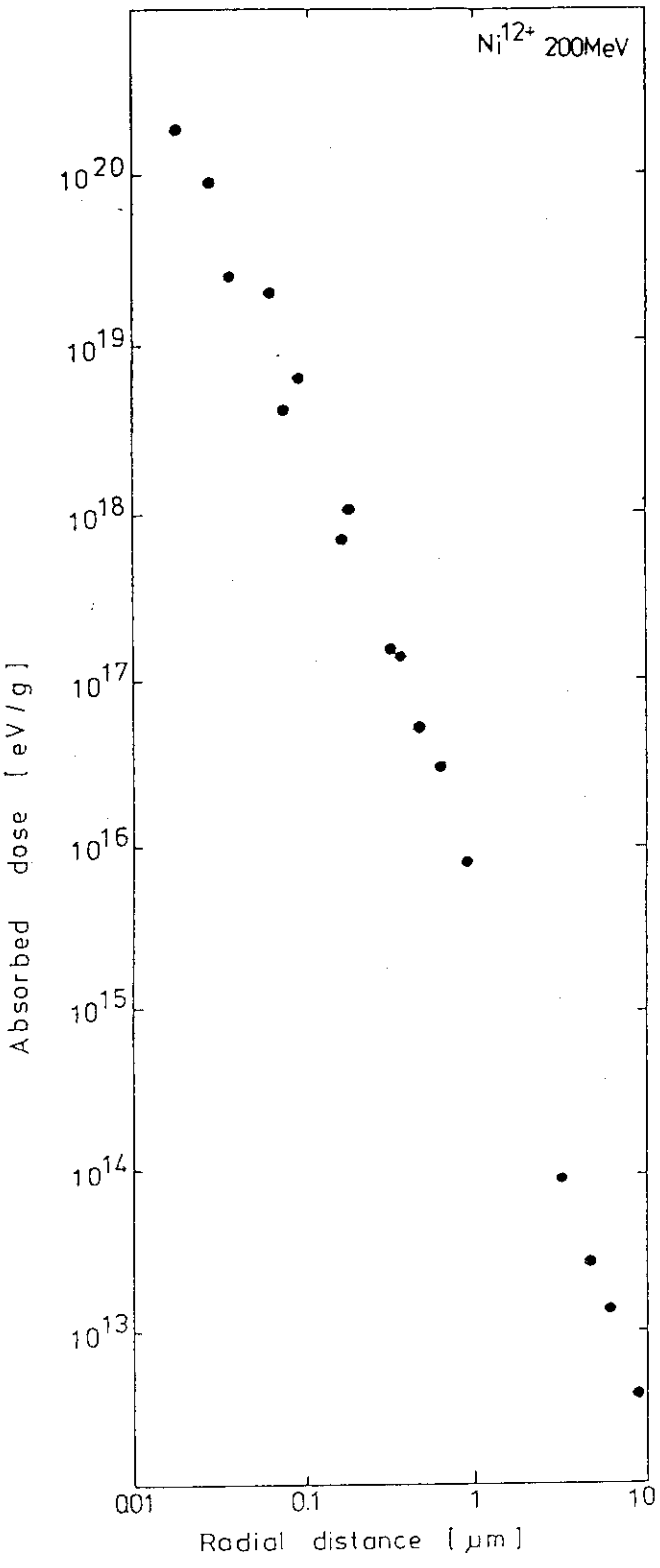

Fig.2 Absorbed dose as a function of simulated radial distance

3.2 HIGH-RESOLUTION ZERO-DEGREE ELECTRON SPECTROSCOPY (III)

Makoto IMAI, Masao SATAKA, Yasunori YAMAZAKI*, Ken-ichiro KOMAKI*, Kiyoshi KAWATSURA**, Yasuyuki KANAI*** and Hiroshi NARAMOTO

Department of Physics, JAERI, *College of Arts and Sciences, University of Tokyo, **Department of Chemistry, Kyoto Institute of Technology, ***The Institute of Physical and Chemical Research (RIKEN)

Introduction

Projectile Auger spectroscopy is known to be a versatile tool for investigating structures of Rydberg atoms[1]. Observing the autoionizing electrons emitted from Rydberg ion projectiles at zero degree with high resolution, we can measure a number of peaks coming from a series of Rydberg states. Previously, we measured electrons emitted from S^{12+} ions of $1s^2 2p9\ell$ Rydberg states excited through He and Carbon-foil targets. In these measurements, as had been obserbed for 1.5-5.0 MeV C^{2+} projectiles[2], we observed the difference between ℓ-distributions for higher Rydberg states excited through ion-atom and ion-solid collisions[3]. This difference is attributed to stochastic collision induced ℓ-diffusion of entrained electrons inside solids[4].

In the present work, we extended the measurement for electrons emitted from the states excited through He and Carbon-foils of various thicknesses (1.2-9.6 $\mu g/cm^2$), to investigate the equilibrating process of angular momentum distributions in foil targets.

Experiment

The experimental apparatus have already been described in detail[5]. Ions of 64MeV S^{6+} were accelerated by JAERI tandem accelerator, and passed a post stripper foil of 10-30 $\mu g/cm^2$ in thickness. The S^{12+} components were separated by a switching magnet, collimated in a diameter of about 1.5mm, and then collided with targets. The thicknesses of carbon foil targets were 1.2, 2.2, 9.6 $\mu g/cm^2$ and He gas target was used for exciting projectiles under the single collision condition. The He gas target cell is 5cm in length, while the target pressure being about 10^{-3}Torr. Electrons ejected in the beam direction were energy

analyzed by tandem electrostatic analyzer with high resolution and detected by MCP and Ceratron multiplyer for C-foils and He targets, respectively.

Results and Discussion

Figure 1 shows the electron energy spectra converted into projectile frame for electrons emitted from 64MeV S^{12+} excited through C-foil targets. The peaks around 1.2eV, which are the most dominant ones in the figure, is attributed to be compositions of the electrons emitted via Coster-Kronig transitions of $1s^22p9\ell$-$1s^22s\varepsilon\ell'$ (ℓ=d,f,g,...) by following procedures.

Neglecting the term splitting and the spin-orbit splitting, the energy of the ejected electrons can be written in the form below.

$$E_{nl} = \Delta E_{2s2p} - \frac{Q^2 Ry}{2(n-\mu_l)^2} ,$$

where ΔE_{2s2p} is the energy difference between the 2s and 2p orbitals, Q is the effective charge of the atomic core seen by the Rydberg electron, Ry is the Rydberg constant (27.211eV), n is the principal quantum number, and μ_l is the quantum defect depending on the angular momentum ℓ. As ΔE_{2s2p} and quantum defect μ_l, we used transition energy[6] of the $1s^22s$-$1s^22p\ {}^2P_{3/2}$ for S^{13+} and theoretical values[7], respectively. Here the transition from the state $^2P_{1/2}$ is energetically impossible. Labels in figure 1 show expected electron energy for specified angular momentum ℓ. The validities of this calculation is not clear for the states ℓ=s and ℓ=p, because the term splitting produced by the coupling of the Rydberg electron with the 2p electron is not negligible. Consequently, we can not conclude that peaks around the energies which correspond to ℓ=s and ℓ=p come from transitions of $1s^22p9\ell$-$1s^22s\varepsilon\ell'$ (ℓ=s,p).

Figure 2 shows the height of the peaks around 1.2eV plotted against the C-foil thickness. Figure 3 shows the peak width versus peak height ratios of the peaks around 1.2eV as a function of the C-foil thickness. In these figures, the heights of the peaks increase, and the width-height ratios become larger when the target thickness increases. The height and the ratio reach equilibrium at target thickness corresponding to C-foil of 2-4$\mu g/cm^2$. These results lead us to the following conclusions. 1) The $1s^22p9\ell$ (ℓ=d,f,g,...) states of 64 MeV S^{12+} produced in ion-solid collisions increase when target thickness increases. 2) Its ℓ-distribution shifts to higher-ℓ when target thickness increases. 3) It reaches equilibrium at target thickness

corresponding to C-foil of 2-4μg/cm^2.

The equilibrating behaviour of projectiles of other charge states and 128MeV projectiles, which are expected to include effects coming from "transfer excitation", "capture to excited states" processes and so on, are under investigation now.

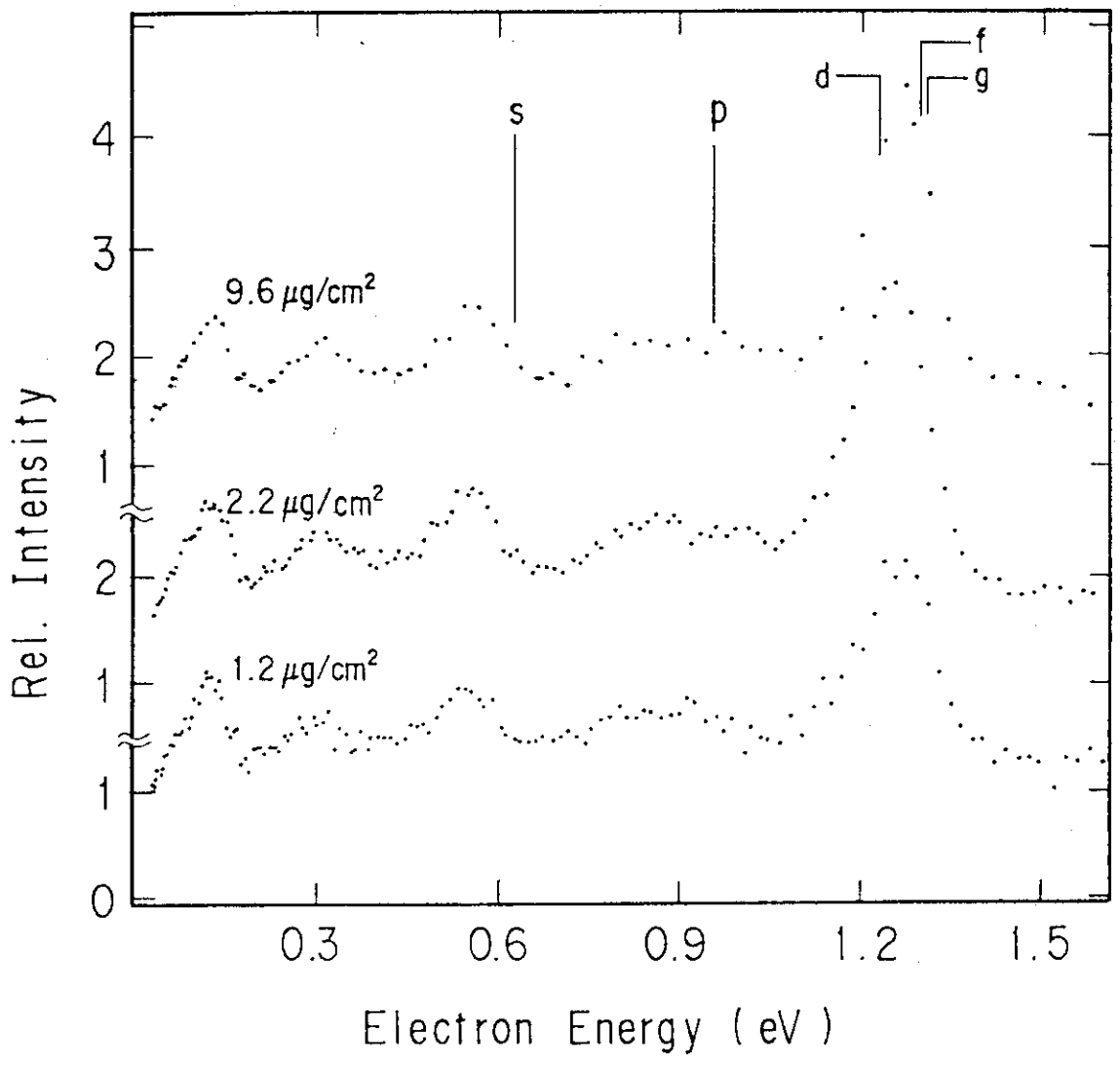

Fig.1 Electron energy spectra converted into projectile frame for electrons emitted from 64MeV S^{12+} $1s^2 2p9\ell$ states excited through C-foil targets. Labels show calcultated values of Auger electron energies emitted from specified ℓ states (see text).

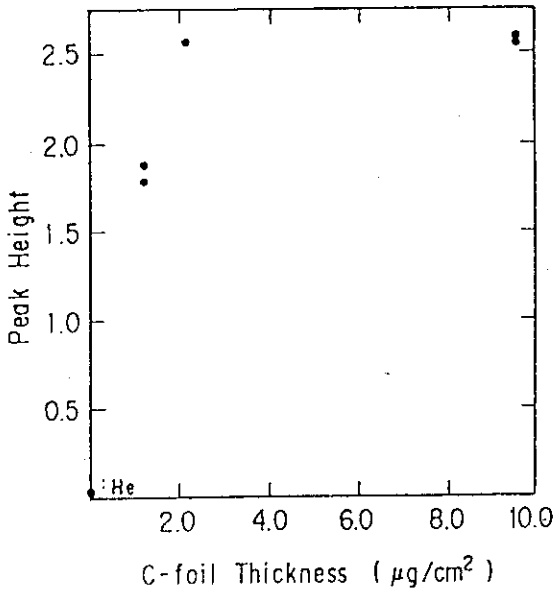

Fig.2 The height of the peaks around 1.2eV plotted against the C-foil thickness.

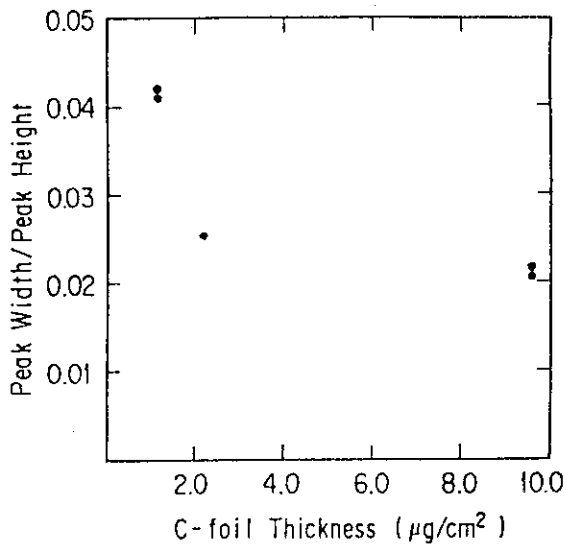

Fig.3 Peak width versus peak height ratios of the peaks around 1.2eV plotted against the C-foil thickness.

References

1) N.Stolterfoht: Phys. Reports 146 (1987) 315, section 5.5, and references therein.

2) Y.Yamazaki, N.Stolterfoht, P.D.Miller, H.F.Krause, P.L.Pepmiller, S.Datz, I.A.Sellin, A.Salin, P.D.Fainstein, R.Rivarola, J.P.Gradin, J.N.Scheurer, S.Andriamonje, D.Bertault and J.F.Chemin: Phys. Rev. Lett. 61 (1988) 2913.

3) K.Kawatsura, M.Sataka, Y.Yamazaki, K.Komaki, Y.Kanai, H.Naramoto, K.Kuroki, T.Kambara, Y.Awaya, Y.Nakai and N.Stolterfoht: Nucl. Instrum. & Methods B 48 (1990) 103.

4) J.Burgdörfer and C.Bottcher: Phys. Rev. Lett. 61 (1988) 2917.

5) K.Komaki, Y.Yamazaki, K.Kuroki, K.Kawatsura, M.Sataka, M.Imai, Y.Nakai, H.Naramoto, Y.Kanai, T.Kambara, Y.Awaya and N.Stolterfoht: JAERI Tandem, Linac & V.d.G. Annual Report 1989 p.53.

6) R.L.Kelly: J. Phys. Chem. Ref. Data 16 Supplement No.1 (1987).

7) C.D.Theodosius, M.Inokuti and S.T.Manson: At. Data Nucl. Data Tables 35 (1986) 473.

3.3 HIGH-RESOLUTION L-AUGER SPECTROSCOPY OF Sc^{9+} PRODUCED IN 90-MeV Sc^{8+} + He COLLISIONS

Ken-ichiro KOMAKI, Yasunori YAMAZAKI, Kenro KUROKI, Kiyoshi KAWATSURA*, Masao SATAKA**, Makoto IMAI**, Hiroshi NARAMOTO**, Yasuyuki KANAI***, Tadashi KAMBARA***, Yohko AWAYA***, Jorgen H. HANSEN+ and Nikolaus STOLTERFOHT++

College of Arts and Sciences, University of Tokyo, *Faculty of Engineering and Design, Kyoto Institute of Technology, **Department of Physics, JAERI, ***The Institute of Physical and Chemical Research(RIKEN), +University of Amsterdam, The Netherlands, ++Harn-Meitner Institute, Berlin, Germany

Introduction

High-resolution projectile Auger spectroscopy has been a powerful tool for investigation of the electronic structure of highly ionized atoms[1]. In particular, the method of zero-degree electron spectroscopy has been proved to be advantageous because of great reduction of Doppler broadening[2]. Furthermore, the use of light target atoms, such as He, provides selectively ionized projectile through the "needle ionization" process, where an inner shell electron is removed without disturbing the outer shells.

In the present work, we measure scandium L-Auger electrons produced in 89-MeV Sc^{8+} + He collision and investigate the electronic structure of Mg-like Sc^{9+} ions.

Experimental

The experimental arrangement is reported previously[3]. A beam of 89 MeV $^{45}Sc^{8+}$ ions were accelerated by the tandem accelerator at JAERI and were introduced to the collision chamber.

The target was He gas with a pressure of ~mTorr and the cell length of 5cm. Electrons emitted in the forward direction were energy analyzed by the tandem parallel-plate electrostatic analyzer. By decelerating the electrons before the second analyzer, the resolution of 3 eV (FWHM) at laboratory frame electron energy of 1850 eV was achieved. Through the transformation to the projectile frame of reference, the energy resolution

is improved to 0.78 eV at projectile frame electron energy of 177 eV.

Results and Discussion

Figure 1 shows a projectile frame energy spectrum of electrons emitted through 89-MeV Sc^{8+} + He collisions. Peaks in the spectrum were identified as L-Auger electrons emitted from the initial states $2s^22p^53s^23p(Sc^{9+})$ and $2s^22p^53s^2(Sc^{10+})$. A pair of peaks at 143.5 eV and 147.8 eV are attributed to the $2p^53s^2\ ^2P_{3/2,1/2}$ doublet produced by removing additional 3p electron in the "needle ionization" of a 2p electron. The rest of the spectral peaks are due to Mg-like Sc^{9+} and are attributed to the transitions to the final configurations, $2p^63s$, $2p^63p$ and $2p^63d$. The third transition involves three electrons, reflecting strong electron correlation in the initial state.

Similar spectral structures have been observed in L-Auger spectra from Mg-like Al^{+} [4] and Ar^{6+} [2] ions and were compared with theoretical results evaluated by configuration interaction Hatree-Fock code due to Cowan[5]. To account for the interaction between 2p hole and 3p electron in the initial state, configurations $2s^22p^5(3s^23p+3s3p3d+3p3d^2)$ were considered in the calculation. In the present case, however, it turns out that the results of the same method of calculation show a poor agreement especially for intensities of transitions to $2p^63d$ states and that the discrepancy is removed by taking configurations with a 2s hole into consideration as well.

The new calculation was performed within the intermediate coupling scheme using the wave function expanded as follows: $2s^22p^53s^2(3p+4p+5p+6p)+2s^22p^5(3s3p3d+3p3d^2+3p^3+3p^24p+3p4p^2)+2s2p^6(3s^23d+3d^3+3p^23d+3s3p^2)$.

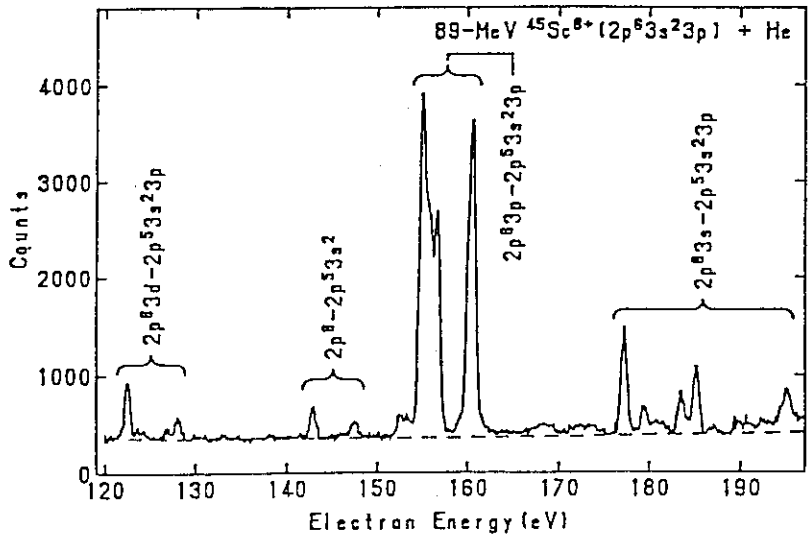

Fig. 1 L-Auger spectrum of Sc produced in 89-MeV Sc^{8+} + He collisions. The observation angle is 0°. The electron energy refers to the projectile frame.

Table Energies and intensities of L-Auger lines of Sc^{9+}.

transition	energy		relative intensity	
	theory	expt.	theory	expt.
$^2D_{5/2} - {}^3S_1$	120.25	120.2	0.003	0.02(2)
$^2D_{3/2} - {}^3S_1$	120.33		0.003	
$^2D_{5/2} - {}^3D_2$	122.40	122.5	0.31	3.4(4)
$^2D_{3/2} - {}^3D_2$	122.47		1.20	
$^2D_{5/2} - {}^3D_3$	122.53		2.25	
$^2D_{3/2} - {}^3D_3$	122.60		0.005	
$^2D_{5/2} - {}^1P_1$	123.49	123.5	0.011	0.41(10)
$^2D_{3/2} - {}^1P_1$	123.57		0.39	
$^2D_{5/2} - {}^3P_2$	124.07	124.2	0.51	0.41(10)
$^2D_{3/2} - {}^3P_2$	124.15		0.13	
$^2D_{5/2} - {}^3P_0$	126.40	126.4	0.003	0.055(40)
$^2D_{3/2} - {}^3P_0$	126.47		0.00014	
$^2D_{5/2} - {}^3D_1$	126.88	126.9	0.002	0.52(12)
$^2D_{3/2} - {}^3D_1$	126.96		0.66	
$^2D_{5/2} - {}^3P_1$	127.93	128.0	0.012	1.2(2)
$^2D_{5/2} - {}^1D_2$	127.98		1.12	
$^2D_{3/2} - {}^3P_1$	128.00		0.026	
$^2D_{3/2} - {}^1D_2$	128.05		0.38	
$^2D_{5/2} - {}^1S_0$	137.88	—	0.0018	0
$^2D_{3/2} - {}^1S_0$	137.96	—	0.0012	0
		total	7.02	6.0(8)
$^2P_{3/2} - {}^3S_1$	152.74	152.6	1.26	1.4(4)
$^2P_{1/2} - {}^3S_1$	153.57	153.4	0.75	1.3(4)
$^2P_{3/2} - {}^3D_2$	154.89	155.0	2.62	20.5(15)
$^2P_{3/2} - {}^3D_3$	155.02		16.04	
$^2P_{1/2} - {}^3D_2$	155.72	155.6	9.14	6.5(15)
$^2P_{1/2} - {}^3D_3$	155.85	155.9	0.21	7.7(15)
$^2P_{3/2} - {}^1P_1$	155.98		5.19	
$^2P_{3/2} - {}^3P_2$	156.56	156.7	12.87	11.0(15)
$^2P_{1/2} - {}^1P_1$	156.81	156.8	1.96	2.3(10)
$^2P_{1/2} - {}^3P_2$	157.39	157.5	0.23	0.13(10)
$^2P_{3/2} - {}^3P_0$	158.89	158.9	0.23	0.88(30)
$^2P_{3/2} - {}^3D_1$	159.37	159.4	0.52	0.23(15)
$^2P_{1/2} - {}^3P_0$	159.72	159.7	0.0003	1.4(5)
$^2P_{1/2} - {}^3D_1$	160.20	160.2	6.90	8.2(12)
$^2P_{3/2} - {}^3P_1$	160.42	160.5	3.69	12.6(15)
$^2P_{3/2} - {}^1D_2$	160.47		10.75	
$^2P_{1/2} - {}^3P_1$	161.25	161.3	0.88	0.91(15)
$^2P_{1/2} - {}^1D_2$	161.30		1.10	
$^2P_{3/2} - {}^1S_0$	170.37	—	0.094	0
$^2P_{1/2} - {}^1S_0$	171.20	—	0.054	0
		total	74.49	75.0(20)
$^2S_{1/2} - {}^3S_1$	177.29	177.2	6.32	6.6(4)
$^2S_{1/2} - {}^3D_2$	179.44	179.5	0.61	1.9(2)
$^2S_{1/2} - {}^3D_3$	179.57		0.94	
$^2S_{1/2} - {}^1P_1$	180.53	180.5	0.78	0.65(20)
$^2S_{1/2} - {}^3P_2$	181.11	181.2	0.149	0.72(20)
$^2S_{1/2} - {}^3P_0$	183.44	183.5	2.54	2.3(5)
$^2S_{1/2} - {}^3D_1$	183.92	183.9	0.25	0.52(15)
$^2S_{1/2} - {}^3P_1$	184.97	185.0	3.73	4.2(4)
$^2S_{1/2} - {}^1D_2$	185.02		0.54	
$^2S_{1/2} - {}^1S_0$	194.92	194.8	2.63	2.1(6)
		total	18.49	19.0(10)

To distinguish ten resulting states, the largest LSJ term is used as label. Assuming a statistical population of the initial states, the line intensities were calculated for 50 transitions between these ten initial states and five final states, $2s^2 2p^6 3s\ ^2S_{1/2}$, $2s^2 2p^6 3p\ ^2P_{1/2,3/2}$, $2s^2 2p^6 3d\ ^2D_{3/2,5/2}$. The result is presented in Fig. 2 and Table together with the result of the deconvolution of the experimental data. Intensities are normalized to the total values of 100. In Fig. 2, position and length of the vertical lines represent theoretical energies and intensities, respectively. An excellent agreement is achieved both in the energy and intensity values.

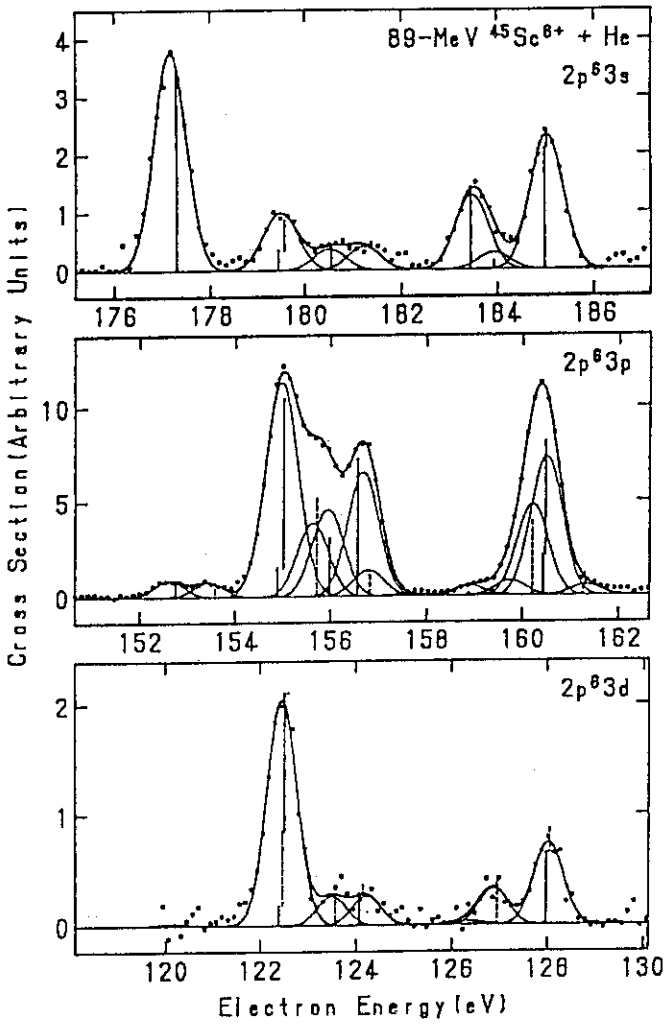

Fig. 2 Line structure of L-Auger spectra from Sc^{9+} $2p^5 3s^2 3p$ configuration.

References

1) A. Itoh, T. Schneider, G. Schwietz, Z. Roller, H. Platten, G. Nolte, D. Schneider and N. Stolterfoht: J. Phys. B16(1983)3965.

2) P. Focke, T. Schneider, D. Schneider, G. Schiwietz, I. Kádár, N. Stolterfoht and J. H. Hansen: Phys. Rev. A40(1989)5633.

3) K. Kawatsura, M. Sataka, Y. Yamazaki, K. Komaki, Y. Kanai, H. Naramoto, K. Kuroki, T. Kambara, Y. Awaya, Y. Nakai and N. Stolterfoht: Nucl. Instrum. and Methods B48(1990)103.

4) R. Malutzki, A. Waschter, V. Schmidt and J. H. Hansen: J. Phys. B20 (1987)5411.

5) R. D. Cowan: The Theory of Atomic Structure and Spectra(University of California Press, Berkeley, 1981)Chapter 7-14.

Ⅳ NUCLEAR CHEMISTRY

4.1 A COLLINEAR LASER-ION-BEAM SPECTROSCOPY SYSTEM

Yoshinori NAKAHARA, Hideki IIMURA, Shin-ichi ICHIKAWA, Kazuhiro KOTANI*, Masanori WAKASUGI** and Takayoshi HORIGUCHI***

Depertment of Chemistry, JAERI, *Department of Nuclear Engineering, Nagoya University, **RIKEN, ***Faculty of Science, Hiroshima University

The purpose of the JAERI-ISOL project is to investigate the structure of short-lived nuclei which are prepared by means of an isotope separator coupled to the tandem accelerator in JAERI. So far, work at JAERI-ISOL has concentrated on the electron- and gamma-spectroscopy of neutron deficient nuclei in the A=120-130 mass region, so that level energies and γ-transition properties in these nuclei have been investigated. It is interesting to supplement this investigation with measurements of nuclear moments derived from optical hyperfine structure (hfs). Thus we installed a collinear laser-ion-beam spectroscopy system at JAERI-ISOL. The purpose of this system is to measure hfs in radioactive isotopes with sub-Doppler resolution.[1] We report here on results of tests performed by using stable isotope ^{141}Pr.

The experimental setup is shown in Fig.1. A cw dye laser with wavemeter (Coherent 699-29) was pumped with an Ar-ion laser (Coherent INNOVA-100-20) and controlled by a personal computer. As a dye, we used Rhodamine 6G. The wavemeter was used to determine the absolute frequency which was calibrated by an absorption spectrum of an I_2 cell. The relative frequency of the hyperfine lines was calibrated by a confocal etalon with free spectral range of 150 MHz (Burleigh CFT-500).

A beam of 40-kV Pr^+ ions, part of which are in metastable levels, was produced by the JAERI-ISOL mass separator. The metastable ions were excited to upper levels by a counter-propagating laser beam. The interaction region was defined by a cage of 10 cm in length and 4 cm in diameter, which was kept at the potential of -3 kV. This potential ensures that the velocity of the ions is Doppler-tuned into resonance in the cage and that depopulation pumping of the metastable levels does not occur far upstream from the cage.

Resonance was observed by detecting the fluorescence light from the excited levels to the ground level. The fluorescence light was collected by a spherical mirror onto a cooled photomultiplier (HAMAMATSU Photonics R943-02). Stray light from the laser beam was suppressed by an appropriate combination of a broad-band filter and a narrow-band interference filter. The ion current was monitored by a Faraday cup (FC) after the interaction region. Typical ion beam current was about 50 nA. Hyperfine spectra were measured by scanning the laser frequency of about 20 GHz and recorded in multi-channel scaling (MCS) mode by using a personal-computer-based data acquisition system.

Typical hyperfine spectrum for PrII from the metastable $^5G_2^0$ level to the $^5H_3$ level (λ=601.94 nm) is shown in Fig.2. All the hyperfine components were well resolved and assigned, as shown in Fig.2. The observed linewidth is typically about 90 MHz (FWHM). The magnetic-dipole constant A and the electric-quadrupole constant B were derived from the measured hyperfine spectra. Part of results are summarized in ref.2.

The overall efficiency for detecting the fluorescence photons is about 10^{-8} photons/ion. The background is about 10^3 counts/s, and it arises mainly from two things. One thing is the scattered laser light, and the other is light originating from collisions between the ions and the gas atoms remaining in the interaction chamber.

The observed linewidth is sufficent for our needs. More important one is sensitivity, because the mass-separated yield is estimated to be below 10^5 ions/s in on-line experiments. Thus reduction of the backgrounds and improvement of the overall efficiency are necessary. We are now attempting to improve collection efficiency of the fluorescence photons and to increase population of the metastable states.

REFERENCE

1) S.L.Kaufman:Opt.Commun. 17(1976)309.

2) H.Iimura, Y.Nakahara, S.Ichikawa, K.Kotani, M.Wakasugi and T.Horiguchi, J.Phys.Sci.Jpn. 59(1990)4208.

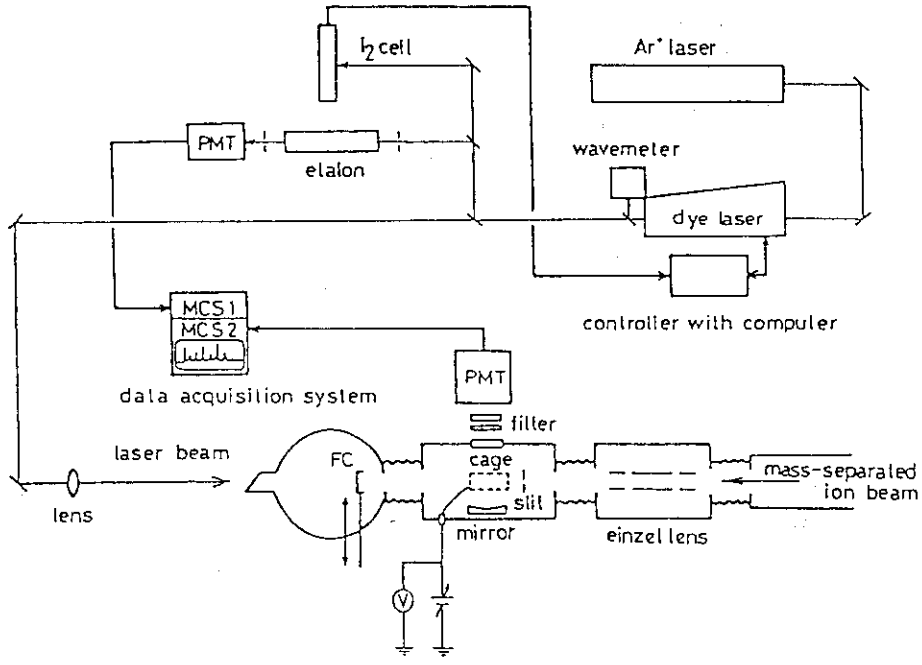

Fig.1. Experimental setup for collinear laser-ion-beam spectroscopy.

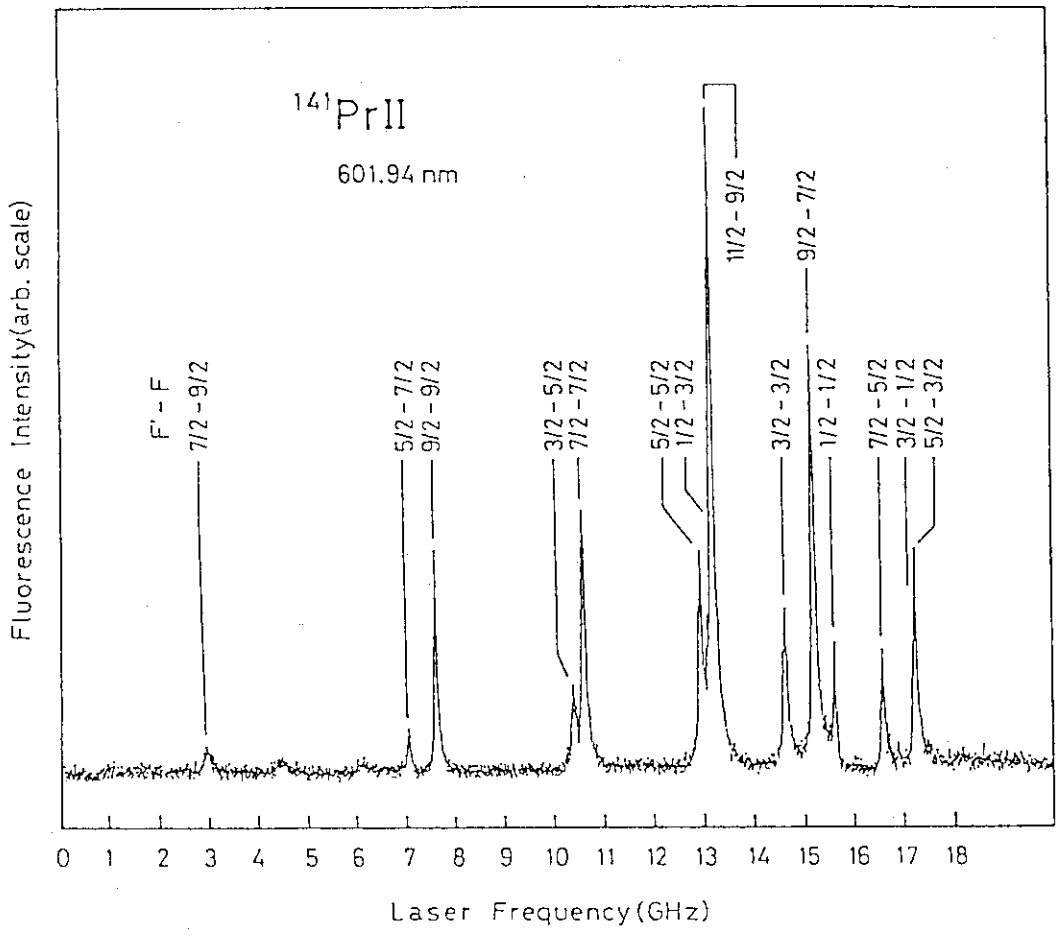

Fig.2. Typical measured hyperfine spectrum.

4.2 DECAY OF ^{122}La

Toshiaki SEKINE,[1] Shin-ichi ICHIKAWA,[2] Tsuneyasu MORIKAWA,[1,4]
Masumi OSHIMA,[3] Akihiko OSA,[2,5], Yuichi Hatsukawa,[1]
Hideki IIMURA[2] and Nobuo SHINOHARA[2]

[1]Department of Radioisotopes, [2]Department of Chemistry, and
[3]Department of Physics, JAERI, [4]Faculty of Science, Hiroshima
University, [5]School of Engineering, Nagoya University

The present work is part of a systematic study on the decay of neutron defficient nuclei in the rare-earth region. The decay of ^{122}La was investigated previously by the present authors.[1)] Although the experiment suggested the existence of a side band in its daughter nucleus, ^{122}Ba, the counting statistics in γ-γ coincidence measurement was not enough to establish its band. In the present work the γ-γ coincidence measurement has been carried out again to obtain information on the nuclear structure of its daughter ^{122}Ba.

The ^{122}La isotope was produced by bombarding a ^{92}Mo target with a ^{35}Cl beam delivered by the tandem accelerator and mass-separated on-line as ^{122}La^{16}O^{+} ions, being separated from the Cs and Ba isobars.[2)] The γ-γ coincidence measurement was performed using a BaF_2 scintillation detector and a HPGe detector.

Figure 1 shows a γ-ray spectrum obtained previously for ^{122}La. In addition to γ-rays of the ground band, three new γ-rays were observed at 743, 940 and 972 keV. The results of the γ-γ coincidence measurement indicate that the 743- and 972-keV γ-rays are coincident with the 197-keV $2_1^+ \rightarrow 0_1^+$ γ-ray but the 940-keV γ-ray isn't (see Fig.2). From the coincidence relation, new levels of 939.6 and 1169.0 keV are introduced into a level scheme, as shown in Fig.3.

The systematics of lowlying levels in this region is shown in Fig.4. From this systematics it seems natural to conclude that the 939.6-keV level is the band head of the quasi-γ band and has a spin/parity of 2^+. The 1169.0-keV level is considered to be also a member of the quasi-γ band and to have a spin/parity of 3^+.

One can note in Fig.4 that the energy of the 2_2^+ state decreases slightly with decreasing neutron number, arrives at a minimum and then starts increasing at ^{122}Ba. It is interesting that Puddu *et al.*[3)] predicted this trend of the 2_2^+-level energy by applying the IBM-2. Their prediction of the branching ratio between $2_2^+ \rightarrow 2_1^+$ and $2_2^+ \rightarrow 0_1^+$ transitions is in good agreement with our experimental value.[1)] The calculation of the IBM-2 suggests that in the Ba isotopic chain the nuclear structure changes from O(6) around ^{134}Ba towards SU(3) around ^{122}Ba.[3)]

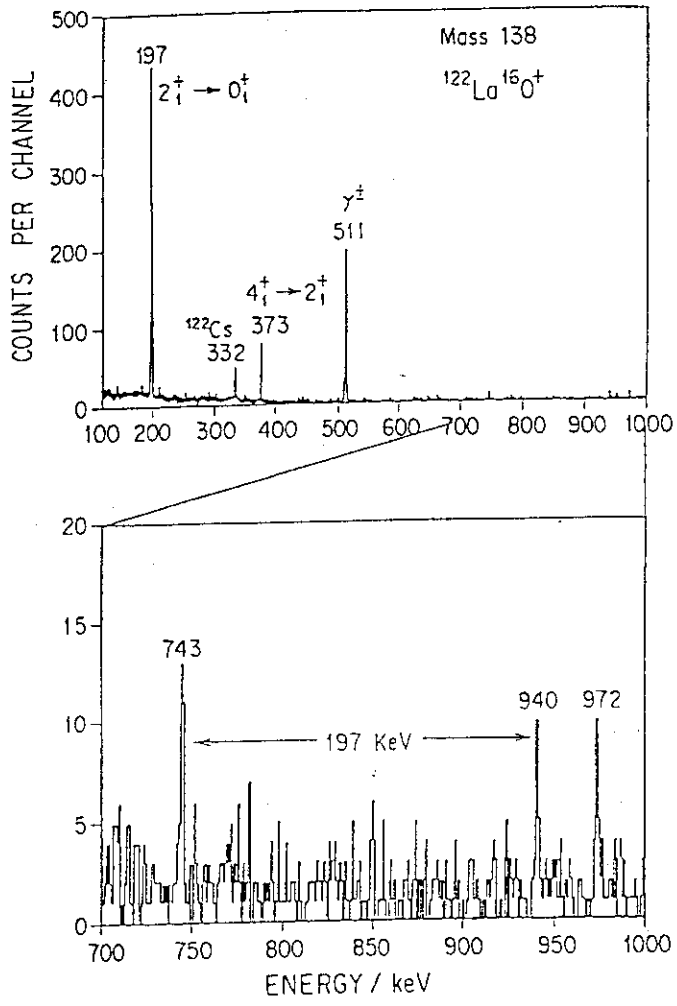

Fig.1 A γ-ray spectrum coincident with β-rays for mass 138 ($^{122}La^{16}O$).

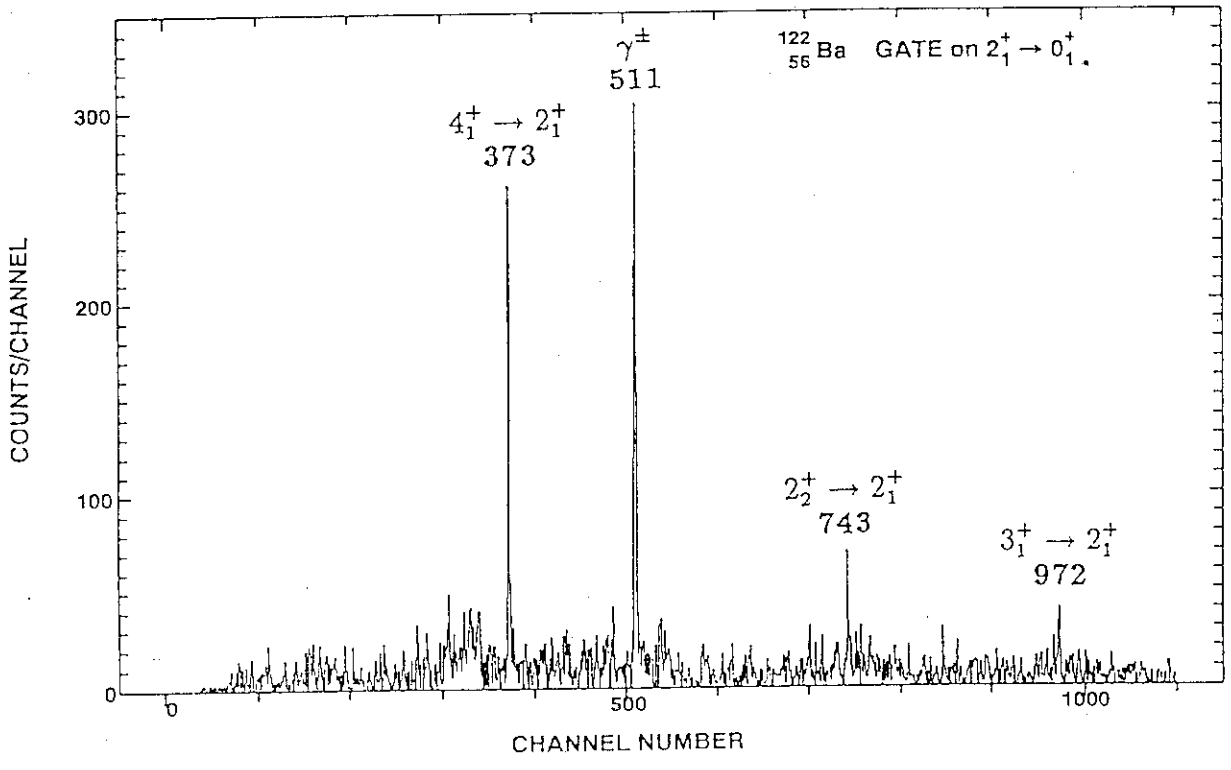

Fig.2 A γ-ray spectrum gated by the 197-keV ($2_1^+ \rightarrow 0_1^+$) γ-ray for mass 138 ($^{122}La^{16}O$).

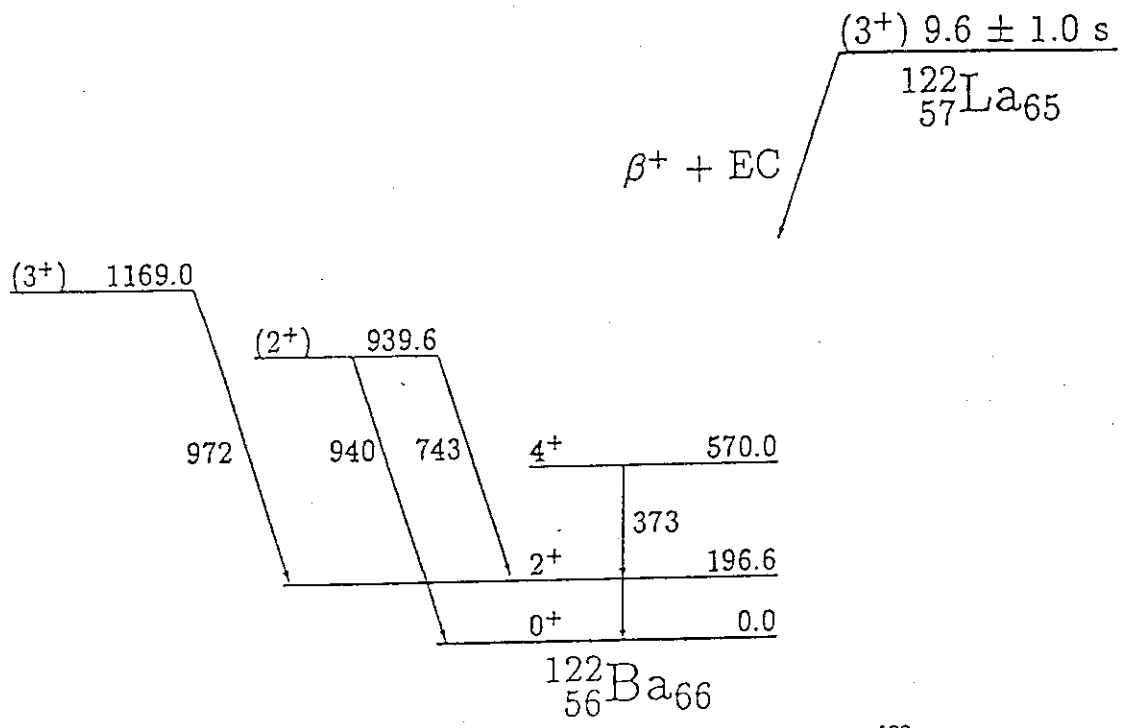

Fig.3 A proposed decay scheme for ^{122}La.

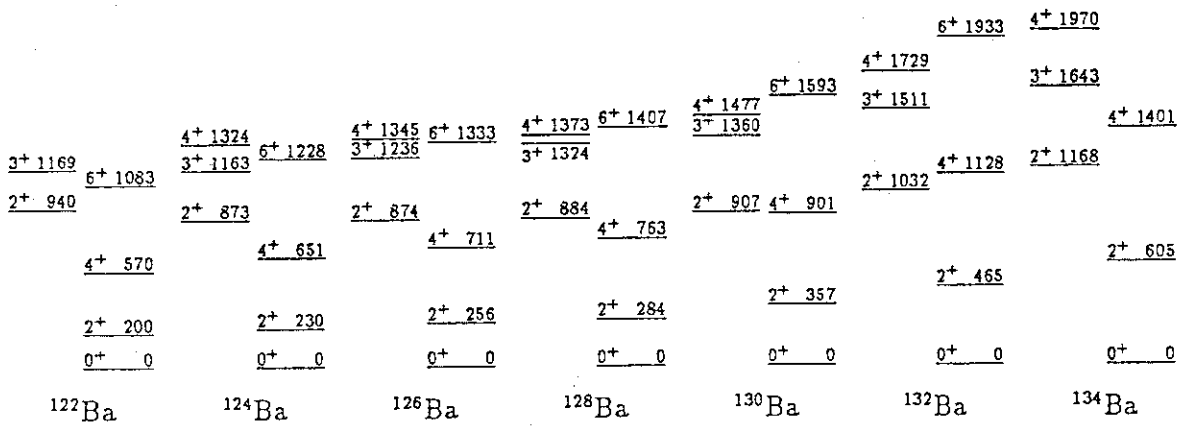

Fig.4 Systematics of lowlying levels in light Ba isotopes.

References

1) T. Sekine, H. Iimura, S. Ichikawa, M. Oshima, K. Hata, Y. Nagame, N. Takahashi and A. Yokoyama, JAERI-M 88-181, p.121 (1988).

2) S. Ichikawa, T. Sekine, H. Iimura, M. Oshima and N. Takahashi, Nucl. Instr. Meth. A274, (1988).

3) G. Puddu, G. Scholten and T. Otsuka, Nucl. Phys. A348, (1980).

4.3 A BETA-DECAY STUDIES OF ^{123}La WITH AN ON-LINE ISOTOPE SEPARATOR

Hideki IIMURA, Michihiro SHIBATA*, Shin-ichi ICHIKAWA, Toshiaki SEKINE**, Masumi OSHIMA*, Nobuo SHINOHARA, Masahide MIYACHI***, Akihiko OSA***, Hiroshi YAMAMOTO*** and Kiyoshi KAWADE***

Department of Chemistry, *Department of Physics, **Department of Radioisotopes, JAERI and ***Department of Nuclear Engineering, Nagoya University

Investigation of the nuclear structure of neutron deficient nuclei in the A=120-130 mass region has revealed that the nuclei tend to be very soft for γ-deformation and their collective character grows rapidly with decreasing neutron number. For the ^{123}Ba nucleus in-beam γ-ray spectroscopic studies has led to information on high-spin level structures.[1,2] However, experimental information on low-spin levels of this nucleus is very scarce; the knowledge of the excitation energies of such levels are needed for understanding the collective behaviour of this nucleus. In the present work, we studied the level scheme of ^{123}Ba from the β-decay of ^{123}La ($T_{1/2}$ = 16 sec) using a heavy-ion reaction and an on-line mass-separation technique.

The experiments were performed at the tandem accelerator facility, using the reaction ^{92}Mo(^{35}Cl,2p2n)^{123}La with a 180-MeV ^{35}Cl beam. The thickness of the molybdenum targets was about 3 mg/cm^2. Reaction products were ionized in a surface-ionization ion source, and mass-separated electromagnetically. In order to obtain ^{123}La activity free from the Cs and Ba isobars, the monoxide ions ^{123}La^{16}O$^+$ were separated by setting the magnetic field at the mass number of 139.[3] The mass separated ^{123}La activity was implanted into an aluminum-coated Mylar tape in a tape transport system and periodically transported to a measuring position, where γ-ray singles and γ-γ coincidence measurements were performed with a low-energy photon HPGe detector, a 20% HPGe detector and a 28% n-type HPGe detector. The decays of γ-rays were traced by taking consecutively 16 spectra counted for 3 sec each in order to distinguish the γ-ray peaks of ^{123}La from those of daughter nuclides. Coincident events were recorded in list mode on a magnetic tape.

Figure 1 shows levels and transitions in ^{123}Ba obtained from the

present measurements. The excited states were placed on the basis of the energies and coincidence relations of the γ-rays assigned to the decay of ^{123}La. We have derived 12 new levels, the energies of which are indicated with an asterisk. For some transitions between these levels internal conversion coefficients were obtained from a simultaneous measurement of electrons and γ-rays with Si(Li) and HPGe detectors. From the derived K conversion coefficients, the multipolarities of the 120.9-, 153.6-, 174.4- and 243.9-keV transitions have been determined to be M1 and/or E2. In order to obtain more information on the 120.9-keV transition we performed a β-γ delayed coincidence measurement, utilizing a plastic scintillator and the low-energy photon HPGe detector. This measurement has yielded $t_{1/2}$=0.83±0.06 μs as the half-life of the 120.9-keV level. If the 120.9-keV transition is M1, this half-life corresponds to a hindrance factor F_W=1.1 x 10^5. From assumed M1 multipolarity, I^π(120.9 keV) is restricted to $7/2^+$, $5/2^+$ and $3/2^+$, and hence K^π(120.9 keV) is also restricted to $7/2^+$, $5/2^+$, $3/2^+$ and $1/2^+$. These possible values of K^π(120.9 keV) give $\Delta K \leq 2$ for the 120.9-keV transiton, because the ground state is the band head of a $K^\pi=5/2^+$ band.[2] However, the hindrance factor is an extremely high value for M1 transitions with $\Delta K \leq 2$.[4]. Thus the 120.9-keV transition can be assigned to be pure E2. The half-life gives E2 hindrance factor F_W=2.8 to this transition.

The new levels at 120.9, 153.6, 328.0, 397.5, 695.3 and 790.8 keV are expected to be the $1/2^+$, $3/2^+$, $5/2^+$, $7/2^+$, $9/2^+$ and $11/2^+$ members of a new band with $K^\pi = 1/2^+$, respectively, because the energy spacings of the six members of this band are fairly consistent with the rotational formula:

$$E_I = E_0 + A\{I(I+1)+a(-1)^{I+1/2}(I+1/2)\},$$

and give a rotational parameter A=21.9 keV and a decoupling parameter a= -0.548. The Nilsson orbital [411]$1/2^+$ can be assigned to the 120.9-keV level because other Nilsson orbitals with $K^\pi=1/2^+$ are far from the Fermi surface for the 67th neutron at a deformation $\varepsilon = 0.27$ deduced from the reported quadrupole moment Q=1.52±0.13 b (ref.5) of the ground state. The negative decoupling parameter supports this Nilsson-orbital assignment.

References

1) N. Yoshikawa, J. Gizon and A. Gizon: J. de Phys. 40 (1979)209.
2) R. Wyss, F. Liden, J. Nyberg, A. Johnson, D. J. G. Love,A. H. Nelson, D. W.Banes, J. Simpson, A. Kirwan and R. Bengtsson: Z. Phys. A330 (1988) 123.
3) S. Ichikawa, T. Sekine, H. Iimura, M. Oshima and N. Takahashi: Nucl. Instr. and Meth. A274 (1989) 259.
4) W.Andrejtscheff, K.D.Schilling and P.Manfrass: Atomic Data and Nuclear Data Tables 16 (1975)515.
5) A.C.Mueller, F.Buchinger, W.Klempt, E.W.Otten, R.Neugart, C.Ekstrom, J.Heinemeier and The ISOLD Collaboration: Nucl. Phys. A403(1983)234.

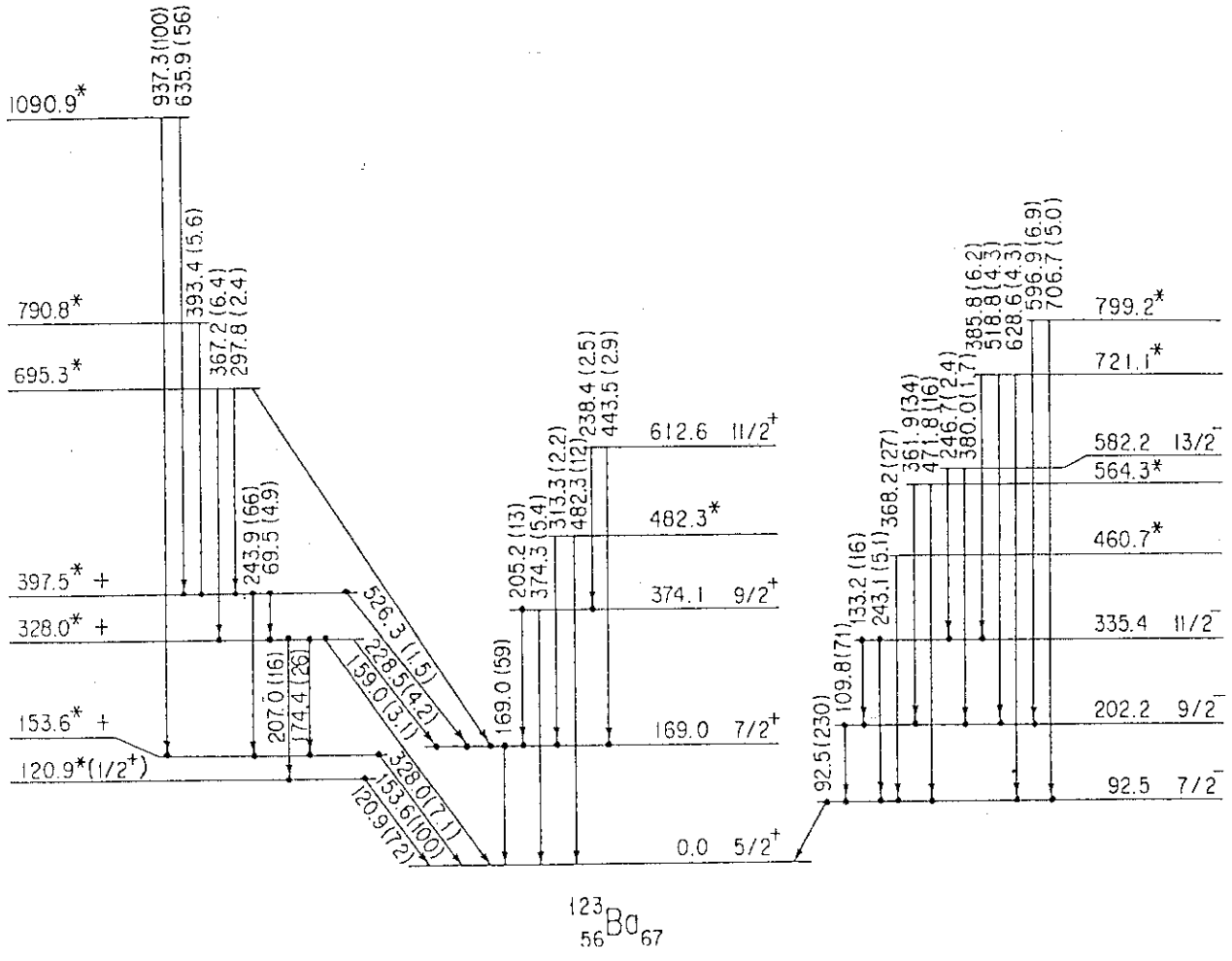

Fig. 1. Partial level scheme of ^{123}Ba populated by the β-decay of ^{123}La. The energies of the new levels are shown with an asterisk. The γ-intensities are given in parentheses relative to that of the 937.3-keV transition.

4.4 Lifetime measurement of the 2_1^+ state in ^{122,124,126}Ba

Tsuneyasu MORIKAWA[*1,*5], Toshiaki SEKINE[*1], Yuichi HATSUKAWA[*1], Masumi OSHIMA[*2], Shin-ichi ICHIKAWA[*3], Akihiko OSA[*3,*4], Akihiro TANIGUCHI[*4]

[*1]Department of Radioisotopes, [*2]Department of Physics, [*3]Department of Chemistry, Japan Atomic Energy Research Institute, [*4]School of Engineering, Nagoya University and [*5]Faculty of Science, Hiroshima University

The measurement of absolute transition rates provides a good means for testing various nuclear models. Especially in even-even nuclei, $B(E2;0_1^+ \rightarrow 2_1^+)$ values are one of the most important information for nuclear structure study. Our aim is a systematic lifetime measurement of the 2_1^+ state in neutron defficient nuclei in the Xe-Ba-Ce transitional region.

Recently, the BaF_2 scintillator of fast timing characteristics for γ-ray detection has been developped. The β-γ delayed coincidence technique using the scintillator in combination with a β-ray detector has become a powerful method for lifetime measurement. We employed this technique to derive lifetimes of ^{122,124,126}Ba. To produce ^{122,124,126}La, the parent nuclei of Ba, enriched ^{92}Mo and ^{nat}Mo targets were bombarded with ^{35}Cl beams from the JAERI tandem accelerator. The reaction products were mass separated in the form of LaO^+ with an isotope separator on-line (ISOL) connected to the accelerator. A Pilot-U $2''\phi\times3$ mm plastic detector and a $1''\phi\times1/2''$ BaF_2 detector were used to detect β and γ rays, respectively. A typical timing resolution of the system for prompt transitions was 150 ps FWHM at 1332 keV of a ^{60}Co source. Data of each event, γ-ray energy, β-ray energy and time difference between them, were recorded on magnetic tapes in list-mode. The time spectra corresponding to the $2_1^+ \rightarrow 0_1^+$ transition were analyzed with a deconvolution method to minimize χ^2 of the fit. Half-lives of 297(13), 297(26) and 141(8) ps were obtained for the 2_1^+ state in ^{122,124,126}Ba, respectively. The half-lives were converted into $B(E2;0_1^+ \rightarrow 2_1^+)$ values. The results are listed in table 1.

In Xe isotopes, experimental $B(E2;0_1^+ \rightarrow 2_1^+)$ values have been reported as shown in fig. 1 (a). Although the data are somewhat scattered, one can see some trend with respect to the neutron number. Otsuka et al. performed an IBM-2 calculation taking into account the Pauli blocking effect for the Xe-Ba-Ce isotopes.[1] The results for the Xe isotopes are also plotted in fig. 1 (a). The solid line denotes the calculation including the Pauli effect and the dashed line indicates the limit of no Pauli effect. The experimental values are well reproduced by the IBM-2 calculation including the Pauli blocking effect.

Table 1. Half-lives of the 2_1^+ state and B(E2;$0_1^+ \rightarrow 2_1^+$) values in ^{122,124,126}Ba.

	Present work		Previous work	
Nuclide	$T_{1/2}$ (ps)	B(E2) (e^2b^2)	$T_{1/2}$ (ps)	B(E2) (e^2b^2)
^{122}Ba	297(13)	2.71(12)	-	-
^{124}Ba	297(26)	1.37(12)	-	-
^{126}Ba	141(8)	1.71(10)	126(14)[a)]	1.90(21)[a)]

[a)]Ref. 3.

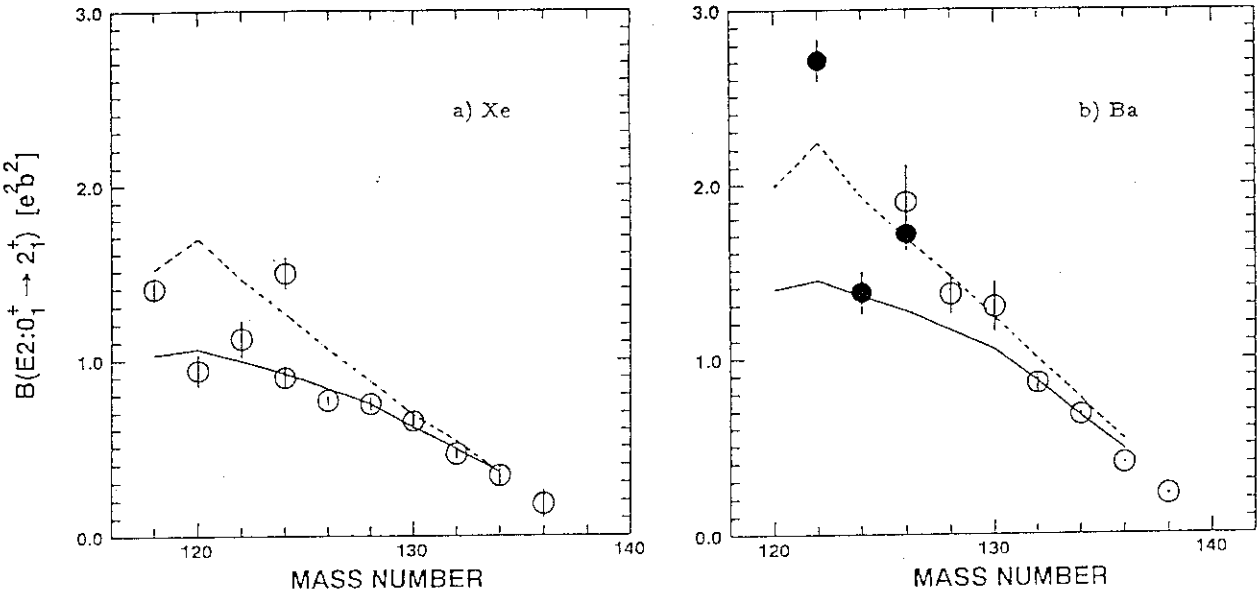

Fig.1. B(E2) values for neutron defficient isotopes of Xe (a) and Ba (b). Data obtained in the present work are plotted in solid circles. Open circles indicate previous experimental values taken from ref. 3. The solid line denotes the IBM-2 model calculation taking account of the Pauli blocking effect and the dashed line corresponds to the limit of no Pauli blocking effect.[1)]

New data from the present work for the Ba isotopes are plotted in comparsion with the results of the IBM-2 calculations in fig. 1 (b). In the data for Ba, in contrast, the B(E2) values show another trend opposite to that of the Xe isotopes, though the data are rather scattered. The IBM-2 calculation including the Pauli blocking effect does not seem to reproduce the experimental data. For ^{124}Ba, rather strong side feedings from two quasi-particle states to the 4_1^+ state might have affected the measured half-life of the 2_1^+ state. In the mean time, the B(E2) value for ^{122}Ba is rather large compared with the IBM-2 calculation of no Pauli limit and other predictions by systematics presented in ref. 2. To confirm the present data, another experiment on ^{122,124,126}Ba is beeing planned.

References

1) T.Otsuka, X.W.Pan, and A.Arima, private communication. (1989)
2) S.Raman, C.W.Nestor, Jr., S.Kahane, and K.H.Bhatt, At. Data. Nucl. Data Tables 42 (1989) 1.
3) S.Raman, C.H.Malarkey, W.T.Milner, C.W.Nestor, Jr., and P.H.Stelson, At. Data. Nucl. Data Tables 36 (1987) 1.

4.5 A RESEARCH FOR THE PRODUCTION OF TRANSURANIUM ELEMENTS

Ichiro FUJIWARA, Seiichi SHIBATA*, Hisaaki KUDO**, Kazuaki TSUKADA***, Tsutomu OHTSUKI***, Yuichi HATSUKAWA****, Nobuo SHINOHARA*****, Shin-ichi ICHIKAWA*****, Masaaki MAGARA*****,

School of Economics, Otemon Gakuin University, *Institute for Nuclear Study, University of Tokyo, **Department of Chemistry, Niigata University, ***Department of Chemistry, Tokyo Metropolitan University, ****Department of Radioisotopes, *****Department of Chemistry, JAERI

Synthesis of the transuranium nuclides by heavy ion reactions proceeds through the process of compound nucleus formation, but the fission barrier of the compound nucleus with atomic number greater than 100 is so low that almost all compound nuclei compete with the fission in the every step of successive neutron evaporations. Therefore, the transuranium nuclides must be synthesized to form the compound nucleus with the excitation energy as low as possible, whereas the projectile of the charged particles must overcome the coulomb barrier for the compound-nucleus formation. This report presents the results of the synthesis of mendelevium performed using the JAERI TANDEM accelerator.

Target of ^{241}Am (100 $\mu g/cm^2$ in thickness) was prepared by electrodeposition from organic solution of the americium nitrate. The americium target was located in a reaction chamber of He-jet rapid transportation system and bombarded by ^{12}C beams of energy 80 MeV (on the target) at intensity of 600 enA. Details of the experimental procedures were described in the previous report.[1)]

The result of the measurement of alpha-rays from ^{250}Md (half-life 52s) and ^{249}Md (24s) produced by the ^{241}Am(^{12}C,3n)^{250}Md and ^{241}Am(^{12}C,4n)^{249}Md reactions respectively is shown in Fig. 1. The EC-decay daughter ^{249}Fm (2.6min) of ^{249}Md was detected, but the daughter ^{250}Fm (30min) of ^{250}Md after EC decay has too long half-life to be detected in this experimental condition. The accumulation of the alpha-ray counting has been continued this year. However, it is not still enough to reveal the details of the decay schemes of ^{249}Md, ^{250}Md and

^{249}Fm and the cross sections of the formation reactions. We expect to accumulate more alpha-ray counting by preparing another thicker ^{241}Am target.

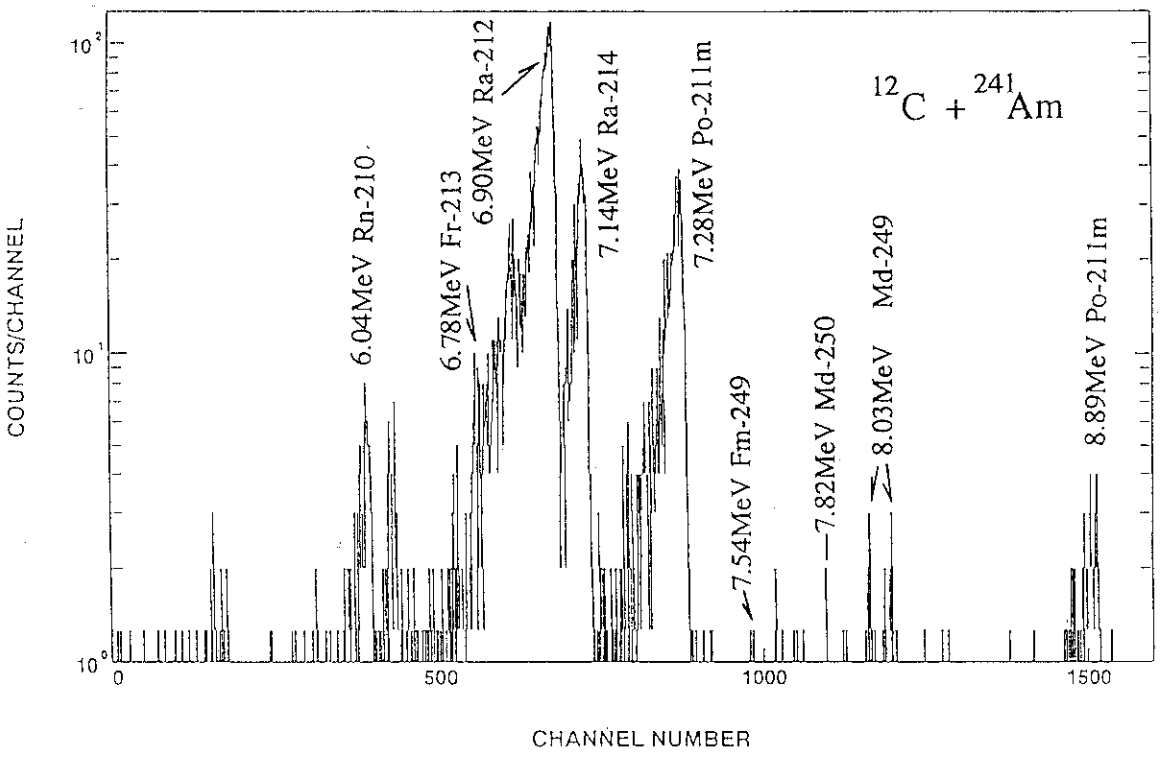

Fig. 1 Alpha-ray spectrum measured by means of a He-jet transportation and moving-tape system. The duration and the cycle for the collection of reaction products and the alpha-ray measurement were 25 s and 720 times, respectively.

Reference

1) I. Fujiwara, et al.: JAERI-M 90-139 (1990) 123.

4.6 SEPARATION AND IDENTIFICATION OF NEUTRON-RICH RUTHENIUM ISOTOPES FROM HEAVY-ION REACTIONS BY MEANS OF THE FAST ON-LINE SOLVENT EXTRACTION SYSTEM SISAK

Nobuo SHINOHARA, Shin-ichi ICHIKAWA, Masaaki MAGARA, Kazuaki TSUKADA*, Tsutomu OHTSUKI*

Department of Chemistry, JAERI, *Department of Chemistry, Tokyo Metropolitan University

Introduction

An on-line chemical separation system, which consists of a KCl/He gas-jet recoil-transport system[1] (abbreviated to HJRT) and a continuous multistage solvent extraction system SISAK (Short-lived Isotopes Studied by AKUFVE technique),[2] has been applied for the identification and investigation of short-lived isotopes of neutron-rich ruthenium in the spontaneous fission of ^{252}Cf and the proton-, ^{12}C- and ^{19}F-induced fissions of ^{232}Th, $^{233,235,238}U$, ^{237}Np and ^{244}Pu targets. In this report, the decay data for γ-rays following the β^- decay of short-lived $^{107-112}Ru$ are presented.

Experimental

Figure 1 shows the schematic drawing of the SISAK experiment for the fast separation of ruthenium. The fission products collected with the aerosol particles in the helium gas were transferred to a static mixer, where the carrier gas and a sulfuric acid solution containing the ruthenium carrier (5×10^{-5}M $RuCl_3$/0.2M H_2SO_4) were mixed thoroughly. The helium gas was then separated by centrifuge (degasser, Dg in Fig. 1). Then, a solution of 0.015M $Ce(SO_4)_2$/0.2M H_2SO_4 preheated to about 90 °C was supplied into the dissolved solution in order to oxidize the ruthenium to RuO_4. The liquid was then contacted with organic solvent of CCl_4 in another static mixer and the mixture was fed into another centrifuge (C1 in Fig. 1) to separate the organic and aqueous solutions, where the ruthenium oxide is isolated from other fission products by extraction into CCl_4. Gamma-ray measurements were carried out on the organic solution after C1 using a coaxial HPGe detector.

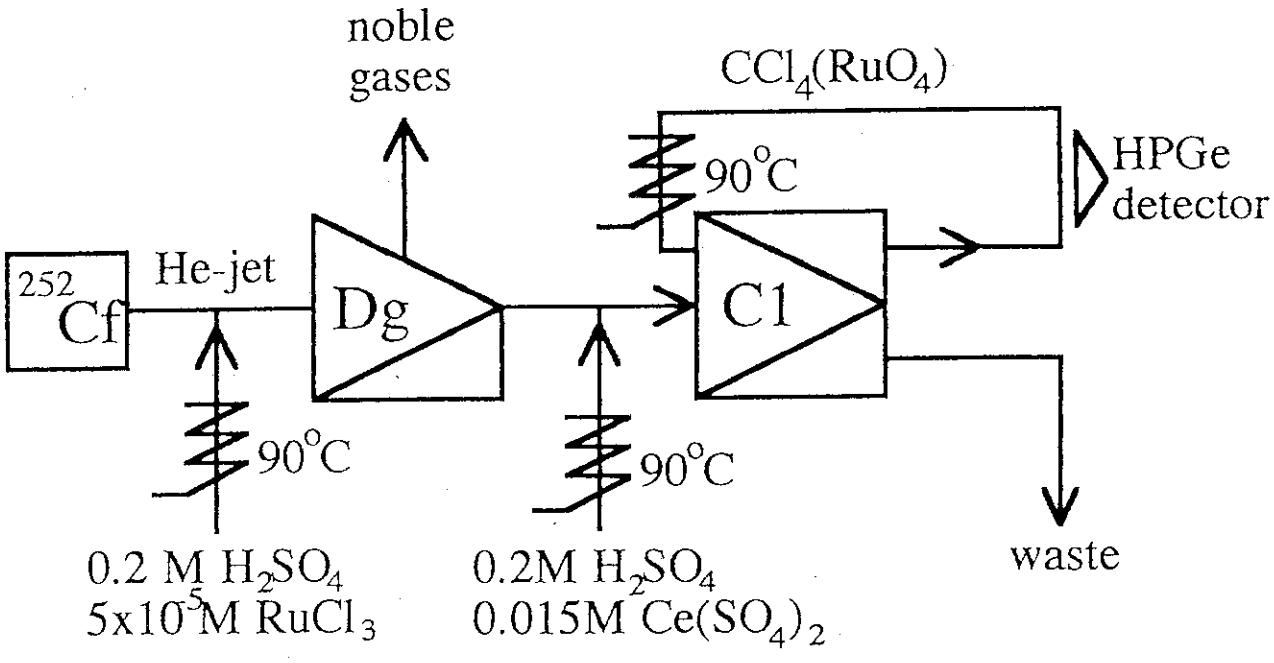

Fig. 1 Flow sheet of the SISAK chemical separation system for the fast separation of ruthenium.

Results and discussion

Table 1 gives the decay data on the ruthenium isotopes. The ^{107}Ru isotope has a half-life of 3.75 min, which is most reliable from evaluating the values from Refs.[3,4,5] When normalized to 100 % for the 194.4-keV γ-ray, the relative intensity for the 462.9 keV γ-ray is 36.4±9.1 %, which almost agrees with 35±11 % by Kaffrell et al.[6] rather than 42 % by Franz et al.[3] The absolute intensities, Iγ in Table 1, were obtained by taking into account the γ-ray yields of ^{252}Cf fission given by Wilhelmy[7] and the cumulative yields for the ruthenium isotopes by Rider.[8]

The half-life of ^{108}Ru, 4.55 min, is too long for the rapid separation as well as ^{107}Ru. Therefore, only a γ-ray of 165.02 keV was detected in this work. Another reliable γ-ray from ^{108}Ru is 150.46 keV one with the relative intensity of 28±1 % when the intensity of the 165 keV γ-ray is normalized to 100 %.[9]

The half-life of ^{109}Ru is 34.5±0.1 s. In our work, 13 γ-rays from ^{109}Ru were observed and their energies and relative intensities have been determined, where the relative intensities of the 194 keV and 250 keV γ-ray were corrected for the contribution of other Ru and Rh isotopes.

Table 1. Energies and intensities of gamma-rays following the β^- decay of $^{107-112}Ru$.[a]

Isotope	$T_{1/2}$[b] (s)	E_γ (keV)	Relative yield /fission (cps)	Relative intensity (%) this work	Relative intensity (%) Ref.[3]	I_γ[c] (%)
^{107}Ru	225(3)	194.40(28)	2.65(29)	100(11)	100	10.3(8)
		462.93(8)	0.96(22)	36.4(91)	42	
^{108}Ru	273(3)	165.02(7)	6.28(29)			27.8(28)
^{109}Ru	34.5(1)	116.39(13)	6.11(96)	29.4(47)	34.1(32)	
		184.03(29)	1.16(58)	5.6(28)	6.6(4)	
		194.40(9)	2.29(37)	11.0(18)	5.1(6)	
		206.38(2)	20.77(71)	100.0(34)	100	
		220.16(16)	1.92(32)	9.3(16)	10.4(15)	
		226.05(3)	15.84(87)	76.3(49)	78.1(6)	
		245.06(9)	1.87(39)	9.0(19)	7.6(7)	
		249.65(17)[d]	<1.06(9)	<5.1(15)	3.5(10)	
		358.78(3)	12.07(48)	58.1(30)	59.8(35)	16.4(24)
		366.39(14)	1.01(24)	4.9(12)	7.0(12)	
		426.56(9)	8.14(67)	39.2(35)	45.6(45)	
		465.34(22)	2.12(45)	10.2(22)	11.6(15)	
		819.21(18)	2.93(44)	14.1(22)	20.0(16)	
^{110}Ru	12.0(1)	96.04(20)	1.30(34)	6.1(17)	6	
		112.51(6)	21.2(13)	100.0(61)	100	15.8(44)
		373.68(4)	2.55(36)	12.0(17)		
^{111}Ru	2.12(7)	211.61(6)	5.96(84)	54.0(82)		
		249.65(17)	<1.06(30)	<9.6(28)		
		303.63(6)	8.28(66)	75.0(73)		20.7(41)
		381.40(4)	11.04(61)	100.0(55)		
^{112}Ru	1.75(7)	326.82(5)	7.2(4)			

[a] Uncertainties of the values are given in parentheses.

[b] Reliable half-lives taken from Ref.[3] for ^{107}Ru and ^{108}Ru, Ref.[12], for ^{109}Ru and ^{110}Ru, and Ref.[10] for ^{111}Ru and ^{112}Ru.

[c] Absolute intensities of the g-rays calculated with percent yields of the γ-rays per fission of ^{252}Cf from Ref.[7] and cumulative yields of the ruthenium isotopes from Ref.[8].

[d] Overlapped with the same energy γ-ray from ^{111}Ru.

Very few decay data of Ru exist in the mass region ≥110 and the Refs.[3,4,7,10,11,12] are only available to evaluate the decay characteristics of the short-lived Ru isotopes. The half-life of ^{110}Ru is 12.0 s which has been determined by Skålberg.[12] In this work, the detailed relative intensities of ^{110}Ru were determined. The observed γ-rays with energies of 211, 250, 304 and 381 keV are assigned to the β^- decay of ^{111}Ru according to Ref.[10] and the half-life of 2.12 s is most

reliable by evaluating the previous values.[3,4,11] The relative intensities for ^{111}Ru are first determined in this work. The 326.82 keV γ-ray is assigned to ^{112}Ru and ^{109}Rh. The 263.5 keV γ-ray from ^{113}Ru[10] was not detected in our experiments, since the half-life of 0.8 s for ^{113}Ru is short to our SISAK separation.

References

1) K. Tsukada, T. Ohtsuki, K. Sueki, Y. Hatsukawa, H. Yoshikawa, K. Endo, H. Nakahara, N. Shinohara, S. Ichikawa, S. Usuda and M. Hoshi, Radiochim. Acta 51 (1990) 77.

2) G. Skarnemark, M. Skålberg, J. Alstad and T. Bjørnstad, Phys. Scr. 34 (1986) 597.

3) G. Franz and G. Herrmann, J. Inorg. Nucl. Chem., 40 (1978) 945.

4) P. Fettweis and P. del Marmol, Z. Physik A275 (1975) 359.

5) W. R. Pierson, H. C. Griffin and C. D. Coryell, Phys. Rev. 127 (1962) 1708.

6) N. Kaffrell, P. Hill, J. Rogowski, H. Tetzlaff, N. Trautmann, E. Jacobs, P. De Gelder, D. De Frenne, K. Heyde, G. Skarnemark, J. Alstad, N. Blasi, M. N. Harakeh, W. A. Sterrenburg and K. Wolfsberg, Nucl. Phys. A460 (1986) 437.

7) J. B. Wilhelmy, UCRL-18978 (1969).

8) B. F. Rider, NEDO-12154-3(C) (1981).

9) R. L. Haese, F. E. Bertrand, B. Harmatz and M. J. Martin, Nucl. Data Sheets 37 (1982) 289.

10) H. Penttilä, P.Taskinen, P. Jauho, V.Koponen, C. N. David and J. Äystö, Phys. Rev. C38 (1988) 931.

11) M. Yun, N. Trautmann and G. Skarnemark, Chin. J. Nucl. Sci. Eng. 5 (1985) 324.

12) M. Skålberg, Ph. D. Thesis, Chalmers University of Technology, Göteborg (1991).

4.7 BINARY SCISSION CONFIGURATION IN THE FISSION OF ^{233}Pa

Tsutomu OHTSUKI, Yuichiro NAGAME, Hiroshi IKEZOE*,
Ikuo KANNO**,Masaaki MAGARA***
Kazuaki TSUKADA****, Ichiro NISHINAKA****,
Toshiaki SEKINE, Hiromichi NAKAHARA****

Department of Radioisotopes, *Department of Physics,
**Department of Reactor Engneering,
***Department of Chemistry, JAERI,
****Department of Chemistry, Tokyo Metropolitan University

Recent data for mass and total kinetic energy distributions in the low energy fission of the heavy nuclides such as ^{258}Fm, ^{258}No, ^{259}Md, ^{260}Md and ^{262}No reveal the existence of two types of scission configurations for the same symmetric mass division[1,2].

Understanding of the phenomena has been attempted by theoretical calculations of the potential energy surface of extremely deformed nuclei which show two paths leading to scission[3,4] in the fission of those heavy nuclides. The existence of two fission valleys in the potential energy surface has also been predicted even for lighter actinide nuclei and for pre-actinides by some theorists[5,6,7] although proper dynamical consideration still remains to be given.

The aim of the present work is to study, by a time-of-flight method, velocities and kinetic energies of fragments produced in the proton-induced fission of actinide, and to investigate if there are two components in the time and kinetic energy distributions of fragments with the mass region of A=126-132 where both symmetric and asymmetric modes are expected.

The correlation between fragment mass and total kinetic energy has been measured for the proton-induced fission of ^{232}Th by means of a double-arm TOF spectrometer constructed at the JAERI tandem accelerator facility. The start detector was composed of a carbon foil (30 μg/cm^2 thick) and a micro-channel plate, and the stop signal was delivered by a large-area parallel-plate avalanche counter (PPAC). The flight paths were 82.0 cm and 60.7 cm and the laboratory angles of detectors were at 45° and −133.5 ° with respect to the beam direction. The target of ^{232}Th evaporated onto a 10 μg/cm^2 carbon foil was bombarded with a 13 MeV proton beam. The calibration of fragment velocity was carried out using a ^{252}Cf source.[8,9]

The primary mass (before neutron emission) of a fission fragment was obtained from the ratio of the velocities of the pair fragments with assumptions that no neutron was emitted from the compound nucleus prior to fission and that neutrons from the primary fragment were isotropically emitted and did not alter the initial fragment velocity. The primary mass yield curve for ^{232}Th+p fission is shown in fig.1. The characteristic feature of mass distribution is typically asymmetric fission and the region for symmetric fission is broad as expected. The time distributions and the total kinetic energy distributions(TKE) of each of fragment masses are shown in fig.2. The binary structure is clearly seen for the fragment mass 128–130.

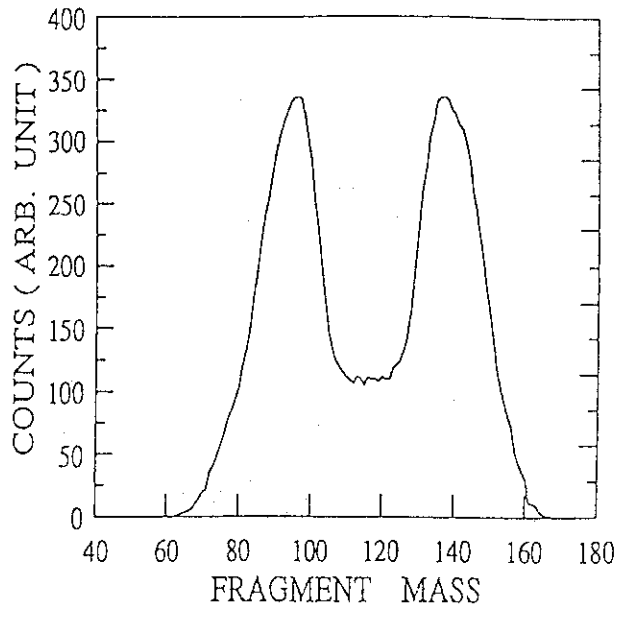

Fig.1 Fission fragment mass distribution of ^{232}Th+p for 13.0 MeV protons.

The slower component and the faster one are equivalent to the lower total kinetic energy component and higher one. The results of two-Gaussian fitting are also shown in the same figure. From the analysis, the kinetic energy for lower components is almost in agreement with the Viola's systematics[10] and the higher one reaches to 187 MeV, and the average difference between the lower component and higher one was almost 16 MeV over the region A=127-132. In the spontaneous fission of the heavier actinide region, the existence of two TKE components has been reported by Hulet et al. and interpreted as a liquid-drop-like deformed and a shell-influenced compact shape at scission point is leading to the lower TKE component and the higher one, respectivelly. The present result indicates that similar scission point configurations exist in the fission of light actinide region.

Reference

1) E.K. Hulet, J.F. Wild, R.J. Dougan, R.W. Lougheed, J.H. Landrum, A.D. Dougan, M. Schädel, R.L. Hahn, P.A. Baisden, C.M. Henderson, R.J. Dupzyk, K. Sümmerer, and G.R. Bethune, Phys. Rev. Lett. 56 313(1986).

2) E.K. Hulet, "*Bimodal Fission*" in *Proceedings of the 50 Years with Nuclear Fission, 1989, Washington, D.C. and Gaithersburg, Maryland,* editted by J.W. Behrens and A.D. Carlson(Published by American Nuclear Society, Inc.,

La Grande Park, Illinois 60525 USA), Vol.2, p.533(1989).
3) P. Möller, J.R. Nix, and W.J. Swiatecki, Nucl. Phys. A469,1(1987).
4) S. Ćwiok, P.Rozmej, A. Sobiczewski and Z. Patyk, Nucl. Phys. A491, 281(1989).
5) V.V. Pashkevich, Nucl. Phys. A169, 275(1971).
6) J.F. Berger, M. Girod and D. Gogny, Nucl. Phys. A428, 23c(1984).
7) U. Brosa, S. Grossmann, and A. Müller. Z. Phys., A325, 241(1986).
8) H. Henschel, A. Kohnel, H. Hipp, and G. Gönnenwein, Nucl. Inst. Meth. 190 125(1981).
9) H.W. Schmitt, W.E. Kiker and C.W. Williams, Phys. Rev. B137, 837(1965).
10) V.E. Viola, K. Kwiatkowski, and M. Walker, Phys. Rev. C 31, 1550(1985).

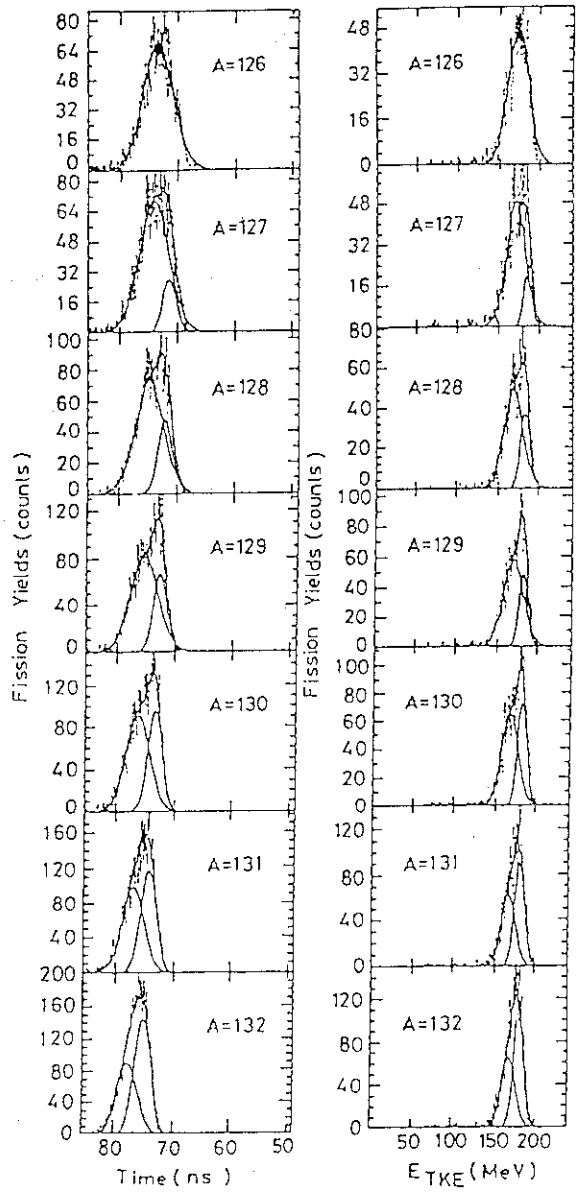

Fig.2 Time distributions for the 82.0 cm flight path and the total kinetic energy distributions in the fragment mass region A=126 ~ 132. Solid curves indicate the result of a Gaussian fit to the time and energy distributions.

4.8 EXTREMELY ASYMMETRIC MASS DIVISION IN LOW-ENERGY PROTON-INDUCED FISSION OF ^{244}Pu

Kazuaki TSUKADA, Nobuo SHINOHARA*, Tsutomu OHTSUKI, Keisuke SUEKI, Shin-ichi ICHIKAWA*, Takayuki KOBAYASHI, Ichiro NISHINAKA, Michio HOSHI*, and Hiromichi NAKAHARA

Faculty of Science, Tokyo Metropolitan University,
*Department of Chemistry, JAERI.

Introduction

The knowledge of mass distributions is indispensable to the study of fission mechanism. Asymmetric mass distributions were observed in the low-energy fission of actinides ($90<Z<100$)[1,2] and their features have been discussed regarding the peak and valley region of the mass yield curves. However, few studies for the rare earth region (especially, $A>150$) have been reported because of the lack of actinide targets and shortness of half-lives of fission products. In particular, mass yield dependence on the incident energy has been scarcely reported[3]. In order to measure accurate mass yields in this rare earth region, rapid chemical separation of the reaction products is essential, considering short half-lives of the nuclides to be measured.

A computer-controlled rapid ion-exchange separation system has been developed[4] and applied to the study of the mass distributions of short-lived nuclides as a function of the incident energy of proton beams. The present paper reports excitation functions of rare earth nuclides in the 10-16 MeV proton-induced fission of ^{244}Pu.

Experiments

A ^{252}Cf source was used for testing the ion-exchange method[5], and then fission products to be measured for the determination of mass yields were decided. Table 1 shows the nuclides used for determination.

An electrodeposited ^{244}Pu target was bombarded for 10-20 min or 1 h in order to ensure adequate production of fission product. The incident proton energy was changed from 10 to 16 MeV at the beam current of about 1.5 eμA. The fission products were caught with an aluminium catcher foil of 5.4 mg/cm^2 thickness. The yields of main fission products were determined

by directly γ-ray measurements. Rare earth elements were separated by a computer-controlled rapid ion-exchange separation system. Dissolution of the catcher foil and chemical separation were completed within 20 min.

Results and Discussion

The fission yields were measured for 42 products in the p+^{244}Pu system. The incident energy dependence in the range of 10 to 16 MeV is shown in Fig.1. The mass ratios (A_H/A_L) of the complementary fragment pairs are given in the figure, where the subscripts H and L denote the heavy and light products. Mass yields of the extremely asymmetric division up to A_H/A_L=2.03 were measured in this work. The incident energy dependece of the yields in the symmetric region was stronger than those in the outer side of the asymmetric peak as shown in Fig.1. The ratios of cross sections between the symmetric and asymmetric products are given in Fig.2, to show the energy dependence more clearly. As the denominator, the average of ^{141}Ce and ^{143}Ce cross sections was chosen. In the region of A_H/A_L<1.15, the ratios are less energy dependent, whereas the ratios in A_H/A_L>1.15 are strongly energy dependent.

Such a distinctively different energy dependence between the symmetric and the asymmetric divisions suggests the existence of two fission barriers leading to a hypothesis of "two independent modes" by Turkevich et al.[6]. In 1971, Pashkevich[7] suggested theoretically that there could be two kinds of saddle configurations in the fission of ^{236}U. Konecny et al.[8] have reported that in the fission of actinium the symmetric fission barrier heights are higher than the asymmetric ones and that the asymmetric and symmetric fissions proceed over their different saddle points. Experimentally, two types of the mass distributions in the actinide region have also been observed[9,10], where the energy dependence has been discussed near the peak top but no excitation function in the extremely asymmetric mass division has been reported. We have measured the excitation function for A=162 (A_H/A_L=2.03). The extremely asymmetric region has obviously a different energy dependence from the symmetric region, but it has rather a similar dependence to the asymmetric peak top. Thus, it may be concluded that the fission of the extremely asymmetric region (A_H/A_L=2.03) is dominated by the same mode as the fission near the peak top.

References

1) M.Goeppert-Mayer, Phys.Rev. 74 (1948) 235.
2) H.Nakahara and T.Ohtsuki, J.Radioanal.Nucl.Chem.,Article 142 (1990) 231.
3) V.K.Rao, V.K.Bhargava, S.G.Marathe, S.M.Sahakundu and R.H.Iyer, Phys. Rev. C19 (1979) 1372.
4) K.Tsukada, T.Ohtsuki, K.Sueki, Y.Hatsukawa, H.Yoshikawa, K.Endo, H.Nakahara, N.Shinohara, S.Ichikawa, S.Usuda and M.Hoshi, Radiochim. Acta 51 (1990) 77.
5) K.Tsukada, K.Sueki, T.Ohtsuki, T.Kobayashi, I.Nishinaka, H.Nakahara, N.Shinohara, S.Ichikawa, M.Hoshi, and Y.Nagame, JAERI-M 90-139(1990)123.
6) A.Turkevich and J.B.Niday, Phys. Rev. 84 (1951) 52.
7) V.Pashkevich, Nucl.Phys. A169, (1971) 275.
8) E.Konecny, H.J.Specht, and J.Weber, Proceedings of IAEA Symposium on Physics and Chemistry of Fission 1973, IAEA SM-174/20, Vol.II, p.3.
9) D.G.Perry and A.W.Frairhall, Phys. Rev. C4 (1971) 977.
10) T.Ohtsuki, Y.Hamajima, K.Sueki, H.Nakahara, Y.Nagame, N.Shinohara and H.Ikezoe, Phys. Rev. C40 (1989) 2144.

Table 1 Fission product γ-decay data used in mass yield measurements.

Nuclide	Half-life	γ-ray		Nuclide	Half-life	γ-ray	
		Energy (keV)	Intensity (%)			Energy (keV)	Intensity (%)
^{85m}Kr	4.48 h	151.2	75.1±1.8	^{140}Ba	12.75 d	537.3	24.4±0.2
^{87}Kr	76.3 m	402.6	49.6±3.1	^{140}La	40.28 h	1596.5	95.40±0.08
^{88}Kr	2.84 h	196.3	26.0±1.2	^{141}Ce	32.50 d	145.4	48.4±0.4
^{91}Sr	9.52 h	555.6	56.1±3.9	^{142}La	1.52 h	641.2	47.4±0.5
		1024.5	33.4±2.3	^{143}La	14.2 m	620.5	2.34±0.12
^{92}Sr	2.71 h	1383.9	90.±10	^{143}Ce	33.0 h	293.3	42.8±0.4
^{93}Y	10.1 h	266.9	6.98±1.24	^{146}Ce	13.52 m	316.7	56.2±3.0
^{95}Zr	64.03 d	756.7	54.5±0.2	^{146}Pr	24.1 m	453.9	48.0
^{97}Zr	17.0 h	743.4	94.75±0.30			1524.7	15.6
^{97}Nb	72.1 m	657.9	98.39±0.20	^{147}Pr	13.6 m	314.6	24.0
^{99}Mo	2.75 d	140.5	4.57±.24	^{147}Nd	10.98 d	91.1	27.9
^{99m}Tc	6.01 h	140.5	89.06±0.24			531.0	13.1±0.7
^{103}Ru	39.25 d	497.1	90.9±2.7	^{149}Nd	1.73 h	114.3	19.0±1.6
^{105}Ru	4.44 h	469.4	17.5±0.5			211.3	25.9±1.4
^{105}Rh	35.36 h	318.9	19.1±0.6	^{149}Pm	2.21 d	285.9	3.1±0.2
^{111}Ag	7.45 d	342.1	6.68	^{150}Pm	2.68 h	333.9	68.±4
^{112}Ag	3.14 h	617.4	42.5	^{151}Nd	12.44 m	116.8	43.4±2.4
^{113g}Ag	5.37 h	298.6	9.0	^{151}Pm	28.40 h	340.1	22.±1
^{115g}Cd	2.23 d	336.2	45.9±0.9	^{152}Nd	11.4 m	278.5	29.±3
^{117g}Cd	2.49 h	273.3	27.9±0.7	^{153}Sm	46.7 h	103.0	28.3±0.6
		1303.3	18.2±0.6	^{155}Sm	22.1 m	104.3	74.6±3.8
^{117m}Cd	3.36 h	1997.3	26.2±0.2	^{156}Sm	9.4 h	203.8	20.2±3.7
^{127g}Sn	2.10 h	1114.3	38.±6	^{156}Eu	15.2 d	811.8	9.7±0.8
^{127}Sb	3.85 d	473.0	24.7±0.9	^{157}Sm	8.11 m	196.4	22.
		685.7	35.3±0.8			197.8	62.
^{128g}Sn	59.1 m	482.3	59.0±6.7	^{157}Eu	15.1 h	370.5	11.
^{128g}Sb	9.01 h	754.0	100.±5			410.7	18.
^{129}Sb	4.32 h	812.6	43.±1	^{158}Eu	45.9 m	944.2	25.
^{131}I	8.02 d	364.5	81.2	^{159}Eu	18.1 m	95.7	2.58±0.71
^{132}Te	3.26 d	228.2	88.±3	^{159}Gd	18.56 h	363.6	10.8±2.8
^{133g}I	20.8 h	529.9	87.0±2.3	^{162}Gd	9.0 m	441.6	52.±3
^{135}I	6.61 h	1260.4	28.9±0.2	^{162}Tb	7.76 m	260.0	80.0±3.76
^{135}Xe	9.08 h	249.8	90.2±0.2			807.5	42.8±2.4
^{139}Ba	1.38 h	165.8	22.0±1.0	^{163}Tb	19.5 m	389.7	24.3±2.9
				^{170}Tm	128.6 d	84.3	3.2±0.3

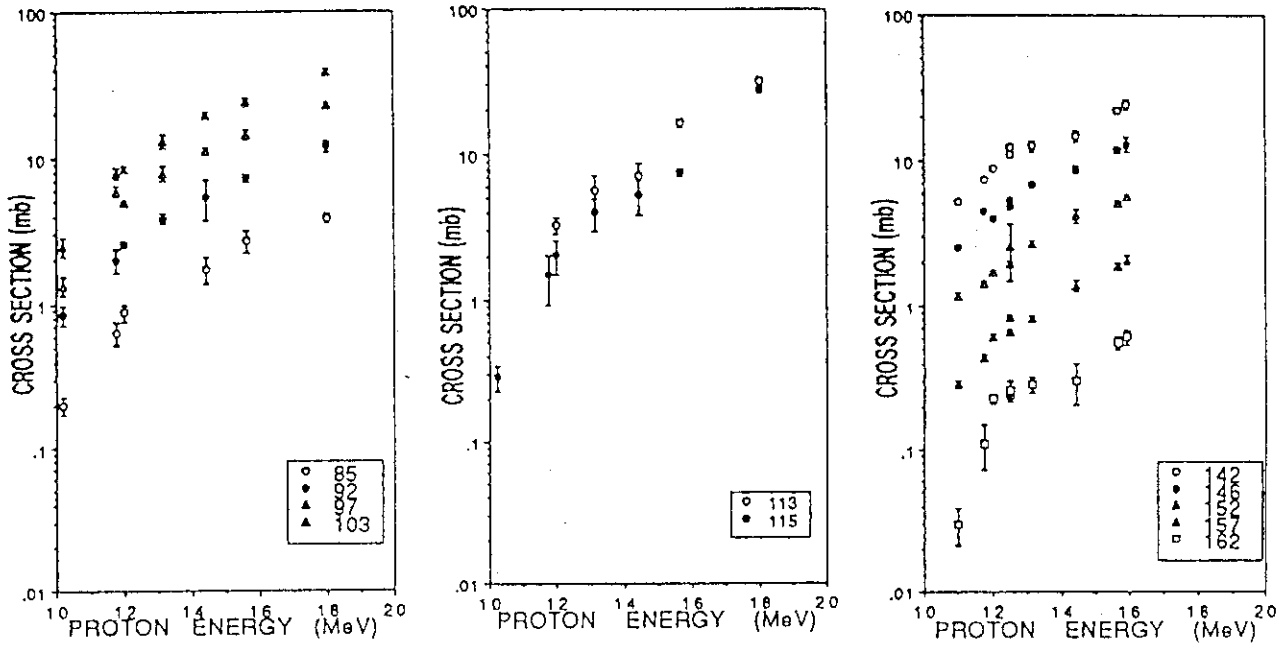

Fig.1 Excitation function of each mass products in proton-induced fission of ^{244}Pu.

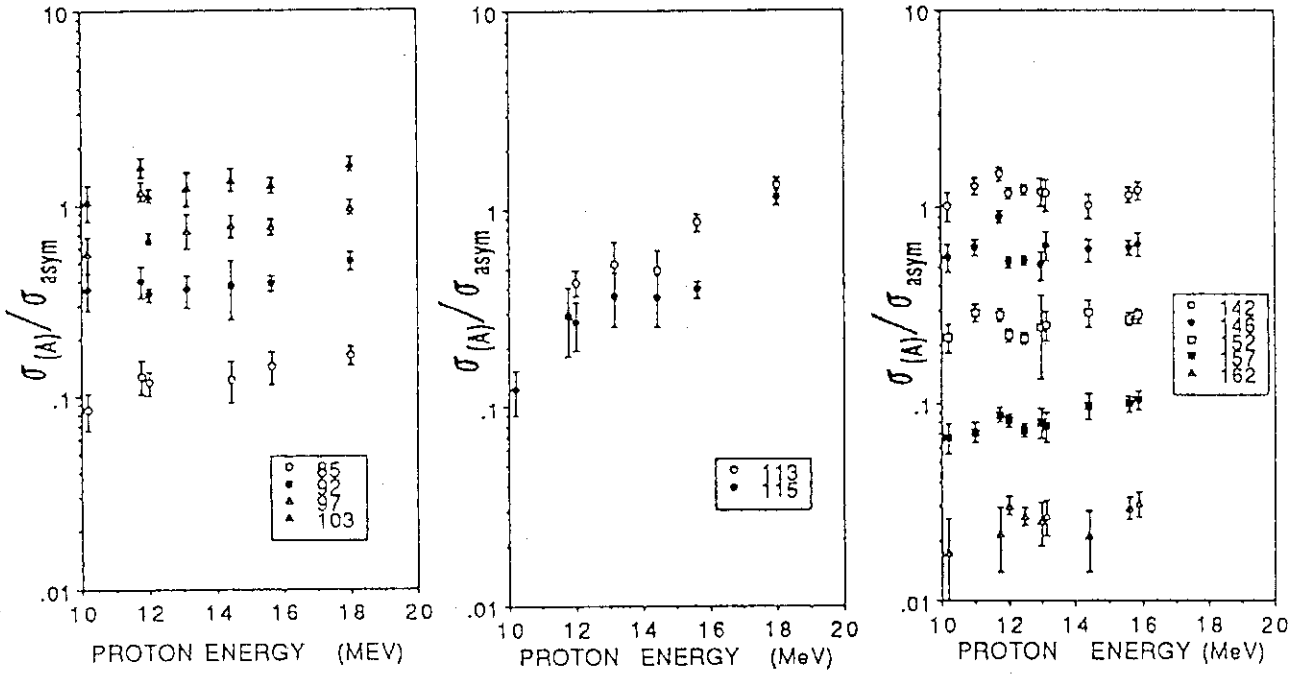

Fig.2 Cross section ratios $\sigma(a)/\sigma_{asym}$ as function of the incident proton energy. The average of the yields of ^{141}Ce and ^{143}Ce are used for σ_{asym}.

V NUCLEAR PHYSICS

5.1 IN-BEAM STUDY OF IN-103

Tetsuro ISHII, Mitsuhiko ISHII, Yuichi SAITO,
Mituo NAKAJIMA*, Masao OGAWA* and Akiyasu MAKISHIMA**

Department of Physics, JAERI, *Department of Energy Sciences,
Tokyo Institute of Technology, **National Defense Medical College

Nuclear structure of the nucleus ^{100}Sn is very interesting but this nucleus is located too far from the β-stability line to produce. Neighbors of ^{100}Sn, however, give a clue to investigating the double shell closure. Thus far we have studied the nuclei ^{106}Sn and ^{105}In[1,2]. The nucleus ^{103}In is another candidate of the nearest neighbors that we can observe. We have studied its excited states by in-beam γ-ray spectroscopy.

The nucleus ^{103}In was produced by the reaction ^{48}Ti(^{58}Ni, p2n) ^{103}In; a beam of 224 MeV ^{58}Ni ions was provided by the JAERI tandem accelerator. The target was a ^{48}Ti foil, 1.0 mg/cm^2, backed by a foil of natural titanium, 5.4 mg/cm^2, to stop the reaction products. The Si box was employed to select the reaction channel by charged-particle multiplicity[3]. Four Ge detectors, 30 % in relative detection efficiency, were employed to observe γ-rays; three of them were placed at the bottom and the both sides of the target, respectively, and the other at 20° with respect to the direction of the beam. The γ-ray anistropies were obtained from the γ-ray intensities observed at angles of 20° and 90°.

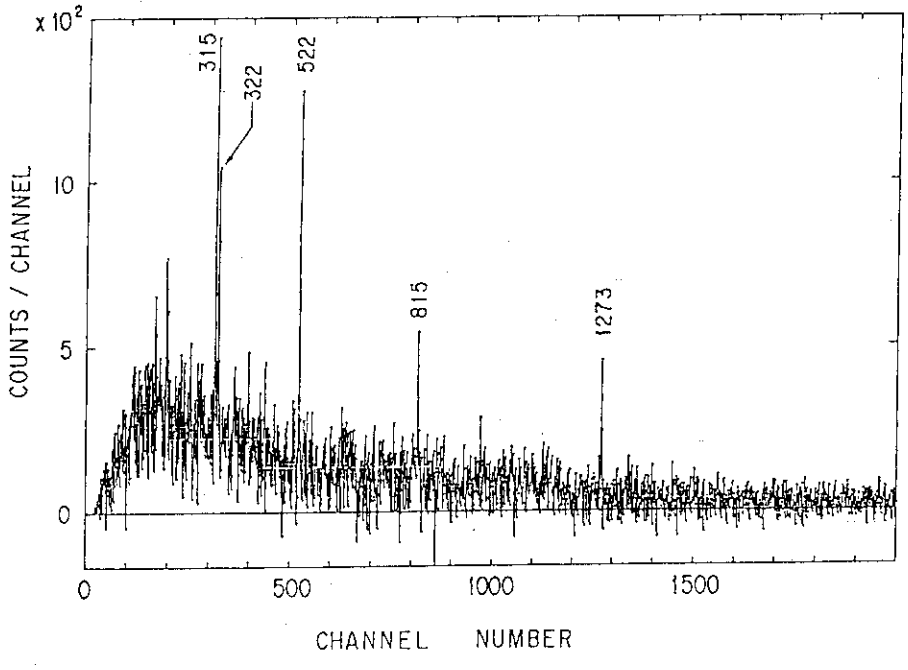

Fig.1 Gamma-rays emitted from ^{103}In.

Candidates of transitions in the nucleus ^{103}In were picked out from the p–γ spectrum with multiplicity M=1; their energies were 315, 815 and 1273 keV. Fig. 1 shows a p–γ–γ sum spectrum over the gates set on these transitions. In the present experiment, five transitions in cascade have been observed. The 1273 keV γ–ray is the strongest among them and shows the anisotropy of quadrupole type transition. Its energy is close to 1342 keV, the energy of the $13/2^+ \rightarrow 9/2^+$ transition in ^{105}In. Furthermore, the 522 keV γ–ray is of quadrupole type and 315 keV γ–ray of dipole type. On the basis of these facts, the level scheme of ^{103}In shown in fig. 2 has been built. For comparison the level scheme of ^{105}In are depicted there also.

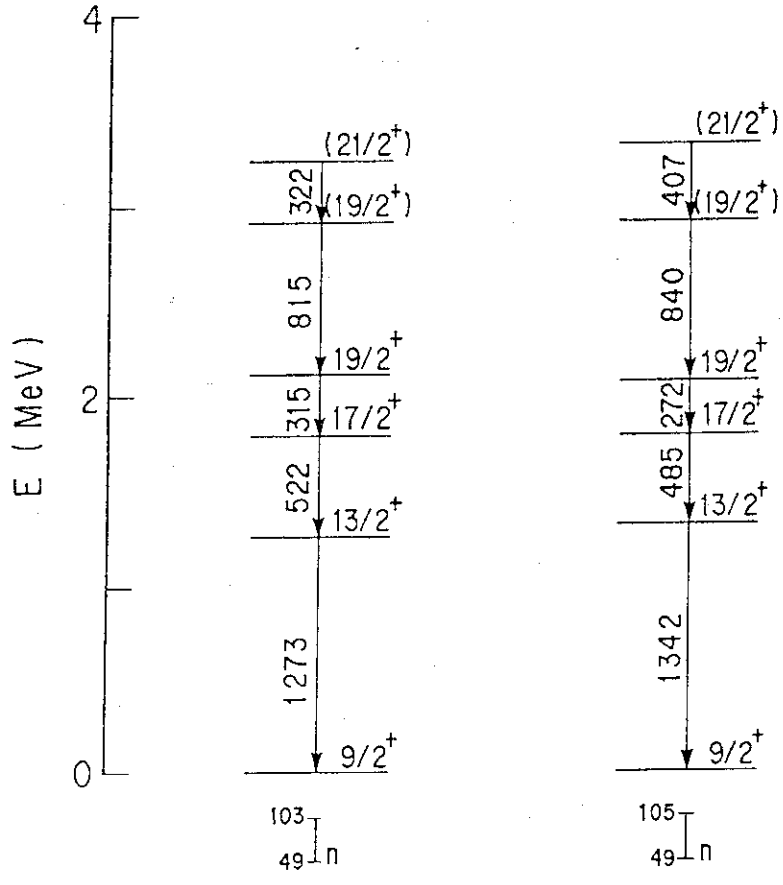

Fig.2 Level schemes of ^{103}In and ^{105}In.
The transition energies are given in units of keV.

References

1) T. Ishii et al.: 'Lifetimes of high–spin states in ^{106}Sn', submitted to Phy. Rev. C.
2) T. Ishii et al.: JAERI–M 89–119 (1989) 165.
3) M. Ishii et al.: in Nuclei off the line of Stability(ed. R. A. Meyer and D. S. Brenner, A.C.S., Washington D.C., 1986) p.350.

5.2 LIFETIMES OF EXCITED STATES IN IN–105,107

Tetsuro ISHII, Mitsuhiko ISHII, Yuichi SAITO,
Akiyasu MAKISHIMA[*], Mituo NAKAJIMA[**]
and Masao OGAWA[**]

Department of Physics, JAERI, [*]National Defense Medical College,
[**]Department of Energy Sciences, Tokyo Institute of Technology

We have measured the lifetimes of the $19/2^+$ and $17/2^+$ states in ^{105,107}In by the recoil distance method. The nuclei ^{105,107}In were produced by bombarding ^{56}Fe, 0.4 mg/cm^2, with a beam of 200 MeV ^{54}Fe ions. The Si box[1] helped us to select the reaction channel emitting three protons. The Si box was divided into halves, between which a simple plunger was inserted. The level scheme of ^{105}In had been built previously by the authors[2] and that of ^{107}In by Andersson et al.[3]. In the present experiment, the halflives of the $19/2^+$ and $17/2^+$ states have been measured:

$T_{1/2}(19/2^+) = 6(3)$ ps and $T_{1/2}(17/2^+) = 0.29(10)$ ns for ^{105}In
$T_{1/2}(19/2^+) = 28(8)$ ps and $T_{1/2}(17/2^+) = 1.1(3)$ ns for ^{107}In

The $19/2^+$ states in both nuclei possess almost the same B(M1) values. The B(E2) values of the $17/2^+$ states in ^{105,107}In are similar to those of the 6^+ states in the nuclei ^{106,108}Sn, respectively. This suggests that the ground state band in ^{105,107}In has the configuration: the proton hole $(\pi g_{9/2})^{-1}$ coupled to the core ^{106,108}Sn, respectively.

References

1) M. Ishii et al.: in Nuclei off the line of Stability(ed. R. A. Meyer and D. S. Brenner, A.C.S., Washington D.C., 1986) p.350.
2) T. Ishii et al.: JAERI–M 89–119 (1989) 165.
3) E. Andersson et al.: Phy. Rev. C 24 (1981) 917.

5.3 YIELD OF COULOMB EXCITATION OF THE UNSTABLE NUCLEUS ^{76}Kr

Masumi OSHIMA, Shin-ichi ICHIKAWA,[*] Yuichi HATSUKAWA,[**] Tsuneyasu MORIKAWA,[**] Byung-Joo MIN, Yasuyuki GONO,[***] Takeshi MURAKAMI,[****] Hideshige KUSAKARI,[*****] and Masahiko SUGAWARA[******]

Department of Physics, JAERI, [*]Department of Chemistry, JAERI, [**]Department of Radioisotopes, JAERI, [***]RIKEN, Wako-shi, Saitama 351-01, [****]Tokyo Institute of Technology, Oh-okayama, Meguro, Tokyo, [*****]Faculty of Education, Chiba University, Yayoi-cho, Chiba 260, and [******]Chiba Institute of Technology, Shibazono, Narashino, Chiba 275

We have previously reported the first observation of secondary-beam Coulomb excitation (COULEX) for an unstable nucleus ^{76}Kr.[1] An important point of this method is that electromagnetic matrix elements can be extracted directly by measuring the COULEX yield. In order to establish this method we undertook an experiment to measure the COULEX yield in an absolute basis.

At first we describe briefly the experimental method. The experimental setup used is shown in Fig. 1. The inverse reaction, ^{9}Be (^{70}Ge,3n) ^{76}Kr, was chosen to produce the secondary beam of ^{76}Kr. The 310-MeV ^{70}Ge beam was delivered by the tandem accelerator. The beam intensity was approximately 1 particle nA. The first and second targets were self-supporting foils of ^{9}Be and ^{208}Pb with thicknesses of 0.94 and 2.0 mg/cm^2, respectively. Under these conditions, the kinetic energy of the ^{76}Kr secondary beam was estimated to be 3.1 MeV/u. A γ-ray multiplicity filter placed at the first target position discriminates fusion events from COULEX or decay events there. The primary- and secondary-beam particles scattered by the second target were detected by four sectored plastic scintillators. Four germanium detectors at the second target position detect γ rays from the second target. The triple coincidence (multiplicity filter-plastic-germanium) selects fusion residues which are Coulomb excited by the second target and hit the plastic scintillators.

By measuring the absolute γ yield of ^{76}Kr with a Ge detector placed at the first target position, the secondary-beam intensity was derived to be $4.4 \cdot 10^5$ particles per second with the primary beam of 1 pnA: the ratio of the intensities i.e., conversion

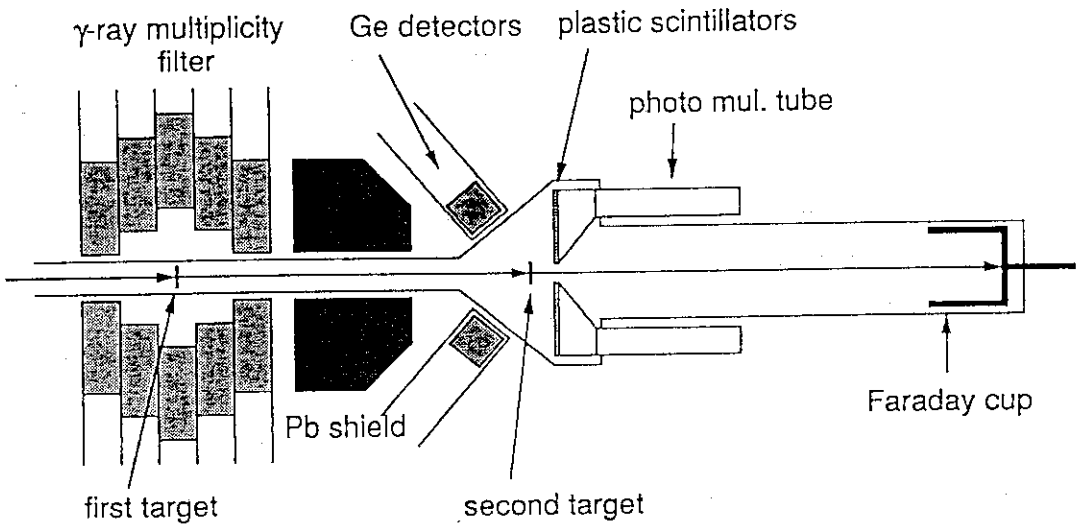

Fig. 1. Schematic view of experimental setup for secondary–beam COULEX experiment.

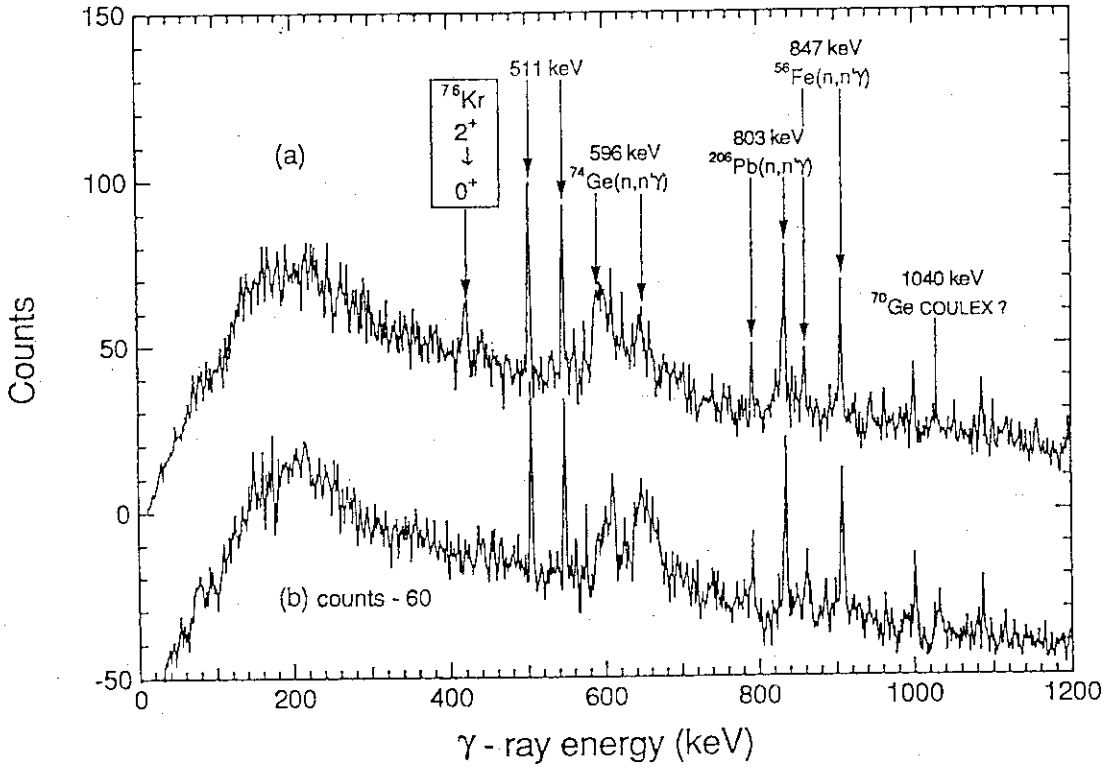

Fig. 2. (a) A spectrum corrected for Doppler shift. Two types of gated spectra were summed which correspond to different configurations of plastic and germanium detectors. The different Doppler shift corrections for the spectra cause double peaks for accidental–coincidence events. (b) A background spectrum obtained by setting a gate off the prompt peak in multiplicity filter and plastic coincidence.

efficiency from primary to secondary beam is $1.6 \cdot 10^{-5}$. The reaction cross section was extracted to be 660 mb, which can be compared with 410 mb obtained by ALICE code.[2] From the counting rate of the γ–ray multiplicity filter, the detection efficiency of the filter was determined to be 73 ± 13 %.

Recoils by evaporated neutrons and multiple scattering in the first target cause angular spread of the secondary beam. We have measured a ratio of the secondary beam hitting the secondary target with a size of 20 mmϕ by a catcher–foil technique. Firstly total reaction products produced in the first target were accumulated on an Al catcher foil placed just behind the target. Secondly the recoiled products reaching at the second target were collected on another foil which replaced the second target. The decay γ–rays from ^{76}Kr on the two foils were measured off–line to give relative yields of ^{76}Kr. Thus, the ratio of the secondary beam hitting the second target was determined to be 39 ± 3 %. In the inverse kinematics, the angular spread due to the multiple scattering is small as compared with the recoils by the evaporated neutrons, so that the loss of the secondary beam is brought about by the latter.

The energy of the ^{76}Kr is calculated to be 237 MeV from the reaction kinematics and average energy loss in the first target. The differential COULEX cross section is calculated by Winther de–Boer COULEX code [3] by using the known B(E2; $0 \rightarrow 2$) value ($0.56\ e^2b^2$).[4] The cross section of 3.2 barn is obtained from integration of the differential cross section from 19° to 51°, which is the angular range covered by the plastic scintillators. Since the cross section of 4^+ excitation is less than one tenth of that of 2^+ excitation, it is negligible. From product of the above quantities, the photopeak efficiencies of germanium detectors and the measuring time, we expect to obtain 410 ± 110 counts for the γ–ray yield of the secondary beam COULEX. The largest uncertainty of the estimation comes from the estimation of ^{76}Kr yield, which can be reduced in a future experiment. The expected γ–ray yield can be compared with the experimental yield of 360 ± 80 counts. They agree within the experimental accuracy.

This technique of the secondary–beam COULEX will be applicable to unstable nuclei with lifetimes longer than ≈ 20 ns which corresponds to the flight time between the first and second targets. By using this technique it becomes possible to obtain B(Eλ) value and to test nuclear models in a much wider region of nuclei than possible today. The objective of such study includes isomers as well as ground–states of unstable nuclei. Nuclear deformation above isomers, which has been rarely known so far, provides important information on nuclear shape evolution above isomers.

References

[1] M.Oshima et al., JAERI–M Report 90–139, p.163 (1990).

[2] F.Plasil et al., Phys. Rev. **C11**, 508 (1975).

[3] A.Winther and J.de Boer, *Coulomb Excitation*, ed. K.Alder and A.Winther, p.303 (Academic, New York, 1966).

[4] E.Nolte et al., Z. Phys. **268**, 267 (1974).

5.4 GIANT DIPOLE RESONANCE AT FINITE TEMPERATURE

Kazuyoshi FURUTAKA, Takeshi MURAKAMI, Jirohta KASAGI, Akira YAJIMA, Masumi OHSHIMA[a], Shin-ichi ICHIKAWA[a], Shunji NIIYA[b] and Hideki TOMINAGA[c]

Department of Physics, Tokyo Institute of Technology, [a]Department of Physics, JAERI, [b]Department of Physics, Kyushu Univ., [c]Department of Physics, Hiroshima Univ.

Studies of the giant dipole resonance (GDR) on highly excited nuclei provide direct information on the coupling of the GDR to fluctuations of the nuclear surface, and size and strength of the average potential at finite temperature. In our previous work[1], analyses of decay γ-rays from hot nuclei indicated that the width of the GDR increases drastically as the excitation energy (E_x) increases above E_x ~ 100 MeV. On the other hand, it has been discussed[2] that the increase of the width for E_x < 150 MeV is mainly due to the effect of the angular momentum and dependence on the thermal excitation energy is rather weak. Thus, further experimental studies are highly desirable to solve the discrepancy.

We have measured the GDR decay γ-rays as a function of γ-ray multiplicity as well as excitation energy, in order to study both effects, the spin and the exctation energy, separately. The experiments were carried out at the Tandem Accelerator Facility at JAERI. Gamma-rays were measured in the $^{32}S+^{100}Mo$ reactions at incident energies (E_i) of 150, 180 and 210 MeV, corresponding to E_x of 80, 103 and 125 MeV, respectively, in ^{132}Ce. Angular momenta brought into compound nuclei can be deduced from the γ-ray multiplicity data. High energy γ-rays were detected with a large BaF_2 detector consisting of 7 hexagonal crystals, placed at 90°. The γ-ray multiplicitiy associated with the high energy γ-

we plot the values of Γ versus E_{th}, instead of $N\gamma$. As seen, it can be said that Γ is a smooth function of E_{th}. Γ depends slightly on E_{th} for $E_{th} \leq 100$ MeV, but increases very rapidly for $E_{th} \geq 100$ MeV. The present observation supports our previous interpretation described in ref. 1). Systematic studies upto $E_{th} \sim 150$ MeV are highly desirable.

References

1) K. Yoshida, et al.: Phys. Lett. 245B (1990) 7.
2) J.J. Gaardhoje, et al.: Phys. Rev. Lett. 56 (1986) 1783.
D.R. Charkrabarty, et al.: Phys. Rev. C36 (1987) 1886.
3) F. Puhlhofer: Nucl. Phys. A280 (1977) 267.

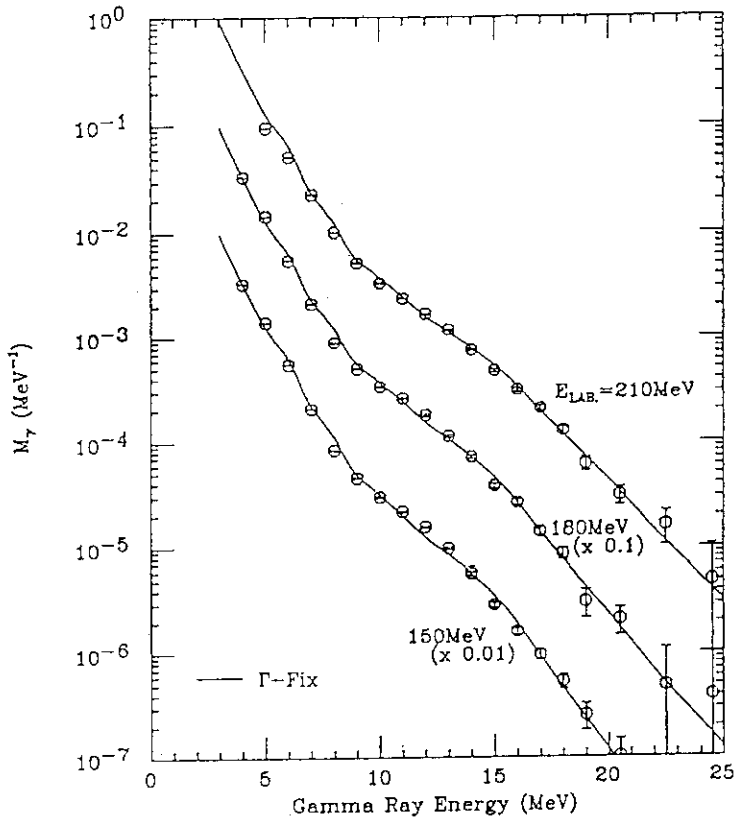

Fig. 1. Gamma-ray spectra for $N\gamma \geq 9$.

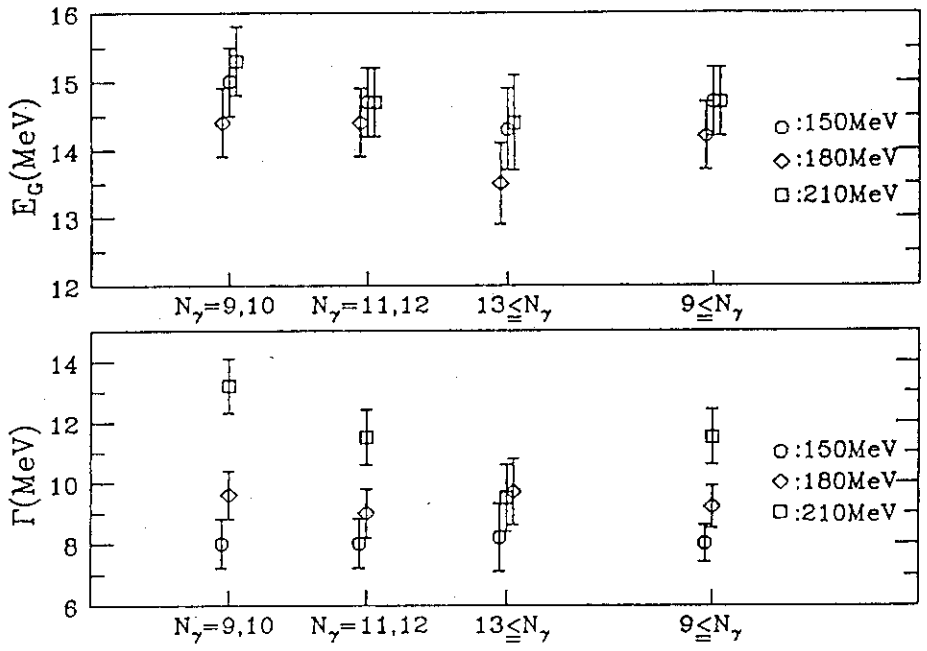

Fig. 2 Obtained resonance energy and width against Nγ.

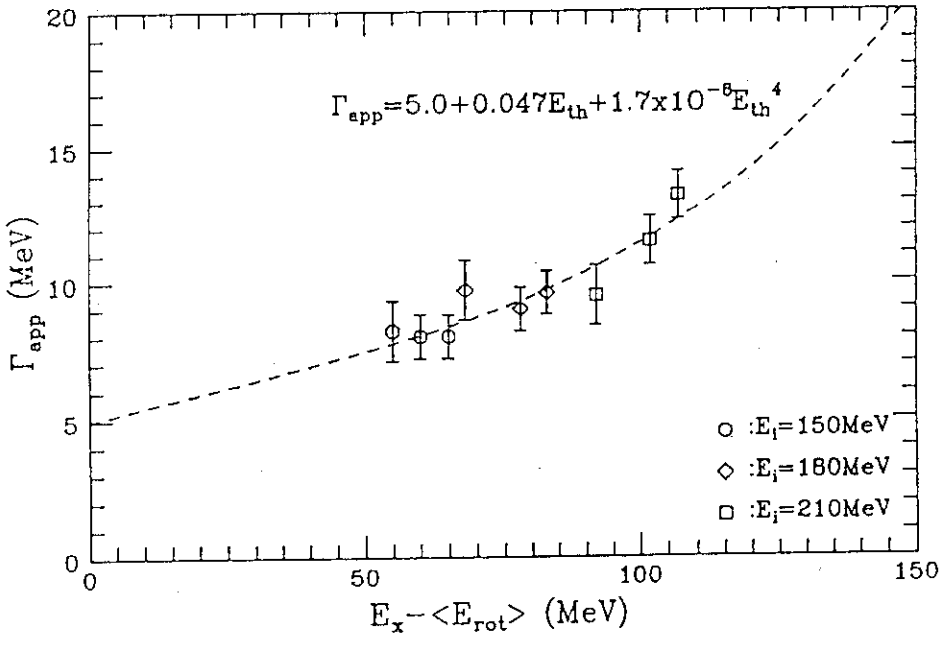

Fig. 3 Obtained width vs. thermal energy.

5.5 SPIN ALIGNMENT OF $^{12}C(2^+;4.44MeV)$ STATE IN RESONANT $^{16}C+^{12}C$ INELASTIC SCATTERING

Hiroshi FUJITA, Norihisa KATO*, Tsuyoshi SUGIMITSU*, Takumi OKAMOTO*, Makoto MATSUO*, Takashi MUKAE*, Shinichi MITSUOKA*, Yasuharu SUGIYAMA**, Hiroshi IKEZOE**, Kazumi IDENO** and Yoshiaki TOMITA**

Daiichi College of Pharmaceutical Sciences, *Department of Physics, Kyushu University, **Department of Physics, JAERI

It has been recognized that the γ–decay in flight of an excited nucleus broadens the line width in the momentum (or energy) spectrum of the decaying nucleus. The momentum shift due to the γ–recoil is the counterpart to the well known Doppler shift of γ–ray from a moving source. The shape of the line is determined by the angular distribution of the emitted γ–ray which has a characteristic pattern for each magnetic substate m. Characteristic line shape has been observed where a high momentum resolution has been achieved, and m–substate population has been obtained by unfolding the spectra[1].

So far we measured the spin alignment of the 3^- (6.13MeV) state of ^{16}O excited through the inelastic scattering of $^{12}C+^{16}O$ in an energy region of known resonances around E_{cm}=20MeV using a particle–γ angular correlation technique[2]. A population of m=±3 magnetic substates was dominant at four resonance energies of 19.7, 20.5, 22.0 and 22.6 MeV. This result was qualitatively reproduced by the band crossing model[3] which described the dominance of the aligned configuration in these resonances. We measured also the excitation functions of the mutual excitation channels of $^{12}C(2^+)+^{16}O(3^-)$ and $^{12}C(2^+)+^{16}O(1^-,2^+)$ in the energy range of E_{cm}=19.5 to 32.2 MeV[4]. A prominent intermediate structure was observed at $E_{cm}\approx$32MeV in the $^{12}C(2^+)+^{16}O(3^-)$ channel. The purpose of the present experiment is to clarify the physical processes that underlie the intermediate structure.

In the present experiment, we measured a spin alignment of an excited $^{12}C(2^+;$ 4.44MeV) state in a single $^{12}C(^{16}O,^{12}C(2^+))^{16}O$ and a mutual $^{12}C(^{16}O,^{12}C(2^+))^{16}O(3^-)$ excitations via a γ–ray recoil method. The experiment was carried out at JAERI tandem accelerator. We took an advantage of the reversed kinematics for backward angle measurement by bombarding a ^{12}C target ($50\mu g/cm^2$) with ^{16}O beam. Momenta of ^{12}C were measured with the heavy–ion magnetic spectrograph "ENMA"[5].

Momentum spectra of $^{12}C(2^+)$ in single and mutual excitations were measured in the range of laboratory angles from 4° to 17° with a step of 1° at a laboratory energy of 75MeV (E_{cm}=32.2MeV). Fig.1 shows typical spectra at θ_{lab}=7°. The left hand side of the figure shows the momentum spectrum of ^{12}C around Q–value of –5MeV and the right hand side shows the one around Q=–11MeV. The line shape broadened by the γ–ray recoil is seen clearly for the $^{12}C(2^+)$ peaks. The angular distributions of m–substate population of $^{12}C(2^+)$ obtained from the line shape analysis are shown in Fig.2. The left hand side of the figure corresponds to the result obtained in the single excitation of $^{12}C(^{16}O,^{12}C(2^+))^{16}O$ and the right hand side is the result in the mutual excitation of $^{12}C(^{16}O,^{12}C(2^+))^{16}O(3^-)$. We compare the results with simple resonance model calculations. The solid lines in the figures are calculated assuming single partial waves L and L' for the entrance and exit channels, respectively. L and L' are related by the aligned coupling of L'=L–2 and L'=L–5 for the single and mutual excitations with L=16,respectively. The data are reproduced well by such simple calculations.

References

1) Y.Sugiyama et al.: Z. Phys. A–Atoms and Nuclei 322 (1985) 579.
2) N.Kato, K.Anai, T.Tachikawa, H.Fujita, K.Kimura, T.Sugimitsu and Y.Nakajima: Phys. Lett. 120B (1983) 314
3) T.Tazawa, J.Y.Park and Y.Abe: Phys. Lett. 125B (1983) 30.
4) N.Kato, H.Fujita, T.Tachikawa, K.Kimura, T.Sugimitsu and Y.Nakajima: KUTL Report–1 (1985) p.106
5) Y.Sugiyama et al.: Nucl. Instrum. and Methods in Physics Research A281 (1989) 512.

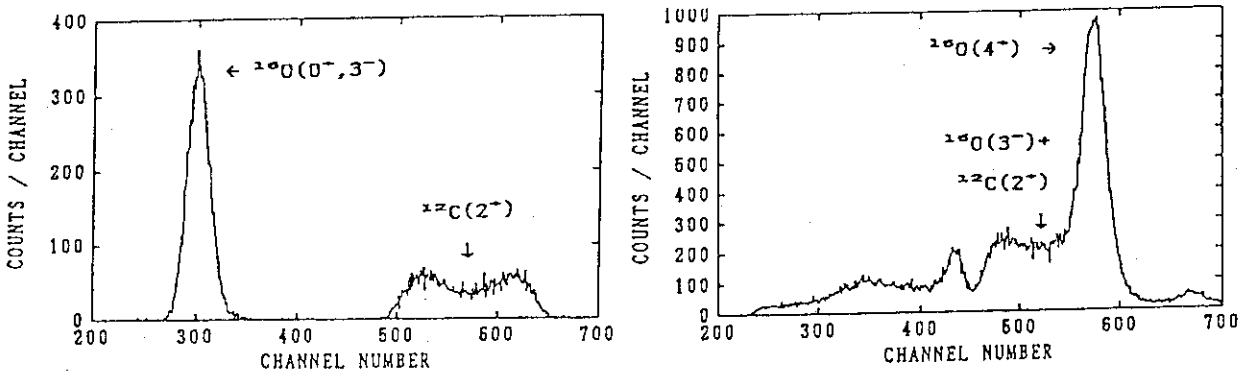

Fig.1 Typical momentum spectra of ^{12}C

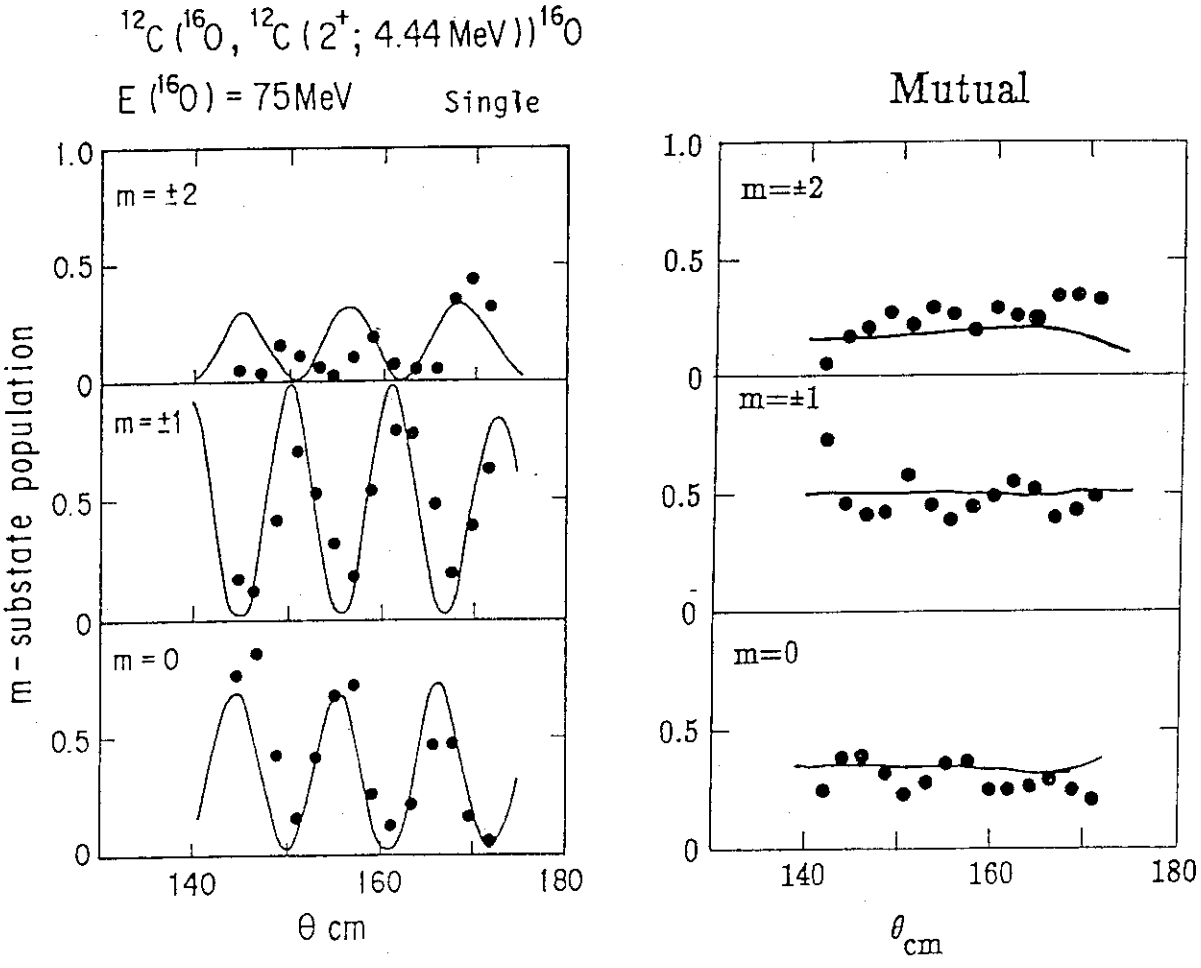

Fig.2 Angular distributions of m–substate population of $^{12}C(2^+;4.44MeV)$ in the single (left) and mutual(right) excitations. Solid lines are calculated assuming a simple resonance model described in the text.

5.6 A STUDY OF ELASTIC AND INELASTIC COLLISIONS OF $^{58}Ni+^{90,94}Zr$ AT NEAR-BARRIER ENERGIES

L.Corradi[1], D.R.Napoli[1], A.Dal-Bello[1], A.M.Stefanini[1], C.Signorini[2], Y.Sugiyama[3], H.Ikezoe[3], ,Y.Tomita[3], K.Ideno[3], H.J.Kim[3,6], B.J.Qi[3,7], Y.Nagashima[4], T.Masuda[4], H.Fujiwara[4], Yue Hu Pu[4], Y.Tagishi[4], T.Sugimitsu[5],

[1]INFN-Laboratori Nazionali di Legnaro, I-35020 Legnaro (Padova), Italy
[2]Dip. of Fisica, Universita di Padova and INFN-Sezione di Padova, Italy
[3]Department of Physics, Japan Atomic Energy Research Institute, Japan
[4]Tandem Accelerator Center, University of Tsukuba, Japan
[5]Faculty of Physics, University of Kyushyu, Japan
[6]on leave from Oak Ridge National Laboratory, Oak Ridge, USA
[7]on leave from Low Energy Atomic Physics Institute, Beijing, China

Heavy-ion collisions at near the Coulomb barrier energies are important when studying the interplay of nuclear structure and dynamics in determining the reaction mechanism. The study of elastic scattering may give, in particular, valuable information on the interaction potential and the relative importance of coupled reaction channels. With the aim of extending our knowledge to rather heavy systems, we have measured elastic scattering as well as the inelastic scattering to the lowest-lying states of $^{58}Ni+^{90,94}Zr$. For these systems, complete data sets already exist[1)] about evaporation residue and quasi-elastic transfer cross sections in the energy range near the Coulomb barrier.

The measurement of pure elastic scattering of heavy systems is a rather difficult task: several factors enter into play like e.g. strong kinematic energy spreads, the limited energy resolution of conventional detectors, the necessity of using very thin and homogeneous targets, the ability to discriminate reaction channels other than the elastic one. For these reasons we have made use of the heavy-ion magnetic spectrograph ENMA[2)] in JAERI.

The ^{58}Ni beams were obtained from the JAERI Tandem at energies of 232.5 and 247.5 MeV, and scattered Ni-ions and/or recoiling Zr-ions were analyzed by ENMA and detected at the focal plane with good energy resolution (650-750 KeV) as shown in Fig. 1. The spectrograph, through the combined effect of its magnetic elements, effectively corrects for the kinematic energy spreads which typically are 2-3 MeV/deg. A clear separation is seen in Fig. 1 between the elastic peak and the

low-lying inelastic excitations.

The angular distributions for pure elastic scattering of ^{58}Ni+^{90}Zr are shown in Fig. 2. A drop of the cross sections below the Rutherford limit is evident at angles forward of the grazing peak which is clearly observed at both energies. This is already an indication that an appropriate theoretical treatment of the data needs taking into account explicitly the coupling at least the Coulomb excitation plus inelastic scattering. Moreover, the experimental points at backward angles cover an angular momentum range which overlaps with fusion and transfer channels and this should give new information on the connections between the various processes. The energy resolution allows us to obtain cross sections for the excitation of the lowest 2^+ level of both projectile and target, at least for the ^{90}Zr case. For the ^{94}Zr case, the presence of the 2^+ excitation at 920 KeV make it difficult to discriminate that level from the elastic peak, especially at backward angles where the cross sections are small and the statistics rather poor, due also to the use of very thin ($10\mu g/cm^2$) strip targets.

A comparison of the present experimental results with the predictions of coupled-channels calculations, also in connection with the older data on fusion and transfer, gives interesting insight into the reaction dynamics of these soft-colliding heavy-ion systems. Fig. 3 shows the comparison of the pure elastic scattering angular distributions with the calculations by PTOLEMY coupled channel code for the system of ^{58}Ni+^{90}Zr at two energies. The agreement between experimental results and the calculation seems to be fine at 247.5MeV, especially coupled calculation in which coupling to first 2^+ state is taken into acount predicts fairly good in not only reaction region but also pure rutherford region. On the other hand, the calculation seems to be very hard to reproduce the results of experiment at 232.5MeV. The detailed analysis is still under way.

Reference

1) F.Scarlassara et al. Z. Phys. A338 (1991) 171

2) Y.Sugiyama et al. Nucl. Instr. and Meth. A281 (1989) 512

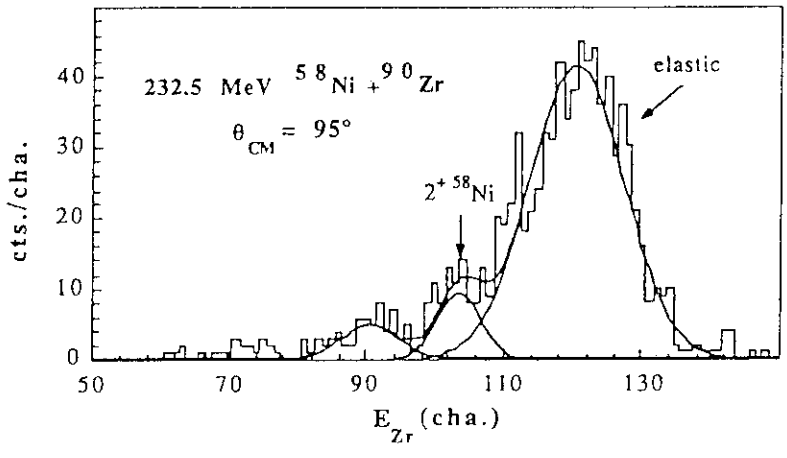

Fig. 1

Energy spectrum for Zr-like ions.

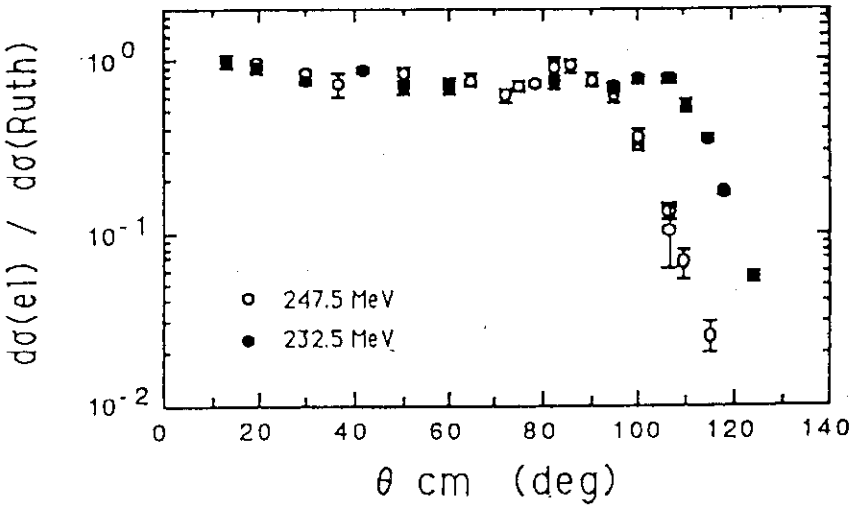

Fig. 2

Angular distribution for elastic scattering of ^{58}Ni+^{90}Zr at the two indicated energies.

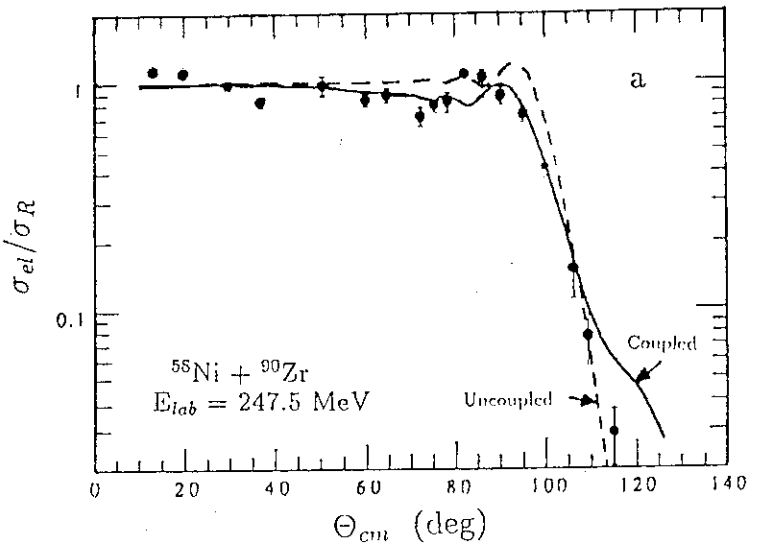

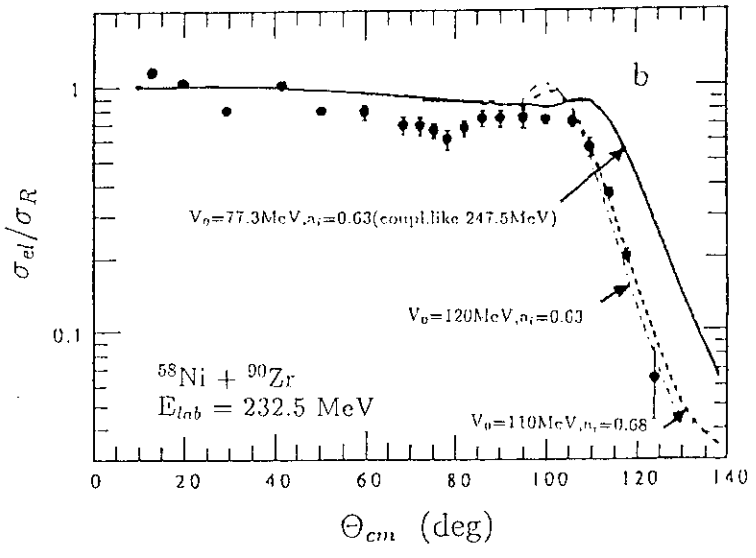

Fig. 3a and Fig. 3b

The coupled (solid curves) and uncoupled (dashed and dotted curves) are compared with the angular distribution for elastic scattering of ^{58}Ni+^{90}Zr at the two indicated energies.

5.7 $^{12}C \rightarrow 3\alpha$ STUDY BY USING A MULTI-ARRAYED TWO-DIMENSIONAL POSITION-SENSITVE DETECTION SYSTEM IN HEAVY ION REACTIONS

Kazumi IDENO[1], Tsutomu OHTSUKI[2,3], Yasuharu SUGIYAMA[1], Hiroshi IKEZOE[1], Susumu HANASHIMA[1], Yuichiro NAGAME[2], Hee Joong KIM[1,4] and Bujia Qi[1,5]

[1]Department of Physics, [2]Department of Radioisotopes, JAERI, Japan

One attractive feature in the measurement of $^{12}C \rightarrow 3\alpha$ decays for heavy ion reactions is that we can determine the excitation energies of the emitted ^{12}C fragment from kinematical correlations. This kind of measurements, called a particle resonance spectroscopy[1)], have a potential to provide unique information on the relationship between mutual excitations of the emitted fragments in the final stage of the reaction. Here the α-particles detection system must cover a wide range of solid angles depending on the excitation energies of the ^{12}C nucleus. For the excitation energies of ^{12}C below 9 MeV we use a multi-arrayed two-dimensional position-sensitive detection system[2,3)], which covers an opening angle less than 20 degrees. For the higher excitation energies up to 30 MeV, we use this system for the detection of one α-particle and five sets of closely-spaced paired Si(Li) detectors for the detection of the other two α-particles decayed via $^{8}Be_{g.s.}$ nuclei. Fig. 1 shows a schematic diagram of the multi-arrayed two-dimensional position-sensitive detection system. Measurements and analyses for the $^{16}O + ^{60}Ni$ reaction at 90 MeV are now in progress.

References

1) S. Kubono: Preprint HMI-P 86/12 R (Hahn-Meitner Institute, 1986).
2) K. Ideno et al.: JAERI-M 90-139 (1990) p. 149.
3) K. Ideno et al.: Nucl. Inst. and Methods A302 (1991) 385.

---

[3]Permanent address: Laboratory of Nuclear Science, Tohoku University, Japan

[4]on leave from Oak Ridge National Laboratory, Oak Ridge, USA

[5]on leave from Institute of Atomic Energy, Beijin, China

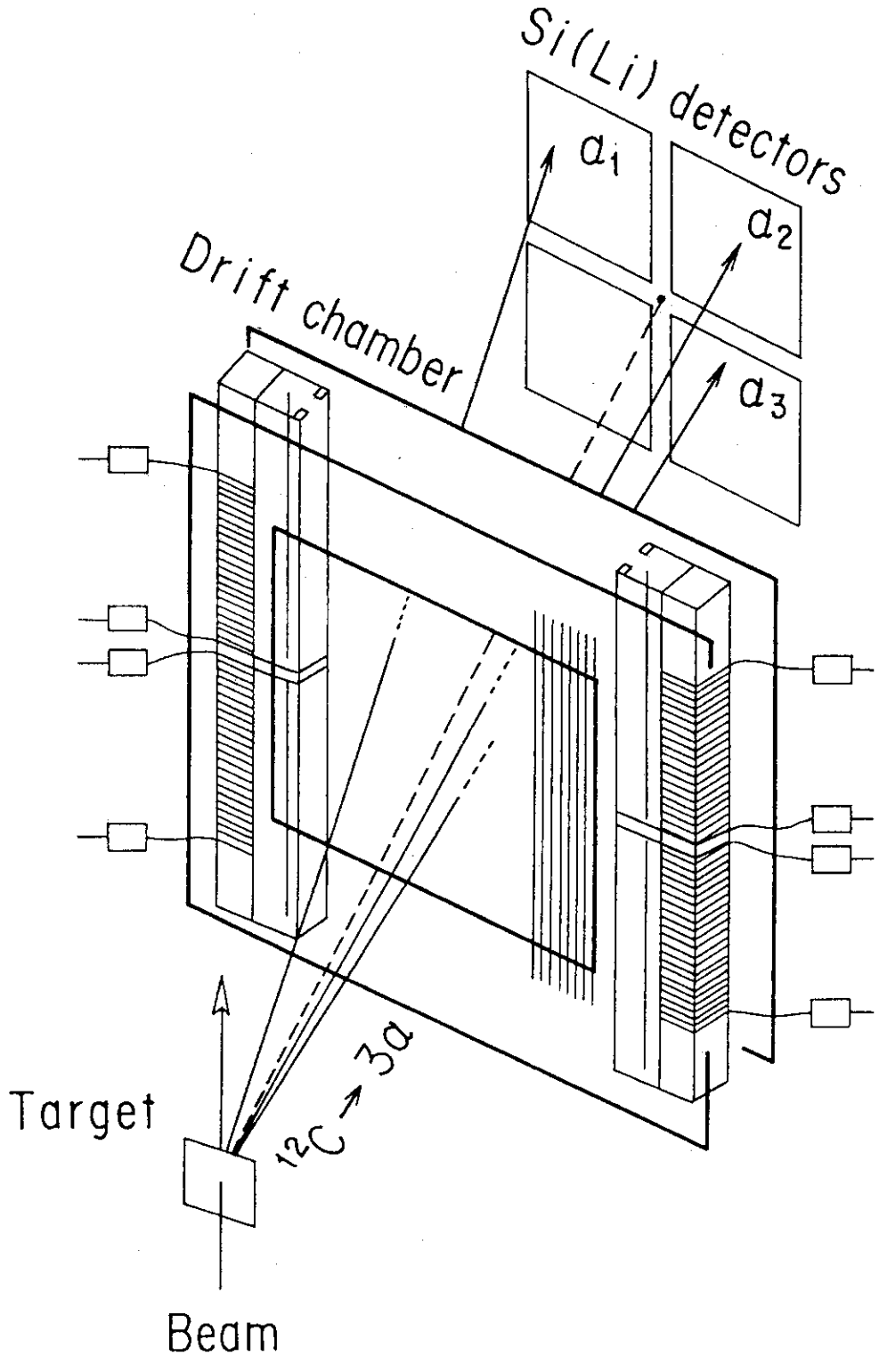

Fig. 1 Schematic diagram of a multi-arrayed 2-dimensional position-sensitve detection system for α-particles.

5.8 CHARGED PARTICLE EMISSIONS IN FISSION PROCESS

Hiroshi IKEZOE, Naomoto SHIKAZONO, Yuichiro NAGAME,
Tutomu OHTSUKI, Yasuharu SUGIYAMA, Yosiaki TOMITA,
Kazumi Ideno, Ikuo KANNO, H.J. Kim*, B.J. Qi** and
Akira IWAMOTO

Department of Physics, JAERI

1. Introduction

The time scale of fission process has been extensively studied by measuring neutron emitted before scission[1,2]. Experimental results that pertain to pre–scission neutrons suggest that the fission process is so slow that about two times as many neutrons are emitted than the statistical model predictions. Charged particle data associated with fission are rather scarce at low excitation energy region (40 ~ 120 MeV). Thus we have measured pre– and post–scission charged particles (proton and α particles) for the $^{19}F + ^{181}Ta$, ^{197}Au, ^{208}Pb, $^{28}Si + ^{197}Au$, ^{208}Pb and $^{16}O + ^{197}Au$ reactions.

2. Experimental Methods

Fission fragments were measured at backward angles ($\theta_f = 105 \sim 160$ deg.) by two solid state detectors (thickness of 60 μm and active area of 300 ~ 400 mm^2) which sustained large solid angles (50 ~ 60 msr). Light charged particles were measured by four solid state ΔE–E detector telescopes in coincidence with fission fragments. Thicknesses of ΔE and E detectors were 30 μm and 2 mm, respectively. These detector telescopes were placed in and out of the reaction plane.

3. Experimental Results

Energy spectra of charged particles measured in coincidence with fission fragments show a low and a high energy components. The low energy component corresponds to the charged particles emitted from excited fission fragments (post–scission emission); the high energy component corresponds to the charged particles emitted from compound nucleus (pre–scission emission).

The energy spectra for the pre– and post–scission emissions were calculated by using the statistical model code Pace2[3]. Although the calculation reproduces the shape of pre– and post–scission energy spectra very well, the calculated pre–scission emission energies are systematically higher both for the protons and α particles: if we shift down the energies by the amounts of Δ_p and $\Delta\alpha$ for protons and α particles[4], respectively, the calculation reproduces both the shape and position of the experimental pre–scission spectra. The

shifting down of energy necessary to fit the data implies a reduction of emission barriers which is a common feature of charged particle evaporation from excited nucleus[5].

The pre–scission multiplicities for proton and α particle were obtained by integrating the out–of–plane angular distributions. The results are shown in Fig. 1 and 2 as a function of U (compound nucleus excitation energy).

The pre–scission multiplicities were calculated using Pace2 taking into account the observed energy shifts[4]. The level density parameter was assumed to be $A_{cn}/10$, where A_{cn} is the mass number of the compound nucleus. Calculations with the ratio of level density at saddle point and ground state $a_f/a_n = 1.00$ (dashed lines) and 1.02 (solid lines) are shown in Fig. 1 and 2. The overall agreement between the data and the calculated results is good within the range of $a_f/a_n = 1.00 \sim 1.02$. The systematical deviation from the present statistical model calculations as reported in the analysis of the neutron multiplicity[2] is not observed in the present excitation energy regions.

The post–scission proton and α particle multiplicities were obtained by assuming isotropic emissions in the rest frames of fission fragments and are shown in Fig. 3 as a function of U. The observed post–scission multiplicities increase with U, especially for the heavy reaction systems where the post–scission multiplicities are $2 \sim 3$ times larger than those of lighter systems. This may be due to the fact that the effective Q–value for the symmetric mass division, $Q_{eff} = Q - TKE$, is larger for heavier systems and the Q–value for the charged particle emission from fission fragment is also larger for heavy fragments.

4. Discussions

The present statistical model calculation using Pace2 does not take into account following time regions: the transient time τ_t during which fission width reaches a stationary value at saddle point and the saddle–to–scission time τ_{ssc}. Pre–scission charged particles, as well as neutrons, can be emitted in the both time regions. The α particle emitted in the descent from saddle to scission may be concentrated in the direction ($\theta_t = 90$ deg.) perpendicular to the emission direction of fission fragments. This is due to focusing of α particle trajectories in the strong Coulomb fields of two fragments, and focused α particles may be identified as ternary events. It turns out that the pre–scission α particles, which do not show such focusing at $\theta_t = 90$ deg., may be attributed to emissions during the transient time τ_t. The emission during a finite τ_t should result in excess particles compared to the statistical model calculations because of the fission hindrance in this time period. The upper limit of τ_t is obtained from the present data as about 10^{-20} sec when $a_f = a_n = A_{cn}/10$ is assumed.

As reported in Ref. 2), if the all observed pre–scission neutrons are emitted during the transient time τ_t, the long transient times of few 10^{-20} to 10^{-19} sec are required to reproduce the observed pre–scission neutron multiplicities. This time scale is longer than

the present results and suggests that the excess neutrons over the statistical model predictions may be emitted during the saddle–to–scission region.

As shown in Fig. 3, the post–scission charged particle data show the steep increases with U. This trend is inconsistent with the post–scission neutron data which are roughly independent of U [2]. The observed post–scission neutron multiplicities indicate that the average excitation energy per fission fragment is about 25 ~ 30 MeV. The Pace2 calculations for symmetrically divided fragments predict rather small values (~ 0.005 to ~ 0.01) of the post–scission charged particle multiplicities for the present reactions with such low excitation energies. Although these calculations do not agree with the data, it should be noted that the Q–values for the proton and the α particle emissions from fission fragments increase with the fragment mass number. The emission probabilities of the charged particles are therefore sensitive to the excitation energies of heavy fragments which may be different from those of symmetrically divided fragments. Thus, it is necessary to get more information about the relations of the charged particle emission to the fragment mass numbers and the total kinetic energy.

* On leave from Oak Ridge National Laboratory, Oak Ridge, TN 37831, U.S.A.,
** On leave from Institue of Atomic Energy, Beijing 102413, China

References

1) A. Gavron, A. Gayer, J. Boissevain, M.C. Britt, J.R. Nix, A.J. Sierk, P. Grangè, S. Hassani, H.A. Weidenmüller, J.R. Beene, B. Cheynis, D. Drain, R.L. Ferguson, F.E. Obenshain, F. Plasil, G.R. Young, G.A. Petitt, and C. Butler, Phys. Letts B176 (1986) 312.
2) D.J. Hinde, R.J. Charity, G.S. Foote, J.R. Leigh, J.O. Newton, S. Ogaza, and A. Chattejee, Nucl. Phys. A452 (1986) 550.
3) A. Gavron, Phys. Rev. C21 (1980) 230.
4) H. Ikezoe, N. Shikazono, Y. Nagame, T. Ohtsuki, Y. Sugiyama, Y. Tomita, K. Ideno, I. Kanno, H.J. Kim, B.J. Qi and A. Iwamoto, Proceedings of Fourth International Conference on Nucleus–Nulceus Collisions, Kanazawa, Japan, June 10–14, 1991, to be published in Nucl. Phys.
5) J.M. Alexander, D. Guerreau, and L.C. Vaz, Z. Phys. A305 (1982) 313.

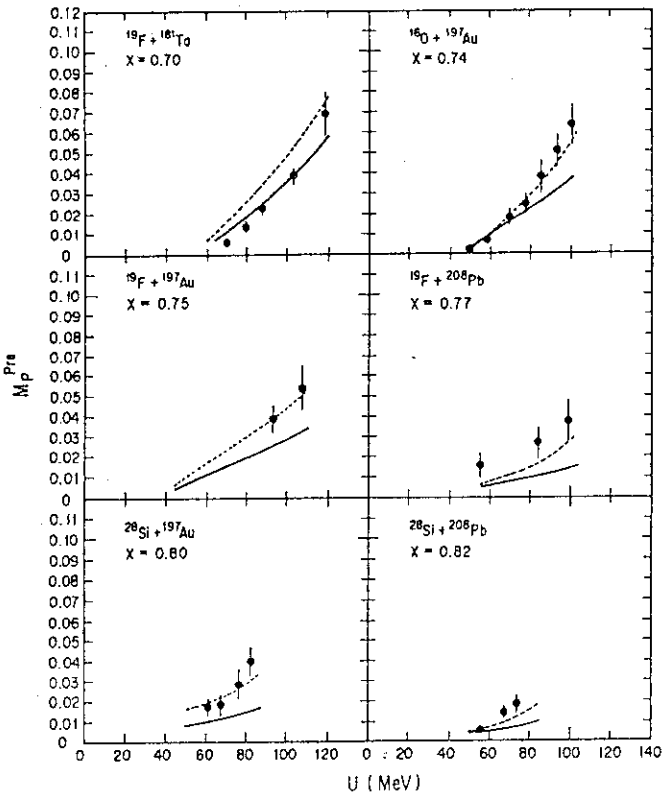

Fig. 1. Pre–scission multiplicities for proton as a function of compound nucleus excitation energies. The statistical model calculations with a_f/a_n = 1.00 and 1.02 are shown as dashed lines and solid lines, respectively. Fissility parameters are shown as x.

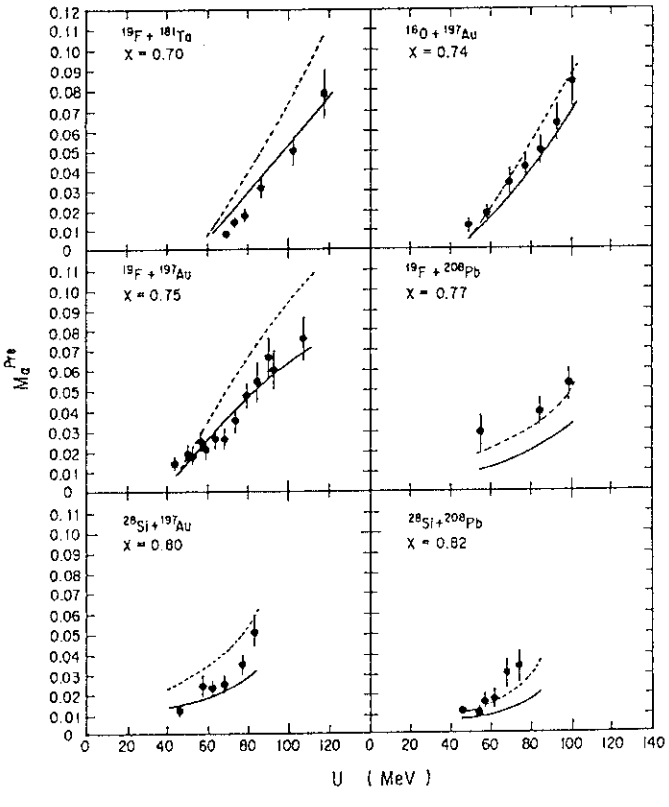

Fig. 2. Same as Fig. 1 for pre–scission α particle multiplicities.

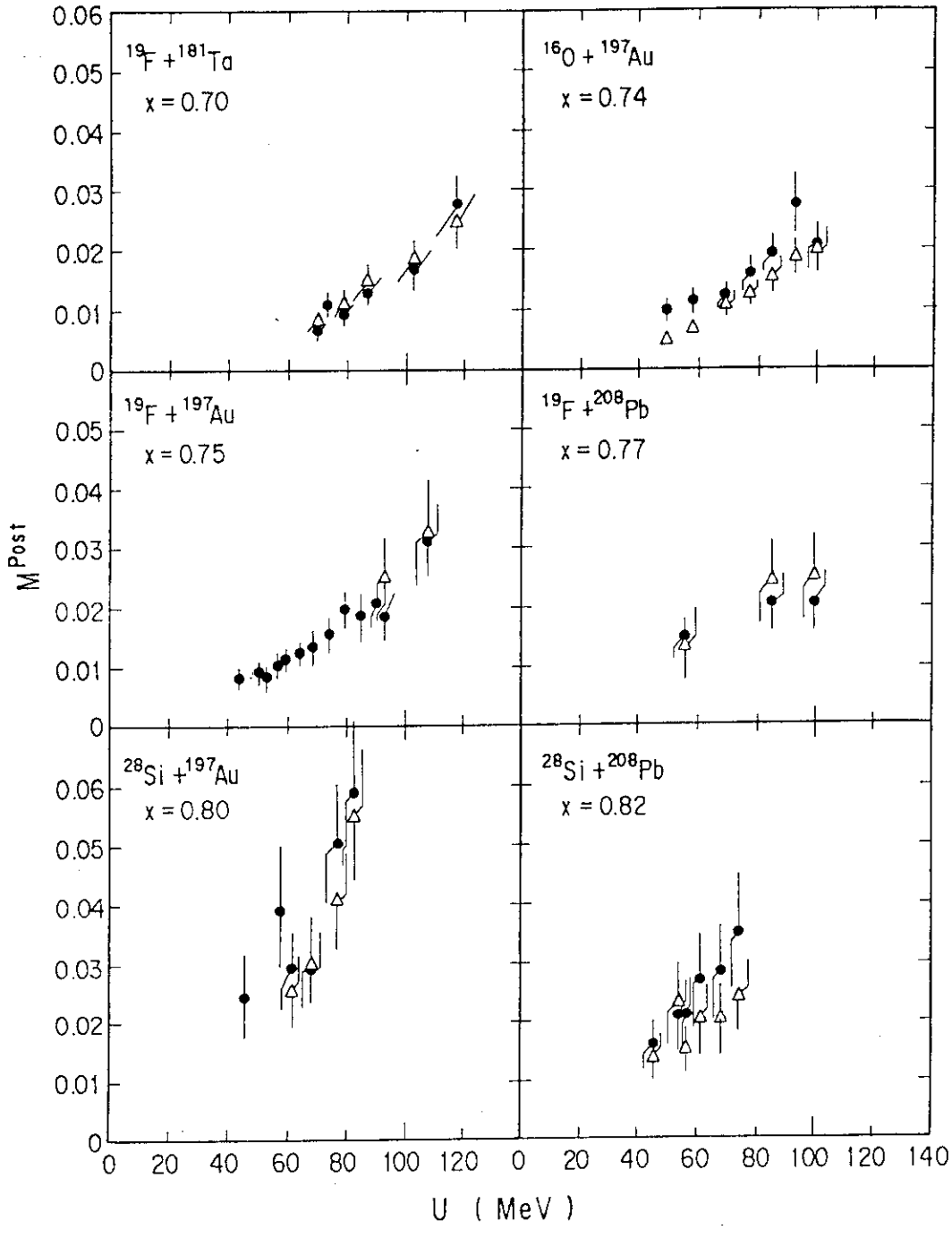

Fig. 3. Post–scission multiplicities for proton (open triangles) and α particle (solid points) as a function of compound nucleus excitation energies.

5.9 DOUBLE γ PHONON EXCITATION IN γ SOFT NUCLEI

Michiaki SUGITA

Department of Physics, JAERI

Using the interacting boson model-2 (sd-IBM-2), double γ phonon excitation is investigated.

Low lying excited bands of axially symmetric nuclei can be understood in terms of β and γ vibrations. The double γ phonon state of these nuclei appears in an energy region (~ 2MeV) of two quasiparticle states. It has not been known how strongly these quasiparticle states couple with the double phonon state. When strong coupling, the double phonon state cannot be observed experimentally.

In so-called γ soft nuclei, the γ band lies in a relatively low excitation energy ~500 keV so that the influence of the quasiparticle states is negligible. However, it is not evident at all that the β and γ phonon picture does hold for such nuclei .

The present investigation aims at clarifying band structure of the γ soft nuclei in terms of β and γ phonons by use of the interacting boson model (IBM). The IBM is used in explaining several collective phenomena in rare earth nuclei. One of the characteristics of the IBM is that it is rotationally invariant and its hamiltonian can be solved exactly. Therefore one can discuss the γ soft nuclei, getting rid of inevitable ambiguities encountered in theories constructed within the intrinsic frame.

Since the IBM in itself does not contain β and γ variables within its framework, some procedure is necessary to see phonon structure of the IBM wavefunctions. In a present study, we take the procedure of using the intrinsic state and angular-momentum projection. We introduce there a *reference* state which is axially symmetric and a bose condensate, and on which state the phonons are built. We use Tamm-Dancoff (TD) approximation for constructing the phonon states and restrict the number of phonons to two in the present study.

Calculations were done for the Os isotopes, one of typical nuclei soft against the γ deformation. We compare results of three calculations: the first one is the exact calculation, the second is one-phonon approximation and the last is two-phonon approximation. We shall refer to these three calculations as NPBOS, TDBOS and PHBOS, respectively. The energy systematics of the excited $I^{\pi}=0^{+}$ states are shown in Fig. 1a and those of 2_{γ} in Fig. 1b. In the figures, the rectangular symbols are NPBOS, the dashed lines TDBOS, and the solid lines PHBOS results, respectively. Fig. 2 shows probabilities of finding the exact wavefunctions

in the corresponding approximate states. The third 0^+ in TDBOS is a member of the so-called isovector excitation with Ex = 2~3 Mev, and is not drawn in the figures.

Present study shows not only PHBOS but also TDBOS are good approximations for the β, γ and ground bands of $^{184,\ 186}$Os, and thus indicates the axial symmetry of these nuclei. Also, the quality of the TDBOS approximation decreases with A, reflecting the ingredients of the nuclei towards the γ softness. Even for ^{A}Os ($A \geq 188$), the picture holds with 90% probabilities that the ground band is axially symmetric and the γ band is the one phonon excitation. However, TDBOS fails completely in describing the $0^+(2)$ bands. Over the current range of A, PHBOS is still a good approximation for not only the $0^+(2)$ but also the $0^+(3)$ states. It turns out from the analysis of the wavefunctions that one β and two γ phonon states mixes in $0^+(2)$ and $0^+(3)$. Rather pure γ phonon appearing in the 2_γ states and double γ phonon mixing in the excited 0^+ bands suggest a strong correlation between the β and γ oscillations occurring in the nuclear surface, although these two modes of oscillation are usually considered rather independent.

We would like to say in the closing that the double γ phonon states can be observed experimentally in the low lying excited 0^+ bands of the γ soft nuclei.

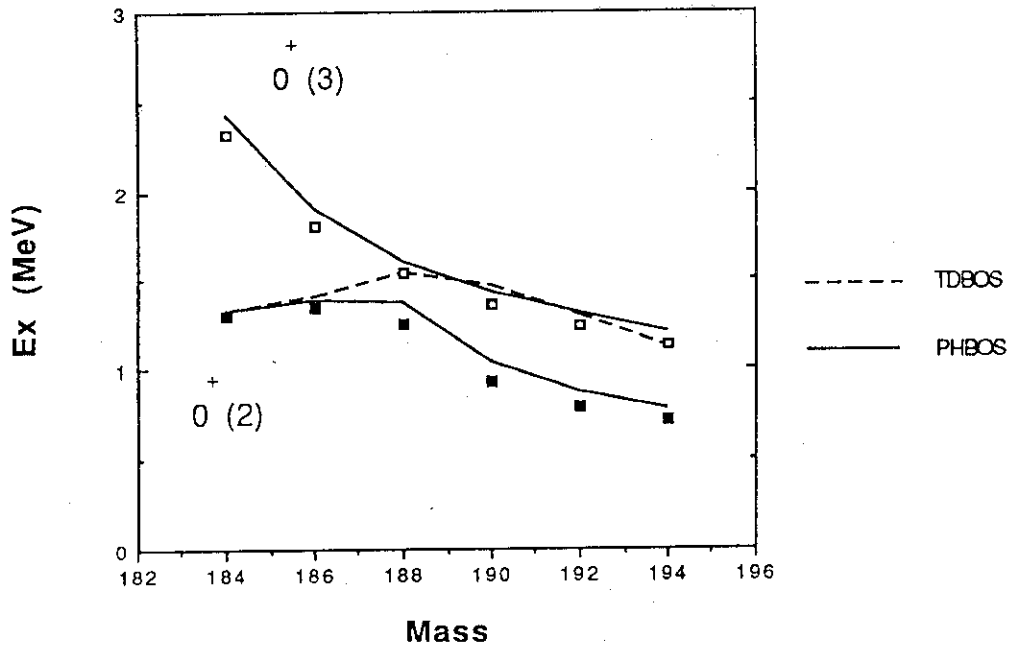

Fig. 1a Comparison between NPBOS, PHBOS and TDBOS results for excited 0+ states in the Os isotopes

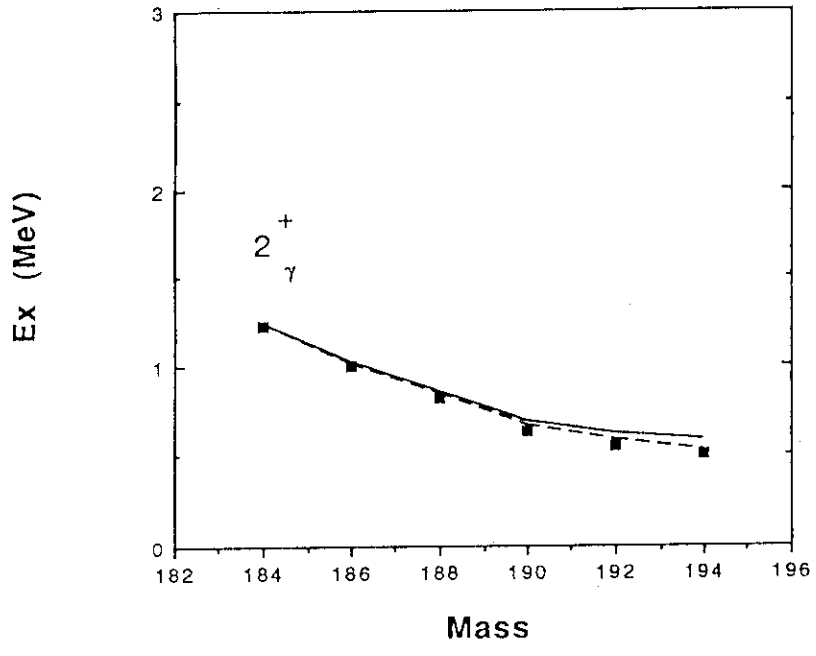

Fig. 1b Comparison between NPBOS, PHBOS and TDBOS results for 2+ states of gamma bands in the Os isotopes

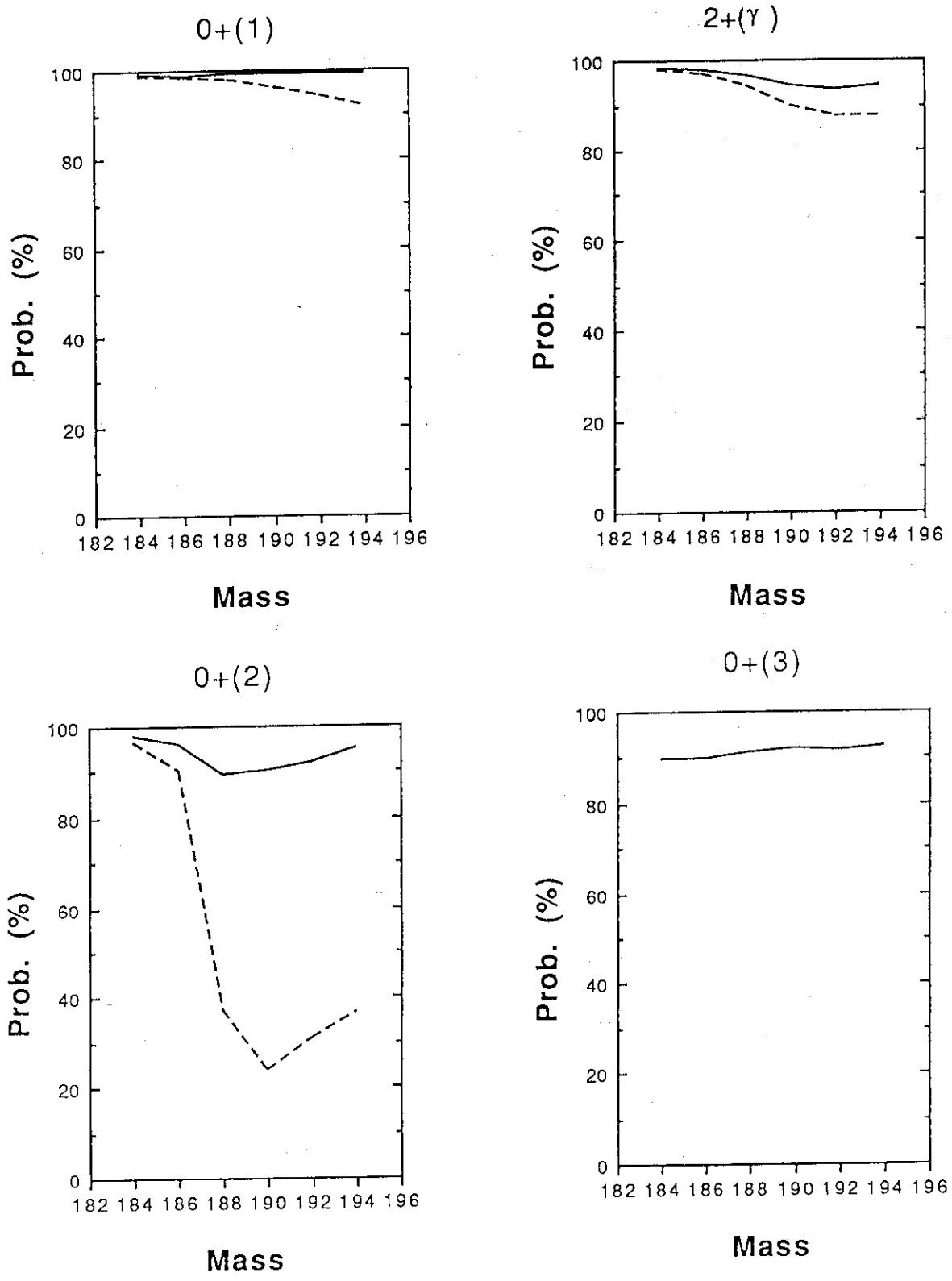

Fig.2 Probability of finding the exact wavefunctions in the approximate states of the Os isotopes

5.10 SUBBARRIER FUSION AND RENORMALIZATION OF OPTICAL POTENTIAL

Akira IWAMOTO and Koji NIITA

Department of Physics, JAERI

1. Introduction

To understand the mechanism of subbarrier fusion cross section , we develop a new formalism based on WKB approximation. Special interest is paid to the change of optical potential caused by the coupling of relative motion to intrinsic excitation. Renormalization of real and imaginary optical potential in classically forbidden region is calculated. This potential will be helpful to understand the dispersion-relation interpretation of the subbarrier fusion cross section[1)]. Our concern is the general discussion of the potential change and thus we use the one-dimensional model with simple coupling potential which leads to a closed-form expression for the induced potential.

2. Formalism

Hamiltonian of the system is written as

$$H = H_0(r) + v(r,\xi) + h(\xi)$$

$$= \{ H_0(r) + V(r) + iW(r) \} + \{ v(r,\xi) - V(r) - iW(r) \} + h(r), \quad (1)$$

where relative coordinate r is coupled to intrinsic coordinate ξ through interaction $v(r,\xi)$. $H_0(r)$ is unperturbed Hamiltonian of relative motion, $V(r)$, $iW(r)$ are induced potentials which will be fixed later, and $h(\xi)$ is intrinsic Hamiltonian. The condition to fix $V(r)$ and $W(r)$ is that

$$\overline{v(r,\xi)} = \{v(r,\xi) - V(r) - iW(r) \} , \quad (2)$$

will give no effect on the elastic wave function.

Wave function is expanded as

$$\Psi = \Sigma c_i(r)\chi(r)\varphi_i(\xi) , \quad (3)$$

where

$$h(\xi)\varphi_i(\xi) = \varepsilon_i\varphi_i(\xi) , \quad (4)$$

and by definition,

$$\{ H_0(r) + V(r) + iW(r) \} \chi = E\chi \ . \tag{5}$$

For the wave function χ we assume

$$\chi^{(\pm)}(r) = \frac{1}{\sqrt{k}} \exp\left(\pm \int k \, dr \right) , \tag{6}$$

where the generalized momentum k is given by

$$k(r) = \frac{1}{\hbar} \{ 2M(V_0 + V + iW - E) \}^{1/2} \ . \tag{7}$$

We solve the Schrödinger equation

$$H\Psi = E\Psi \ , \tag{8}$$

in the tunneling region (II) shown in fig.1 . We impose incoming-wave boundary condition at inner turning point a. $c_i \cdot \chi$ is given more explicitly as

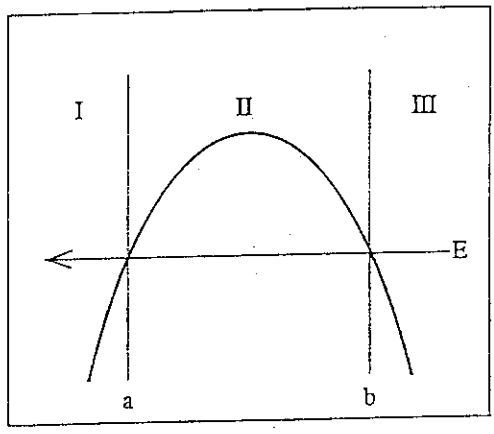

Fig.1

$$c_i \cdot \chi = c_i^{(+)} \chi^{(+)} + c_i^{(-)} \chi^{(-)} \ , \tag{9}$$

where increasing (+) and decreasing(-) components appear.

We assume a so-called adiabatic approximation written in the form

$$\left| (\hbar\omega + | \overline{v_{ij}} |) / (V_0 + V + iW - E) \right| << 1 \ . \tag{10}$$

If we put

$$\Psi = \chi^{(+)} \sum c_i \varphi_i = \chi^{(+)} \Phi \ , \tag{11}$$

we obtain the equation written as

$$\frac{d\Phi}{dr} = \frac{m}{\hbar k} (h(r) + \bar{v}(r, \xi)) \Phi \ , \tag{12}$$

where m is the mass parameter for the intrinsic excitation. If we further assume the linear coupling to intrinsic state

$$v(r, \xi) = f(r) \, \xi \ , \tag{13}$$

the basic equation can be solved in closed form.

4. Solution

If the above conditions are satisfied, the coherent-state technique can be applied to solve the equation. When the wave function is in its ground state at the outer turning point b, the subbarrier wave function is expressed in the form[2)]

$$\Phi = e^{A} \sum_{n} \frac{(B)^n}{n!} |n> \ , \tag{14}$$

where A and B are given functions. We impose the condition

$$\frac{dc_0(r)}{dr} = 0 \ , \tag{15}$$

which means that the ground-state wave function is expressed in the WKB form with complex momentum. This condition leads to the equation

$$V+iW-\frac{1}{2}\hbar\omega = \frac{1}{2\hbar\omega} f(r)\ exp\ \{ \frac{m\omega}{\hbar}\int^{r} \frac{1}{k}\,dr \} \ \times \int^{r} dr' \frac{f(r)}{k}\ exp\ \{ -\frac{m\omega}{\hbar}\int^{r'} \frac{1}{k}\,dr'' \} \ , \tag{16}$$

which is the equation to determine V and iW.

When f(r), the form factor of coupling potential, is assumed constant, the right-hand-side can be calculated analytically to give

$$V + iW - \frac{\hbar\omega}{2} = -\frac{\hbar^2}{2m}(\frac{f}{\hbar\omega})^2 \{ 1 - \exp\ (\frac{m\omega}{\hbar}\int_{b}^{r} \frac{1}{k}\,dr \} \ , \tag{17}$$

where the factor

$$-\frac{\hbar^2}{2m}(\frac{f}{\hbar\omega})^2 \ , \tag{18}$$

is the "adiabatic energy lowering".

5. Numerical Calculation

Numerical calculation of the integral equation by iteration method were performed. First guesses of V and W are inserted to the right-hand-side of Eq.(16) to calculate the second iterative solution. This procedure is continued till the solution converges to a definite value.

What was unexpected was that imaginary potential iW is identically zero when energy is below the real potential!!

We show in Fig.2 an example of real potentials for ^{58}NI + ^{58}Ni subbarrier fusion reaction. Center-of-mass energy is 93 MeV which is about 8 MeV below the fusion barrier for the system.

Solid line is the unperturbed potential, the dot-dashed line is the renormalization of the potential and the long dashed line is the total potential. The form factor of the coupling potential f(r) is shown in arbitrary unit by dotted line in the lower part of the figure. In this case, the total potential shows double-humped shape and in addition to the reduction of the barrier height, the position of the main peak shifts to larger distance. This fact may support the macroscopic neck-formation model [3] where the shift of the barrier position to larger distance occured in all cases treated.

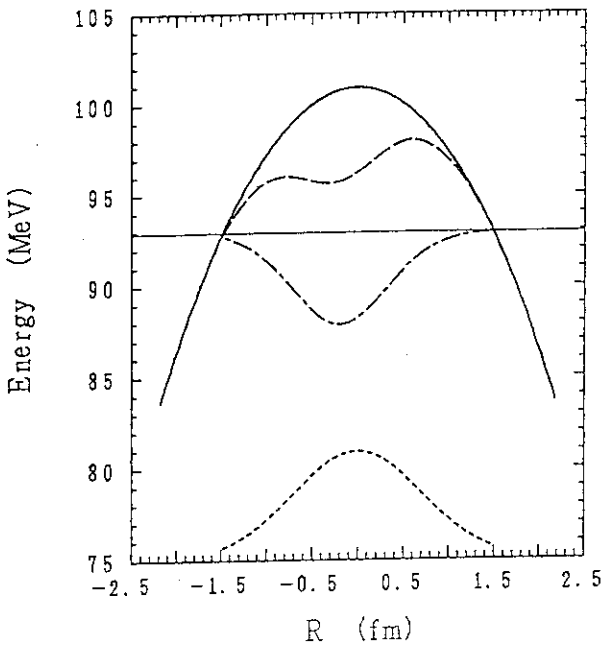

Fig.2

6. Summary

1) Induced potential is real and no imaginary component is induced. This means that in the classically forbidden region, imaginary potential which expresses real excitation of the intrinsic state never appears. On the other hand, real potential which expresses virtual excitation appears naturally.

2) Our method of potential renormalization calculation is very simple and reliable, which can be used to understand the qualitative feature of the subbarrier fusion cross section.

References

1) G.R. Satchler, N.A. Nagarajan and L.S. Lilley: Ann. Phys. 178 (1987) 110.

2) W.H. Louisell: Quantum Statistical Properties of Radiation (Wiley, New York, 1973).

3) A. Iwamoto and K. Harada: Z. Phys.A326 (1987) 201.

Ⅵ NEUTRON PHYSICS

6.1 MEASUREMENTS OF NEUTRONS GENERATED BY D INCIDENT ON THICK LI TARGETS

Masayoshi SUGIMOTO, Yoshimaro YAMANOUTI, Satoshi CHIBA, Kenji NODA*, Yoshio KATANO*, Kiyoyuki SHIBA*, Yoshio KATO*, Yukinobu WATANABE**

Department of Physics, JAERI, *Department of Fuels and Materials Research, JAERI, **Department of Energy Conversion Engineering, Graduate School of Engineering Sciences, Kyushu University

The energy and angular neutron production yields from the d+thick target at Ed=8,16,24, and 32 MeV were measured for natural Li metal and for the Li salt targets. For the lowest energy case, it was found that the molecular beam can provide the best quality of the pulsed deuteron beam. The results were compared with the simple models and the neutron energy profile and the energy integrated yield were well described by them.

Introduction

Energy Selective Neutron Irradiation Test Facility (ESNIT) proposed by JAERI can generate the high energy and high intensity neutron irradiation field for the materials researches[1]. The obtained neutron energy spectra can be varied by changing the incident deuteron energy of the d+Li neutron producing reaction, from 10 to 40 MeV. For the design studies of the facility, It is necessary to get the precise information about the neutron emission spectra from the d+Li reaction at these energies.

In the present work, we paid much attention on the "high energy tail" component (above 20 MeV) and the lower energy part (1–5 MeV region) of the neutron spectra, where the literatures show the inconsistent results.

Experiments

The experiments were carried out at the JAERI tandem accelerator using a high energy neutron time-of-flight spectrometer. The deuteron beam was produced by three methods: (*1*) a negative D^- ion source at the external injector deck (Ed=31.91 and 23.89 MeV), (*2*) a D^+ ion source at the terminal deck (Ed=15.86 MeV), and (*3*) a D_2^+ ion extraction using the same ion source as for the method (*2*) (Ed=7.77 MeV). For the lower energy

deuterons, the molecular beam acceleration provides the best results on the intensity and the quality of the pulsed beam(e.g. pulse width), because all accelerator columns should be used to gain the sufficient focusing force in the acceleration, and the particle of mass four (D_2^+) requires the lower bunching amplitude than that for D^+. These result in the stable operation and the good transmission through beam line.

Two targets were used: (a) a natural Li and (b) a Li salt (LiF $-BeF_2$ -NaF) melted into cylindrical containers (10mmϕ x 30mmL) in the argon atmosphere. The salt target was proposed by one of the authors (Y.KATO) to avoid the difficulties of the handling of the liquid lithium.

The neutron time of flight spectrometer has a 8 m flight path length with the platform rotatable from 0o to 140o, and the large volume neutron detector(VLD)s, filled with 10 ℓ NE213 liquid scintillator. In the present measurements, we used one of four VLDs to measure the neutrons with energies above 12 MeV, and a standard 2 in.ϕ x 2 in. NE213 detector, which was placed at 3 m flight length in the collimator shield, for the lower energy neutrons. The detection efficiencies of these detectors were calculated by the Monte Carlo simulation code. Since the calculated efficiency for the standard size detector, whose bias was set to 600keV, reproduces the absolute efficiency around 5MeV, we employed the yields obtained by the standard size detector as the absolute data. Those obtained by the VLD were normalized at 12MeV, above which energy the relative efficiency of VLD was relatively flat, up to 50MeV.

Seven data sets of the energy and angular distributions (Li metal at Ed=8,16,24,32 MeV and Li salt at Ed=16,24,32 MeV) were obtained for En=1 – 50 MeV and for θ=0° – 140°.

Results

Fig. 1 shows the results for Li metal at Ed=32 MeV and θ=0° – 140°. The bump at En=13 MeV is disappeared at θ=30° or larger angles. The lower energy part at 0° shows the rapid increase at En<3 MeV, however the accuracy of the results at these energies is worse than the other part. For the comparison of the high energy tail, fig. 2 shows the higher energy part at the forward angles. Above En=30 MeV, we found the angular distribution with the characteristic pattern of the L=1 stripping reaction $^7Li(d,n)^8Be(0^+;$ g.s. and $2^+;2.9)$. The total yield obtained from the Li salt target at Ed=32 MeV and θ=0° is about 1/3 of that for Li metal, due to its large contents of the higher Z elements. The high energy tail part shows

the rapid decrease above 35 MeV for the Li salt, where the main contribution comes from the $^{7}Li(d,n)^{8}Be$ reaction. Fig. 3 shows the energy integrated neutron yield for Li metal at all measured angles.

The energy integrated neutron yields at every deuteron energy are well represented by the simple formula: $Y = 3.2 \times 10^{3}\ Ed^{2.5}$, which is derived from the simple model analysis[2]. The energy profile for the deuteron breakup component can be predicted by two models: Serber model and the QuasiFree Scattering (QFS) model. The former model is usually used to interpret the d+thick target reaction yield, however it has inherent difficulty to represent the tail region. The QFS model shows the preferable profile when we suppose the appropriate phase space distribution. It is necessary to check for the energy profile using the thin target geometry.

Conclusion

The energy-and-angular distributions are measured at Ed=8,16,24, and 32 MeV for the thick natural Li target and at Ed=16,24, and 32 MeV for the $LiF-BeF_2-NaF$ salt. The neutrons with En=1 – 50 MeV were measured at $\theta=0^{\circ}$ – 140° with a step, 5° or 10°. We observed no excessive low Energy components referred in a few literatures, and the characteristic angular distribution at the high energy tail. The good prediction energy integrated yield with the function of deuteron energies can be derived by a simple model, such as Serber model. The energy profile may be represented by the Serber model, however the QFS model is preferred to analyze in details

References

1) T. Kondo et al., J.Fus.Energy 8,229(1989)
2) M.Sugimot et al., Proc. of Int. Panel on 14 MeV Intense Neutron Source based on Accelerators for Fusion Material Study, Jan. 14–16, 1991, Ed. by A.Miyahara and F.W.Wiffen, p.317.

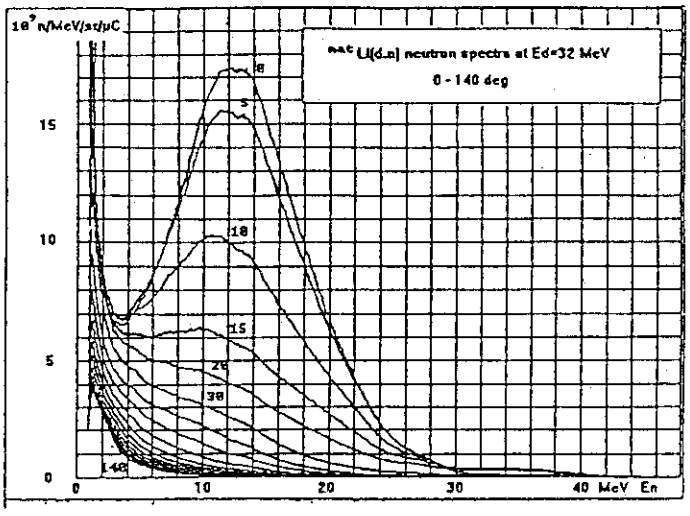

Fig. 1. The measured neutron energy spectra at 0 - 140 deg for $^{nat}Li(d,n)$ reaction, Ed=32 MeV.

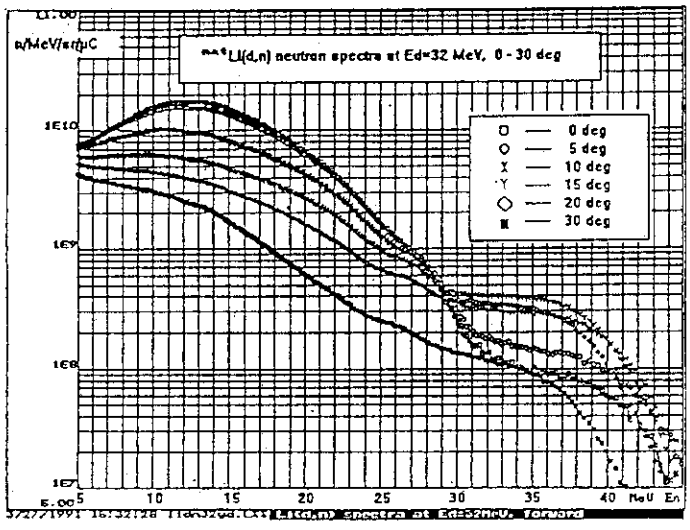

Fig. 2. The measured neutron energy spectra at 0 - 30 deg for $^{nat}Li(d,n)$ reaction, Ed=32MeV.

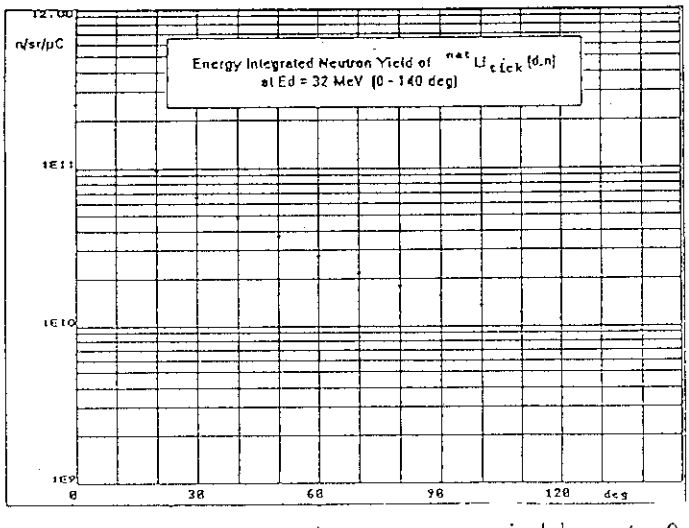

Fig. 3. The energy integrated neutron yields at 0 - 140 deg for $^{nat}Li(d,n)$ reaction, Ed=32MeV.

6.2 SCATTERING OF 18.5 MeV NEUTRONS FROM ^{60}Ni

Yoshimaro YAMANOUTI, Masayoshi SUGIMOTO, Motoharu MIZUMOTO, and Yukinobu WATANABE[A]

Department of Physics, JAERI, [A]Graduate School of Engineering Science, Kyushu University

Neutron scattering is of special interest for obtaining direct information on the nucleon-nucleus optical model potential and the collective nature of the target nucleus. In the energy region above 14 MeV, neutron scattering from ^{60}Ni has been studied only at energies of 14 MeV/1/ and 24 MeV/2/, therefore, there exists no experimental data in the energy range between these incident energies. In this work differential cross sections for elastic and inelastic scattering of neutrons from ^{60}Ni were measured at 18.5MeV, the mid point of the energy region of no data, in order to check the nucleon-nucleus optical model potential, direct reaction process of the neutron scattering and the collective nature of the target nucleus by means of the coupled-channel analysis. The experimental data obtained in this work were analyzed by the phenomenological optical model potential and the coupled-channel formalism, and compared with proton scattering in the framework of the Lane model.

The measurements were performed with pulsed beam time-of-flight method. A pulsed deuteron beam with repetition rate of 2MHz was provided by the JAERI tandem accelerator. Neutrons of 18.5 MeV were generated by the ^{2}H(d,n)^{3}He reaction. The ^{60}Ni scattering sample of 38.67g with 99.79% enrichment was used on loan from ORNL. Scattered neutrons were observed by four 20cmϕ x 35cm NE213 liquid scintillator detectors for efficient measurements. Fig.1 shows a time-of-flight spectrum for neutron scattering of ^{60}Ni taken at 60° .

The relative efficiency of the neutron detector was determined by measuring the angular distribution of the n-p scattering. Differential cross sections were determined for the elastic scattering and the inelastic scattering leading to the excited states at 1.332 MeV (2^{+}) and 4.045 MeV (3^{-}) of ^{60}Ni. The differential cross sections were measured in the angular

range from 20° to 140° in 10° steps at the incident energy of 18.5 MeV.The experimental cross sections are shown in fig.2 together with theoretical predictions.

The elastic scattering data were analyzed by the phenomenological optical model with the standard Woods-Saxon form. The compound nuclear contribution estimated by the Hauser-Feshbach formalism is small compared with the experimental cross sections at this incident energy.

The coupled-channel (CC) calculations based on the rotational model and the vibrational model were performed with the codes ECIS79 and JUPITOR1.In the CC calculations optical potential parameters and the deformation parameters were adjusted to get the best fit to the experimental cross sections for the elastic and inelastic scattering.The parameters for the spin orbit term were fixed in the calculations. The vibrational model calculations well reproduced the experimental cross sections for ^{60}Ni.The results of the CC calculations are shown in fig.2.

Proton optical potential obtained in the proton scattering for ^{60}Ni/3/ was transformed into neutron optical potential in the framework of the Lane model, and the ability to predict the present experimental neutron cross sections was checked in the CC calculations. The same deformation parameters as those obtained in the proton scattering were used in the calculations. The values of the energy dependence and the Coulomb correction term were adopted from the global optical potential.

The CC calculations based on the collective model well described the experimental elastic and inelastic scattering cross sections of neutrons from ^{60}Ni in this energy region, and the best fit optical model potential and the deformation parameters were obtained in the present analysis. The optical potential transformed from the proton potential gives good fit to the experimental neutron cross sections.

References

1. P.P.Guss et al: Nucl. Phys. A438, 187 (1985)
2. Y.Yamanouti et al: Proc.Int.Conf. on Nuclear Cross Sections for Technology, October 1979, Knoxville, TN, p.146, NBS SP 594 (1980)
3. E.Fabrici et al: Phys. Rev. C21, 844 (1980)

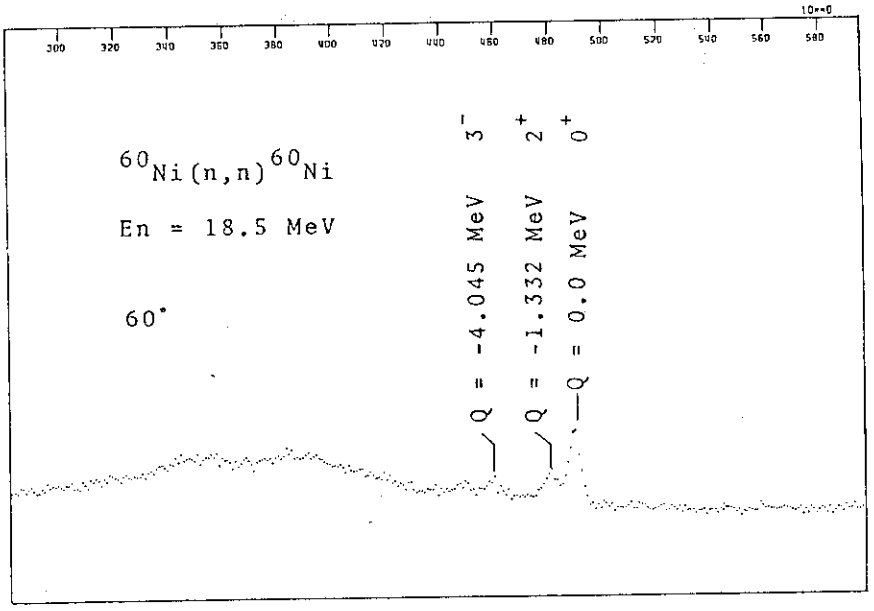

Fig.1 Time-of-flight spectrum for scattering of 18.5MeV neutrons from ^{60}Ni taken at 60°

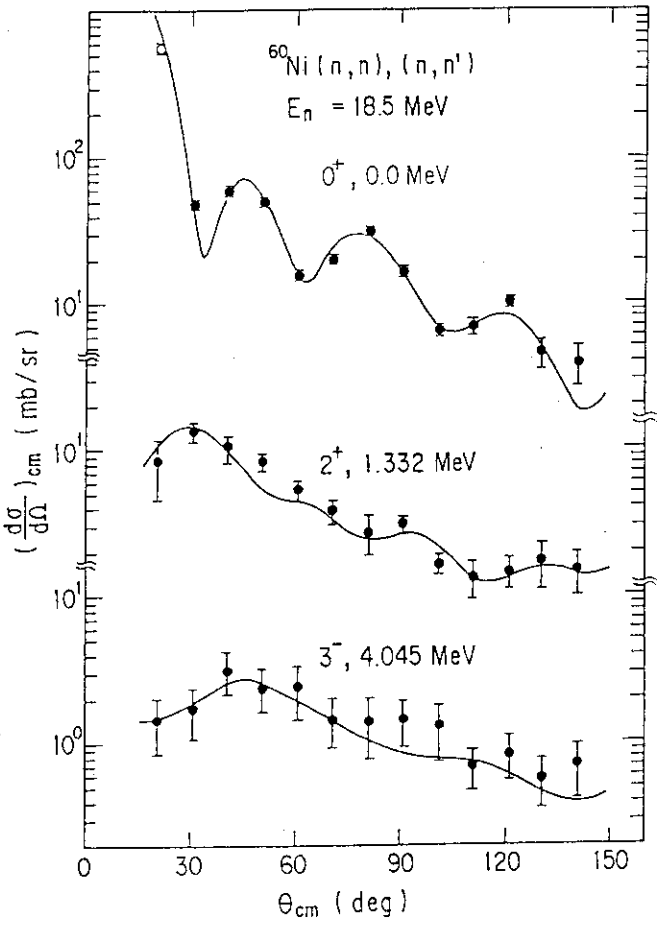

Fig.2 Experimental cross sections for ^{60}Ni and CC predictions based on the vibrational model. The 2^+ and 3^- states were treated as the quadrupole 1 phonon state and the octupole 1 phonon state, respectively, in the CC calculation.

6.3 MEASUREMENT OF DOUBLE DIFFERENTIAL CROSS SECTIONS OF 25.6 MEV (p,xp) and (p,xd) REACTIONS ON ^{98}Mo

Yukinobu WATANABE*, Akira AOTO*, Hiroki HANE*, Yukinori KANDA*, Yoshimaro YAMANOUTI, Masayoshi SUGIMOTO, Satoshi CHIBA

**Department of Energy Conversion Engineering, Graduate School of Engineering Sciences, Kyushu University, Department of Physics, JAERI*

Double differential cross sections of 25.6 MeV (p,xp) and (p,xd) reactions on ^{98}Mo were measured to investigate preequilibrium process in nucleon-induced reactions. The result of the exciton model calculation using the same parameters as those obtained from the analysis for 10-20 MeV region showed overestmation at forward angles for the (p,xp) reaction.

Introduction

In nuclear reactions induced by several tens of MeV nucleon, the contribution from preequilibrium process is observed in continuum spectra of particles emitted with forward-peaked angular distributions. Systematic measurements of double differential charged-particle emission cross sections have so far been performed for proton-induced reactions at 10 to 20 MeV in Kyushu University[1]. Through these experiments, the preequilibrium reaction mechanism has been investigated and the derived knowledge has been applied to the evaluation of neutron nuclear data based on nuclear model calculations.

In the present work, the incident proton energy range is extended to 20-40 MeV using JAERI tandem, and similar measurements of charged-particle spectra from proton-induced reactions are planned for further investigation of the preequilibrium process. Since (p,xn) spectra on Mo-isotopes have already been measured at 25.6 MeV[2], we have carried out measurement of double differential cross sections for the other exit channels (proton and deuteron) in p + ^{98}Mo reaction at the same incident energy. These measured (p,xp) and (p,xd) spectra are analyzed simultaneously on the basis of the preequilibrium model such as the exciton model and the SMD/SMC model.

Experimental Procedure

The experiment was performed using a 25.6 MeV proton beam from the JAERI tandem accelerator. The proton beam was transported in a scattering chamber 50 cm ϕ which was newly installed in N1 beam line. It was focused within about 2 mm ϕ on a target and its current was from about 50 nA to 150 nA. The beam intensity was monitored by means of a

current integrator connected to a Faraday cup. A target of ^{98}Mo was a self-supporting metallic foil whose thickness and enrichment were 0.45 mg/cm^2 and 97.1%, respectively.

A charged particle detecting system consists of a ΔE-E counter telescope of two silicon surface barrier detectors having thickness of 200 μm and 5000 μm, respectively. A defining aperture 2.5 mm in diameter was placed just in front of the ΔE detector and was located 147 mm from the target. The electronic equipments used were standard commercially available NIM modules. Each signal of emitted charged particles was separated by using a particle identifier module (MPS-1230). Energy spectra of emitted protons and deuterons were measured at six angles of 30°, 40°, 60°, 90°, 120°, and 150°.

Experimental result and preliminary analysis

Figure 1 shows a mass spectrum from the particle identifier MPS-1230. Each signal is separated quite well into proton, deuteron and triton. Pulse height spectra of proton and deuteron were recorded separately in a multichannel pulse height analyzer according to each gate signal generated from output of MPS-1230.

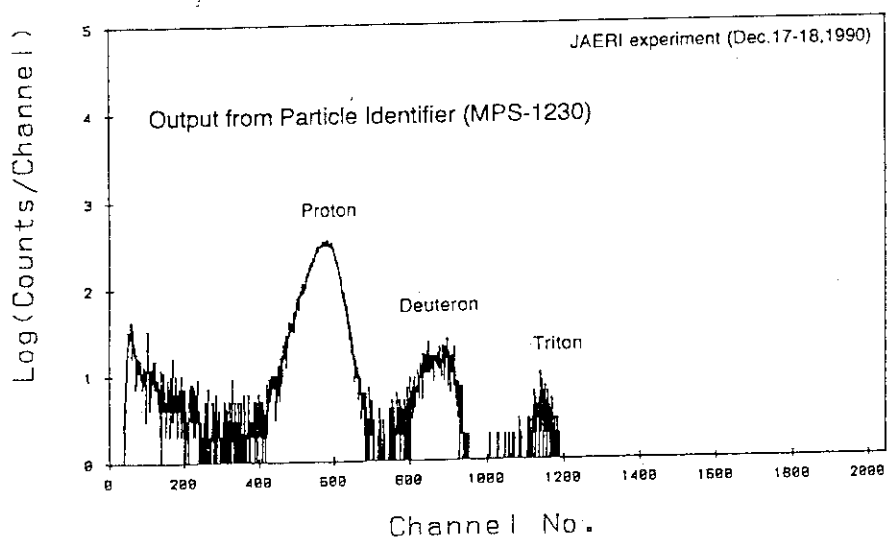

Fig.1 A mass spectrum from the particle identifier MPS-1230.

Measured double differential proton emission cross sections are shown for 40°, 90°, and 120° in Fig.2. The angular distributions are peaked forward in the continuum region between 10 and 20 MeV. This result suggests that the preequilibrium process or the direct process is dominant in this energy region. Figure 3 shows experimental energy spectra of deuterons emitted into 30°, 60°, and 120°. Strong forward-peaked angular distributions are observed at outgoing energies of 10 to 18 MeV. Bump structure are also exhibited around 15 MeV at the forward angle.

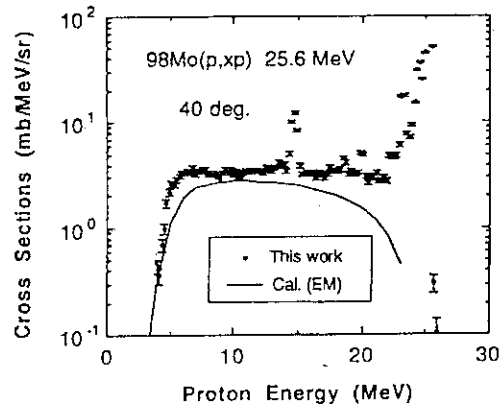

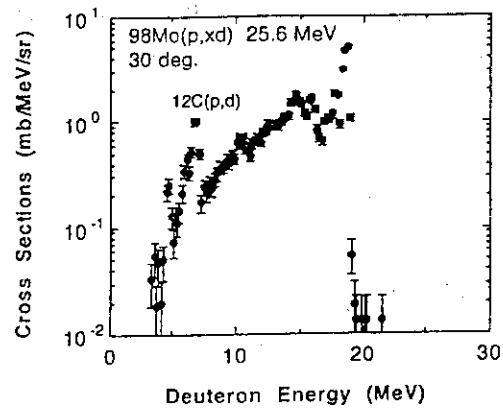

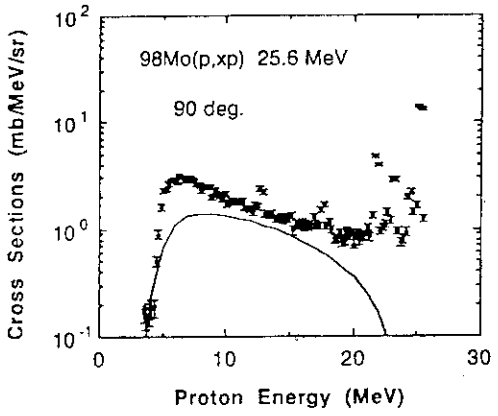

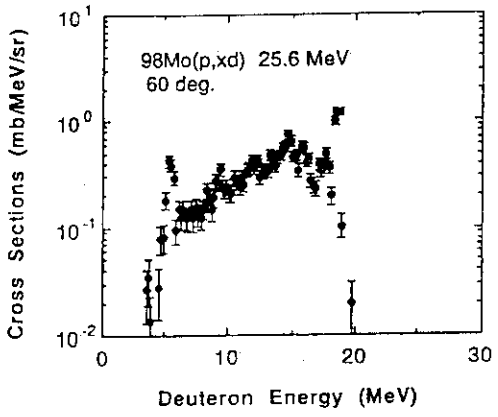

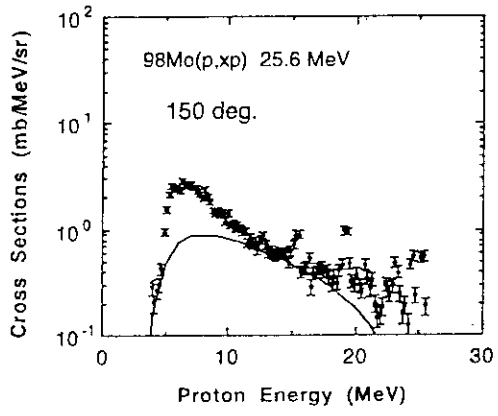

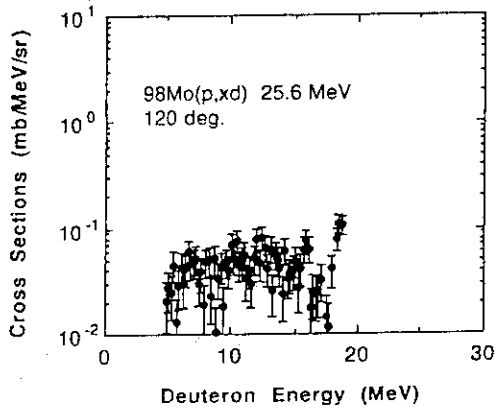

Fig.2 Comparisons of measured double differential proton emission cross sections for ^{98}Mo at 25.6 MeV and those calculated on the basis of the exciton model.

Fig.3 Measured double differential deuteron emission cross sections for ^{98}Mo at 25.6 MeV

The (p,xp) spectra were analyzed preliminarily on the basis of the exciton model in which isospin conservation was taken into account. The same model parameters as in our previous analysis[3] were employed and a modified version[4] of Kalbach -Mann systematics was applied to calculations of angle-dependent energy spectra. The calculated result is shown by solid lines in Fig.2. The calculated spectra underestimate the experimental ones for 40° and 90°. More detailed analyses on 25.6 MeV (p,xp) and (p,xn) spectra are now in progress.

Finally, the authors would like to thank the members of the accelerator division of JAERI for their kind help during the experiment.

References

1) Y. Watanabe et al., *Proceedings of the 1989 Seminar on Nuclear Data*, JAERI-M 90-025, p 216.
2) E. Mordhorst et al., Phys. Rev. C **34**, 103 (1986).
3) Y. Watanabe et al., Z. Phys. A **336**, 63 (1990).
4) I. Kumabe et al., Nucl. Scie. and Eng. **104**, 280 (1990).

Ⅶ PUBLICATION IN JOURNALS AND PROCEEDINGS

Publication in Journals and Proceedings

1. Abe, H., Kinoshita, C. and Nakai, K.
Accumulation Process of Cascades in Ceramics under Ion and/or Electron Irradiation
J. Nucl. Mater., 179 (1991) 399

2. Fukumoto, K., Kinoshita, C., Abe, H., Shinohara, K. and Kustuwada M.
Structure and Kinetic Behavior of Cascades in Copper under Ion and/or Electron Irradiation
J. Nucl. Mater., 179 (1991) 457

3. Gono, Y., Murakami, T., Kusakari, H., Oshima, M., Morita, K., Yoshida, A. and Kumagai, H
Isomer Decay of ^{136}Ce Studied by GARIS
RIKEN Accel. Progr. Rep. Vol. 24 (1990) p.20

4. Gono, Y., Oshima, M., Kusakari, H., Murakami, T. and Sugawara, M.
Coulomb Excitation of Unstable Nucleus ^{76}Kr
RIKEN Accel. Progr. Rep. Vol. 24 (1990) p.19

5. Haruna, K., Maeta, H.
Properties of Indium Phosphide 1.7 Thermal Expansion Coefficient of Inp (pp 16-7) (emis Datareviews Series No. 6 INSPEC Publication)

6. Hatsukawa, Y., Nakahara, H. and Hoffman, D.
Systematics of Alpha Decay Half-Lives
Phys. Rev. C42, 674 (1990)

7. Hoshiya, T., Takamura, S., Aruga, T. and Kobiyama, M.
Critical Current and Activation Energy in $Bi_2Sr_2Ca_1Cu_2O_x$ after Ion Irradiation
Jpn. J. Appl. Phys. 29 (1990) L2026.

8. Hoshiya, T., Takamura, S., Aruga, T. and Kobiyama, M.
Magnetic Flux Motion of Superconducting Bi-Sr-Ca-Cu-O Films after Ion Irradiation
Jpn. J. Appl. Phys. 29 (1990) L1443.

9. Ideno, K., Tomita, Y., Sugiyama, Y., Hanashima, S. and Nagame, Y.
A Two-Dimensional Position-Sensitive Detection System for the ^{8}Be Nuclei in Heavy Ion Reactions
Nucl. Instrum. and Methods A302 (1991) 385

10. Iimura, H., Nakahara, Y., Ichikawa, S., Kotani, K., Wakasugi, M. and Horiguchi, T.
Measurement of Hyperfine Structure of the $4F^{3}5d\ ^{5}G$-$4F^{3}6p\ ^{5}H$ in PrII by Collinear Laser-Ion-Beam Spectroscopy
J. Phys. Soc. Jpn. 59 (1990) 4208

11. Ikezoe, H., Shikazono, N., Nagame, Y., Sugiyama, Y., Tomita, Y., Ideno, K., Iwamoto, A. and Ohtsuki, T.
Pre-scission ^{4}He multiplicity in the ^{19}F+^{197}Au Reaction
Phys. Rev. C42 (1990) 342.

12. Ikezoe, H., Shikazono, N., Nagame, Y., Sugiyama, Y., Tomita, Y., Ideno, K., Iwamoto, A. and Ohtsuki, T.
Pre-scission ^{1}H and ^{4}He Emissions in ^{16}O+^{197}Au Reaction
Phys. Rev. C42 (1990) R1187

13. Iwamoto, A.
Evaporation of Charged particles in Fusion-Fission Reaction
Proc. Riken Symp. on Heavy-Ion Reaction (1991) 47

14. Iwamoto, A.
Subbarrier Fusion
Proc. Int. Conf. on Nuclear Reaction Mechanism Suppl. (1990) 96

15. Iwamoto, A.
Cluster Emission in Pre-Equilibrium Process
Proc. 1990 Symposium on Nuclear Data, JAERI-M 91-032 (1991) 91

16. Iwamoto, A.
Physics of Nuclear Fission : Present state and problems
Soryuushiron Kenkyuu 82 (1991) 401

17. Iwase. A.
Effect of High-Energy Ion Irradiation on Current-Voltage Characteristics in Oxide Superconductor $YBa_2Cu_3O_{7-x}$.
JAERI-M 91-050 p.97.

18. Iwase, A., Masaki, N., Iwata, T. and Nihira, T.
Effect of High-Energy Ion Irradiation on Current-Voltage Characteristics in Oxide Superconductor $YBa_2Cu_3O_{7-x}$.
Jpn. J. Appl. Phys. 29, (1990) L1810.

19. Iwase, A., Masaki, N., Iwata, T. and Nihira, T.
Effect of 120 MeV Oxygen Ion Irradiation on I-V Characteristics in YBaCuO.
Materials Research Society Symposia Proceedings (1991) in press.

20. Iwase, A., Masaki, N., Iwata, T. and Nihira, T.
Non-Ohmic Resistive State in Ion-Irradiated $YBa_2Cu_3O_{7-x}$.
Physica C174, (1991) 321.

21. Iwase, A., Iwata, T., Sasaki, S. and Nihira, T.
Radiation Annealing in Nickel and Copper by 100 MeV Iodine Ions.
J. Phys. Soc. Jpn. 59, (1990) 1451.

22. Iwase, A., Iwata, T., Nihira, T. and Sasaki, S.
Defect Recovery and Radiation Annealing in FCC Metals Irradiated with High Energy Ions.
Rad. Eff. and Defects in Solids (1991) in press.

23. Iwase, A., Iwata, T., Nihira, T. and Sasaki, S.
Defect Recovery in FCC Metals Irradiated with 0.5-126 MeV Energetic Ions.
Materials Science Forum (1991) in press.

24. Iwata, T. and Iwase, A.
Damage Production and Annealing in Ion-Irradiated FCC Metals.
Rad. Eff. and Defects in Solids 113, (1990) 135.

25. Iwata, T. and Iwase, A.
Radiation Annealing in Ni and Cu by Heavy Ion Irradiation.
Nucl. Instrm. Meth. (1991) in press.

26. Izumo, M., Matsuoka, H., Sorita, T., Nagame, Y., Sekine, T., Hata, K. and Baba, S.
Production of ^{95m}Tc with Proton Bombardment of ^{95m}Mo
Appl. Radiat. Isot. 42, 297 (1991)

27. Izumo, M., Sorita, T., Hata, K., Sekine, T., Matsuoka, H., Motoki, R. and Baba, S.
Production of ^{237}Pu and ^{236}Pu with ^{237}Np Targets
JAERI-M 90-102 (1990)

28. Izumo, M., Matsuoka, H., Sorita, T., Nagame, Y., Sekine, T., Hata, K. and Baba, S.
Production of ^{95m}Tc with the ^{95m}Mo (p, n) Reaction
JAERI-M 90-156 (1990)

29. Kanno, I.
A Model of Charge Collection Process in a Silicon Surface Barrier Detector
Proceedings of the Fifth Workshop on Radiation Detectors and Their Uses,
KEK Report 90-11

30. Kanno, I.
Candidate for Residual Defect in Silicon Surface Barrier Detector
J. Nucl. Sci. & Technol. 28 (1991) 87.

31. Kawatsura, K., Sataka, M., Yamazaki, Y., Komaki, K., Kanai, Y., Naramoto, H., Kuroki, K., Kanbara, T., Awaya, Y., Nakai, Y. and Stolterfoht, N.
Angular-Momentum Distribution of Autoionizing Rydberg States of 64 MeV S Ions Produced by Collisions with He and C Foils.
Nucl. Instrum. Meth. B48 (1990) 103

32. Kawatsura, K., Sataka, M., Naramoto, H., Nakai, Y., Komaki, K., Yamazaki, Y., Kuroki, K., Kanai, Y., Kambara, T., Awaya, Y., Hansen, J. E., Kadar, I. and Stolterfoht, N.
High Rydberg and Auger Electrons from Fast Projectile Ions Studied by Zero-Degree Electron Spectroscopy
Nucl. Instrum. & Methods B53 (1991) 421.

33. Kawatsura, K., Sataka, M., Yamazaki, Y., Komaki, K., Kanai, K., Naramoto, H., Kuroki, K., Kambara, T., Awaya, Y., Nakai, Y. and Stolterfoht, N.
Angular Momentum Distribution of Auto Ionizing Rydberg States of 64 MeV S Ions Produced by Collisions with He and C Foils
Nucl. Instrum. & Methods B48 (1990) 103.

34. Kinoshita, C.
Characteristics of Microstructural Evolution of Radiation Damage in Ceramics under Fusion Environment
J. Nucl. Mater., 179 (1991) 53

35. Mashiko, K., Shoji, T., Ishizaki, N., Tayama, H., Yokomizo, H. and SPring-8 Accelerator Group
Proceedings of the 15th Linear Accelerator Meeting in Japan
(September 11-13, 1990)

36. Murakami, T., Gono, Y., Oshima, M., Kusakari, H., Morita, K., Yoshida, A. and Kumagai, H.
Isomer Decay of ^{136}Ce Studied by Gas Filled Recoil Ion Separator
Journal of the Physical Sciety of Japan 60 (1991) 1424.

37. Nagame, Y., Sueki, K., Baba, S. and Nakahara, H.
Isomeric Yield Ratios in Proton-, ^{3}He-, and α-Particle-Induced Reactions on ^{197}Au
Phys. Rev. C41, (1990) 889

38. Nagame, Y., Ikezoe, H., Baba, S., Hata, K., Sekine, T., Ichikawa, S., Magara, M., Ideno, K., Yokoyama, A., Hatsukawa, Y. and Ohtsuki, T.
Statistical Emission of Complex Fragments Produced in the Reaction ^{37}Cl+^{68}Zn
Nucl. Phys. A510 (1990) 518

39. Nagame, Y., Ikezoe, Ohtsuki, T., Yokoyama, A., Hatsukawa, Y., Baba, S., Hata, K., Sekine, T. and Ideno, K.
Symmetric Mass Division Process in the Reactions ^{37}Cl+^{68}Zn and ^{16}O+^{89}Y
Phys. Lett. B249 (1990) 13

40. Nagame, Y., Ikezoe, H., Shikazono, H., Ohtsuki, T. and Nakahara, H.
Studies on Fission Phenomena Induced by Charged Particles Using the JAERI Tandem Accelerator
Nucl. Instr. Meth. B56/57 (1991) 511

41. Nakai, Y. and Sataka, M.
Electron Capture and Loss Cross Sections in Collisions of C Atoms with He.
J. Phys. B24 (1991) L89

42. Noda, K., Ishii, Y., Ohno, H., Watanabe, H. and Matsui, H.
Irradiation Effects on Ion Conductivity of Lithium Oxide
Advances in Ceramics, Vol. 27 (Am. Ceram. Soc., 1990) p.227-247

43. Noda, K., Ishii, Y., Matsui, H., Ohno, H. and Watanabe, H.
Electrical Conductivity of Li_2O under and after Irradiation
J. Nucl. Mater., (1991) in press.

44. Noda, K., Ishii, Y., Matsui, H., Vollath, D., Watanabe, H.
Irradiation Effects on Ionic Conductivity of Pure and Al-doped Li_4SiO_4
Proc. 16th Symposium on Fusion Technology

45. Ohtsuki, T., Nagame, Y., Ikezoe, H., Tsukada, K., Sueki, K. and Nakahara, H.
Binary Structure in Time Distributions of Fission Fragments in 13-MeV Proton-Induced Fission of ^{232}Th
Phys. Rev. Lett. 66 (1991) 17

46. Oshima, M., Inamura, T.
Rotational Perturbation to the Natural-Parity Rotational Bands of Deformed Odd Nuclei
Proceedings of Second IN2P3-RIKEN Sumposium on Heavy-Ion Collisions, edited by B. Heusch and M. Ishihara (World Scientific, 1990) p.287

47. Oshima, M., Kusakari, Sugawara, Inamura, T., Hashizume, A., Kumagai, H., Ichikawa, S. and Iimura, S.
γ-Vibrational States in ^{164}Dy
RIKEN Accel. Progr. Rep. Vol. 24 (1990) p.21

48. Oshima, M., Gono, Y., Murakami, T., Kusakari, H., Sugawara, M., Morita, K., Yoshida, A. and Kumagai, H.
Coulomb Excitation of Unstable Nucleus ^{76}Kr and Isomer Decay of ^{136}Ce
Genshikaku Kenkyu 35 (1991) p.161.

49. Sakae, H., Miyauchi, Y. and Mashiko, K.
Proceedings of the 15th Linear Accelerator Meeting in Japan
(September 11-13, 1990)

50. Sataka, M., Yagishita, A. and Nakai, Y.
Measurement of Charge-Changing Cross Sections in Collisions of He and He^+ with H_2, O_2, CH_4, CO and CO_2.
J. Phys. B23 (1990) 1225

51. Shinohara, N.
Radiochemical Investigation of Ttansuranium Nuclides produced by Heavy Ion Reaction
Proc. of International School-Seminar on Heavy Ion Physics, Dubna, USSR (Oct. 3-12, 1989), JINR-D-7-90-142 (1990) p.70-83.

52. Shinohara, N.
Solution Chemistry of Transactinide Elements in Extremely Dilute Solution Radioisotopes, 40 (1991) 7P.

53. Sugimoto, M., Yamanouti, Y., Chiba, S., Noda, K., Katano, Y., Shiba, K., Kato, Y. and Watanabe, Y.
Measurements of Neutrons Generated by D Incident on Thick Li Targets
Proc. of International Panel on 14 MeV Intense Neutron Source Based on Accelerators for Fusion Materia Study, held on Jan. 14-16, 1991, Tokyo. Ed. by A. Miyahara and F. W. Wiffen, NIFS-WS-2 (1991).

54. Sugiyama, Y.
Elastic Scattering of $^{58}Ni+^{90,94}Zr$ around the Coulomb Barrier
Proc. Riken Symp. on Heavy-Ion Reaction (1991) 87

55. Takeuchi, S., Ishii, T., Ikezoe. H., J. Min, B. and Booster Project Group
Superconducting Heavy-Ion Booster Linac at JAERI
Proc. of the 15th Meeting of Linear Accelerators, 11-13 Sep. 1990, Sapporo p23.

56. Takeuchi, S.
Superconducting Booster Linac for the JAERI Tandem
Proc. of the 4th China-Japan Joint Symposium on Accelerators for Nuclear Science and their Applications, 15-17 Oct. 1990, Beijin to be published.

57. Takeuchi, S., Ishii, T., Ikezoe, H., J. Min, B. and Booster group
Superconduеting heavy-ion booster linac at JAERI
Proceedings of the 15th Linear accelerator Meeting in Japan
Sep. 1990, Hokkaido, P.23∿25

58. Yamanouti, Y., Sugimoto, M., Mizumoto, M., Watanabe, Y. and Wakuta, Y.
Scattering of 18.5 MeV Neutrons from ^{52}Cr
JAERI-M 90-139 (1990) p.185

Contributions to Scientitic and Technical Meetings

1. Fujita, H., Kato, N., Sugimitsu, T., Funatsu, Y., Okamoto, T., Niiya, S., Sugiyama, Y., Ikezoe, H., Tomita, Y., Ideno, K., Kubono, S. and Tanaka, M.
   Elastic and Inelastic Scattering of $^{28}Si+^{19}F$ at $E_{lab}(^{19}F)$=120 and 155 MeV
   Spring Meeting of the Physical Society of Japan in Tokyo (Mar. 28, 1991)

2. Furukawa, K., Ohno, S., Namba, H., Komaki, Y., Yamada, Y. and Nakai, Y.
   Microdosimetry of High-energy Heavy Ions
   33th Annual Congress on Radiation Chemistry, Sendai (Oct. 8-9, 1990)

3. Hata, K., Nagame, Y. and Nakahara, H.
   Systematics on Isomeric Cross Section Ratio
   The 34th Symposium on Radiochemistry in Tokyo (Oct. 1-3, 1990).

4. Haruna, K., Maeta, H., Ohashi, K., Koike, T.
   Thermal Expansion Coefficients of Synthetic Diamond
   Fall Meeting of Japan Society of Applied Physics in Iwate (Sep. 26-29, 1990)

5. Hatsukawa, Y., Nakahara, H. and Hoffman, D.
   Systematics of Alpha Decay Half-Lives
   The 34th Symposium on Radiochemistry in Tokyo (Oct. 1-3, 1990)

6. Ichikawa, S. and Nakahara, Y.
   A Study of Nuclei far from Stability by JAERI ISOL
   Spring Meeting of the Physical Society of Japan in Tokyo (Mar. 24-27, 1991).

7. Ideno, K., Tomita, Y., Sugiyama, Y., Ikezoe, H., Hanashima, S. and Nagame, Y.
   ^{8}Be-α Decays from ^{12}C Nuclei Emitted in the $^{16}O+^{60}Ni$ Reaction
   Autumn Meeting of Physical Society of Japan in Nara (Sept. 30- Oct. 3, 1990)

8. Iimura, H., Nakahara, Y., Ichikawa, S., Kotani, K., Wakasugi, M. and Horiguchi, T.
Preparation of the Apparatus for Laser Spectroscopy at JAERI-ISOL.
Fall Meeting of the Physical Soceity of Japan in Nara.
(Sept. 30 - Oct. 3 in 1990)

9. Ikezoe, H., Nagame, Y., Shikazono, N., Sugiyama, Y., Tomita, Y., Ideno, K., Kanno, I. and Ohtsuki, T.
Emission Mechanism of Pre-scission ^{4}He Particles.
Spring Meeting of Physical Society of Japan in Tokyo (March 28, 1991)

10. Ishii, T., Ishii, M., Saito, Y., Nakajima, M., Ogawa, M. and Garnsomsart, S.
Ns-Isomevs in Neighbor Nuclei of ^{100}Sn
Autum Meeting of Physical Society of Japan in Nara (Oct. 1990)

11. Iwamoto, A.
Evaporation of Charged Particles from Highly Deformed Nucleus
RIFP Symposium on Low and Intermidiate Energy Nuclear Reaction Mechanism, in Kyoto (Sep. 27-29, 1990)

12. Iwamoto, A. and Herrmann, R.
Evaporation of Charged Particles from Highly Deformed Nucleus
Autumn Meeting of the Physical Society of Japan, in Nara (Sep. 30 - Oct. 3, 1990)

13. Iwamoto, A.
Multi-Dimensional Tunneling and Nuclear Fission
5-th Nishinomiya Yukawa-Memorial Symp. on Theoretical Physics, in Nishinomiya (Oct. 25-26, 1990)

14. Iwamoto, A.
Cluster Emission in Pre-Equilibrium Process
1990 Symposium on Nuclear Data, in Tokai (Nov. 29-30, 1990)

15. Iwamoto, A.
Evaporation of Charged Particles in Fusion-Fission Reaction
RIKEN Symp. on Heavy-Ion Nuclear Reactions, in Wako (Jan. 31 - Feb. 2, 1991)

16. Iwamoto, A. and Tomita, Y.
Adiabatic Assumption in Multi-Dimensional Tunneling Process
Spring Meeting of the Physical Society of Japan, in Tokyo (Mar. 27-30, 1991)

17. Iwase, A.
Effect of High Energy Ion Irradiation on Current-Voltage Characteristics in YBaCuO.
1990 Workshop on Plasma-Materials Interactions for Fusion Research in Tokyo (July 10-11, 1990).

18. Iwase, A., Masaki, N., Iwata, T. and Nihira, T.
Effect of Ion-Irradiation on I-V Characteristics in YBaCuO.
Fall Meeting of Physical Society of Japan in Gifu (Oct. 2, 1990).

19. Iwase, A., Iwata, T. and Nihira, T.
Electron-Excitation and Defect Production in High Energy Ion Irradiated Copper.
Fall Meeting of Physical Society of Japan in Gifu (Oct 5, 1990).

20. Iwase, A.
Effect of Electron-Excitation on Heavy Ion Irradiation Damage in Metals.
The 30th Meeting of Lattice Defects Forum in Inuyama
(Oct 7, 1990)

21. Iwase, A., Masaki, N., Iwata, T. and Nihira, T.
Effect of 120 MeV Oxygen Ion Irradiation on I-V Characteristics in YBaCuO.
Fall Meeting of Materials Research Society in Boston (Nov, 26-30, 1990).

22. Iwase, A.
High Energy Ion Irradiation of FCC Metals and High-Tc Superconductors.
ANL Materials Science Division Seminar (Dec 5, 1990)

23. Iwase, A., Iwata, T., Nihira, T. and Sasaki, S.
Defect Recovery in FCC Metals Irradiated with 0.5-126 MeV Energetic Ions.
International Conference on Physics of Irradiation Effects in Metals in Siofok (May 22, 1991)

24. Iwase, A.
High Energy (∿100 MeV) Ion Irradiation Damage in FCC Metals and High-Tc Superconductors.
CIRIL Seminar in Caen (May 16, 1991)

25. Iwata, T.
Status of the JAERI Tandem Accelerator.
International Conference on Application of Accelerator in Research and Industry in Denton (Nov. 5, 1990)

26. Iwata, T.
Radiation Annealing in Ni and Cu by Heavy Ion Irradiation.
International Conference on Application of Accelerator in Research and Industry in Denton (Nov. 8, 1990)

27. Iwata. T.
Defect Production, Radiation Annealing and Effects of Electron Excitation in Ion-Irradiation of Ni and Cu.
ORNL Solid State Division Seminar (Nov. 13, 1990)

28. Kanai, Y., Kanbara, T., Awaya, Y., Hvelplund, P., Sataka, M., Imai, W., Tawara, H., Kawatsura, K., Watanabe, H., Kuroki, K., Komaki, K. and Yamazaki, Y.
Binary Electron Production in Si^{q+} + He Collision.
Spring Meeting of the Physical Society of Japan in Tokyo (Mar. 24-27 1991)

29. Kanno, I.
On the Pulse Height Defect in a Silicon Surface Barrier Detector
1990 Annual Meeting of the Atomic Energy Society of Japan (Apr. 2-4, 1990).

30. Kanno, I., Ikezoe, H., Ohtsuki, T., Kanazawa, S., Hayashi, S. A. and Kimura, I.
Incident Angle Dependence of the Residual Defect in a Si Surface Barrier Detector
1991 Annual Meeting of the Atomic Energy Society of Japan (May. 28-30, 1991).

31. Kanno, I.
Dielectricity Effect in a Silicon Surface Barrier Detector
1990 Fall Meeting of the Atomic Energy Society of Japan (Oct. 2-5, 1990).

32. Maeta, H., Haruna, K.
Radiation Effects of Heavy Ion-Irradiated Synthetic Diamond by X-ray Measurements
Spring Meeting of Physical Society of Japan in Tokyo (Mar. 24-27 1991)

33. Murakami, T., Gono, Y., Oshima, M., Kusakari, H., Morita, K., Yoshida, A. and Kumagai, H.
γ Decay of 10^{+} Isomers in N=78 Isotones and Coulomb Excitation of Unstable Nuclei
Autumn Meeting of the Physical Sciety of Japan in Nara (Oct. 1990).

34. Niita, K.
Present Status of Intermediate and High Energy Heavy Ion Collisions
Riken Symposium on Heavy Ion Collisions in Wako (Jan. 31 - Feb. 2, 1991)

35. Niita, K.
Intermediate Heavy Ion Collisions
Seminar on Nuclear Physics at the Energy Region of the JAERI Tandem-Booster in Tokai (Feb. 28 - Mar. 1, 1991)

36. Niita, K.
Simulations for Intermediate Heavy Ion Collisions
Symposium on Super Computer Theoretical Physics in Kyoto (Mar. 18-20, 1991)

37. Noda, K., Ishii, Y., Matsui, H., Vollath, D., Watanabe, H.
Irradiation Effects on Ionic Conductivity of $Li_{3.7}Al_{0.1}SiO_4$
Spring Meeting of the Atomic Energy Society of Japan in Tokyo
(Apr. 2-4)

38. Noda, K., Ishii, Y., Matsui, H., Vollath, D. and Watanabe, H.
Irradiation Effect on Ion Conductivity of Al-Doped Li_4SiO_4
16th Symp. of Fusion Technology, in London (Sept. 3-7 1990)

39. Noda, K., Ishii, Y., Natsui, H., Vollath, D., Watanabe, H.
Irradiation Effects on Ionic Conductivity of Li_4SiO_4 and $Li_{3.7}Al_{0.1}SiO_4$
Autumn Meeting of The Atomic Energy Society of Japan in Sendai
(Oct. 2-4, 1991)

40. Noda, K., Ishii, Y., Matsui, H., Nakazawa, T., Watanabe, H., Vollath, D.
Evaluation of Irradiation Effects on Tritium Release from Li_4SiO_4 and $Li_{3.7}Al_{0.1}SiO_4$ by Ionic Conductivity Measurements
Spring Meeting of The Atomic Energy Society of Japan in Osaka
(Mar. 28-30, 1991)

41. Ohtsuki, T., Nagame, Y., Ikezoe, H., Tsukada, K., Nishinaka, I.,
Kanno, I., Magara, M., Sueki, K. and Nakahara, H.
Study of Mass Divission for Fission of Actinide
The 34th Symposium on Radiochemistry in Tokyo (Oct. 1-3. 1990)

42. Ohtsuki, T., Tsukada, K., Nishinaka, I., Sueki, k., Nakahara, H.,
Nagame, Y., Ikezoe, H., Magara, M. and Kanno, I.
Mass and Energy Distribution of Fission Fragments in the Proton-Induced Fission of Actinide
The 34th Symposium on Radiochemistry in Tokyo (Oct. 1-3, 1990).

43. Osa, A., Kotani, K., Shibata, M., Kawade, K., Yamamoto, H. and
Ichikawa, S.
Decay of $^{123,125}Ba$
Spring Meeting of the Physical Society of Japan in Tokyo
(Mar. 27-30. 1991).

44. Oshima, M., Inamura, T.
Rotational Perturbation to the Natural-Parity Rotational Bands of Deformed Odd Nuclei
Second IN2P3-RIKEN Sumposium on Heavy-Ion Collisions in Strasbourg (April 1990).

45. Oshima, M., Gono, Y., Murakami, T., Kusakari, H., Sugawara, M., Morita, K., Yoshida, A. and Kumagai, H.
Coulomb Excitation of Unstable Nucleus ^{76}Kr and Isomer Decay of ^{136}Ce
INS Workshop on Nuclear Structure at High Spin and High Excitation in Tokyo (November 1990).

46. Oshima, M.
Coulomb Excitation Experiments on Stable and Unstable Nuclei at JAERI Tandem
Spring Meeting of the Physical Sciety of Japan in Tokyo (March 1991).

47. Sugimoto, M., Yamanouti, Y., Watanabe, Y., Noda, K., Katano, Y. and Shiba, K.
Li (d, n) Neutron Spectra at Ed=8-32 MeV
Fall Meeting of Japan Atomic Energy Society in Sendai (October, 1990)

48. Sugimoto, M., Yamanouti, Y., Chiba, S., Noda, K., Katano, Y., Shiba, K., Kato, Y. and Watanabe, Y.
Measurements of Neutrons Generated by D Incident on Thick Li Targets
Spring Meeting of Japan Atomic Energy Society in Osaka (March, 1991)
T

49. Sugita, M. and Arima, A.
Shape Transition of Nuclei with Mass around A=100
Nuclear Physics in the 1990's
Symposium of Honor Akito Arima in Santa Fe (USA, May 1990)

50. Sugita, M.
α Decay and the spdf Boson Model, Kiken meeting in Kyoto (Aug. 1990)

51. Sugita, M.
Stabilization of Octupole Deformation due to Rotation
Fall meeting of Physical Society of Japan in Nara (Sep. 30, 1990)

52. Sugita, M.
The spdf Boson Model and α Decay
RCNP meeting in Osaka (Mar, 21-23, 1991)

53. Sugita, M.
Anomalous β band and the SPDF boson model
Fall meeting of Physical Society of Japan in Tokyo (Mar. 31, 1991)

54. Sugiyama, Y., Tomita, Y., Ikezoe, H., Ideno, K., Kato, N., Fujita, H. and Sugimitsu, T.
Transfer Reactions of $^{16}O+^{144,152}Sm$ near the Coulomb Barrier
Autumn Meeting of the Physical Society of Japan in Nara (Sep. 30, 1990)

55. Sugiyama, Y.
Elastic Scattering of $^{58}Ni+^{90,94}Zr$ around the Coulomb Barrier
Riken Symposium in Wako (Jan. 31 1991)

56. Sugiyama, Y.
Transfer Cross Sections of $^{16}O+^{144,152}Sm$ near the Coulomb Barrier
INS Symposium in Tokyo (Mar. 26, 1991)

57. Tsukada, K., Sueki, K., Ohtsuki, T., Kobayashi, T., Nishinaka, I., Nakahara, H., Shinohara, N., Ichikawa, S., Hoshi, M., Nagame, Y.
Mass Yield Distributions in Rare Earth Region Produced on Proton-Induced Fission of ^{244}Pu
The 34th Symposium on Radiochemistry in Tokyo (Oct. 1-3, 1990)

58. Yamanouti, Y., Sugimoto, M., Mizumoto, M., Watanabe, Y. and Hasegawa, K.
$^{52}Cr(n, n)$, (n, n') Reactions II
Spring Meeting of Physical Society of Japan in Osaka (Apr. 1, 1990)

59. Yamanouti, Y., Sugimoto, M., Mizumoto, M. and Watanabe, Y.
$^{60}Ni(n, n)$, (n, n') Reactions at 18.5 MeV
Fall Meeting of Physical Society of Japan in Nara (Oct. 3, 1990)

60. Yamanouti, Y., Sugimoto, M., Mizumoto, M. and Watanabe, Y.
Neutron Global Optical Model Potentials
Spring Meeting of Atomic Energy Society of Japan in Osaka (Mar. 30, 1991)

VIII PERSONNEL AND COMMITTEES

(April 1990－March 1991)

(1) Personnel

Department of Physics

	Mitsuhiko	Ishii	Deputy Director
	Fujiyasu	Nomura	Administrative Manager

Accelerators Division

Scientific Staff	Chiaki	Kobayashi*
	Shiro	Kikuchi
	Suehiro	Takeuchi
	Susumu	Hanashima
Technical Staff	Yutaka	Sato
(Tandem, V.D.G)	Tadashi	Yoshida**
	Susumu	Kanda
	Katsuzo	Horie
	Yoshihiro	Tsukihashi
	Shinichi	Abe
	Shuhei	Kanazawa
Technical Staff	Katuo	Mashiko**
(Linac)	Tokio	Shoji
	Nobuhiro	Ishizaki
	Hidekazu	Tayama

Nuclear Physics Laboratory

Scientific Staff	Akira	Iwamoto*

* Head

** Leader, Technical Staff

Nuclear Physics Laboratory (continued)

Scientific Staff	Yasuharu	Sugiyama
	Yoshiaki	Tomita
	Hiroshi	Ikezoe
	Masumi	Ohshima
	Kazumi	Ideno
	Tetsuro	Ishii
	Michiaki	Sugita

Linac Laboratory

Scientific Staff	Yuuki	Kawarasaki*
	Makio	Ohkubo
	Eisuke	Minehara
	Yoshimaro	Yamanouchi
	Masayoshi	Sugimoto
	Satoshi	Chiba
	Ryoji	Nagai
	Masayuki	Takabe
	Jyun	Sasabe
	Masaru	Sawamura

Solid State Physics Laboratory I

Scientific Staff	Yukio	Kazumata*
	Hiroshi	Naramoto
	Hiroshi	Tomimitsu

Solid State Physics Laboratory II

Scientific Staff	Tadao	Iwata*
	Saburo	Takamura
	Akihiro	Iwase

* Head

Atomic and Molecular Physics Laboratory

Scientific Staff	Hiroshi	Maeta
	Masao	Sataka
	Makoto	Imai

Department of Chemistry

Nuclear Chemistry Laboratory 1

Scientific Staff	Masakatus	Saeki*
	Yasuyuki	Aratono
	Mikio	Nakashima

Nuclear Chemistry Laboratory 2

Scientific Staff	Michio	Hoshi*
	Shin-ichi	Ichikawa
	Nobuo	Shinohara
	Hidenori	Iimura

Analytical Chemistry Laboratory

Scientific Staff	Yuji	Baba
	Toshio	Suzuki

Physical Chemistry Laboratory

Scientific Staff	Mutsuhide	Komaki
	Jiro	Ishikawa

Solid State Chemistry Laboratory

Scientific Staff	Teikichi	Sasaki*
	Shigemi	Furuno
	Takeshi	Soga

Laser Chemistry Laboratory

Scientific Staff	Shin-ichi	Ohno*
	Katsutoshi	Furukawa

* Head

Department of Radioisotopes

Isotope Research and Development Division

Scientific Staff	Hiromitsu	Matsuoka
	Kentaro	Hata
	Toshiaki	Sekine
	Yuichiro	Nagame
	Takami	Sorita
	Mishiroku	Izumo
	Hiroyuki	Sugai

Department of Fuels and Materials Research

Radiation Effects and Analysis Laboratory

Scientific Staff	Akimichi	Hishinumua*
	Takeo	Aruga
	Shozo	Hamada
	Tomotsugu	Sawai
	Katsumaro	Fukai

Material Processing and Qualification Laboratory

Scientific Staff	Hitoshi	Watanabe*
	Kenji	Noda
	Yoshinobu	Ishii

Department of Reactor Engineering

Thermal Reactor paysics Laboratory

Scientific Staff	Ikuo	Kanno

* Head

Department of Health Physics

Radiation Control Division II

Technical Staff	Shoji	Izawa*
	Kenji	Yamane
	Masamitsu	Kikuchi
	Akihiko	Kuramochi

* Chief

(2) Tandem Steering Committee

(Chairman)	Naomoto	Shikazono	(Deputy Director General, Yokai Research Estanblishment)
	Toru	Hiraoka	(Deputy Director, Department of Reactor Engineering)
	Tatuo	Kondo	(Director, Department of Fuels and Materials Research)
	Mitsuhiko	Ishii	(Deputy Director, Department of Physics)
	Enzo	Tachikawa	(Director, Department of Chemistry)
	Susumu	Shimamoto	(Director, Department of Thermonuclear Fusion Research)
	Hirokazu	Umezawa	(Director, Department of Radioisotopes)
(Secretary)	Chiaki	Kobayashi	(Head, Accelerators Division)
(Secretary)	Fujiyasu	Nomura	(Administrative Manager, Department of Physics)

(3) Tandem Consultative Committee

(Chairman)	Takumi	Asaoka	(Director General, Tokai Research Establisnment)
(Vice Charman)	Naomoto	Shikazono	(Deputy Director General, Tokai Research Establishment)
(Vice Chairman)	Mitsuhiko	Ishii	(Deputy Director, Department of Physics)
	Hiromichi	Kamitsubo	(Principal Scientist, Institute of Physical and Chemical Research)
	Koji	Nakai	(Professor, National Laboratory for High Energy Physics)
	Hiroyasu	Ejiri	(Professor, Osaka University)
	Shiori	Ishino	(Professor, University of Tokyo)
	Hiroyuki	Tawara	(Associate Professor, Institute of Plasma Physics, Nagoya University)
	Kohzoh	Masuda	(Professor, University of Tsukuba)
	Shiro	Iwata	(Professor, Kyoto University)
	Ichiro	Fujiwara	(Professor, Otemon Gakuin University)
	Kenji	Sumita	(Professor, Osaka University)
	Naohiro	Hirakawa	(Professor, Tohoku University)
	Hirosuke	Yagi	(Professor, University of Tsukuba)
	Syunpei	Morinobu	(Associate Professor, Research Center for Nuclear Physics Osaka University)
	Hiromichi	Nakahara	(Professor, Tokyo Metropolitan University)
	Sadaei	Yamaguchi	(Professor, The Research Institute for Iron, Steel and other Merals, Tohoku University)
	Nobutsugu	Imanishi	(Associate Professon, Kyoto University)
	Mamoru	Akiyama	(Professor, University of Tokyo)
	Yasuo	Ito	(Associate Professor, University of Tokyo)

(Secretary)	Chiaki	Kobayashi	(Head, Accelerators Division)
(Secretary)	Fujiyasu	Nomura	(Adiministrative Manager, Department of Physics)
(Secretary)	Hirokazu	Umezawa	(Director, Department of Radioisotopes)
(Secretary)	Tadao	Iwata	(Head, Solid State Physics Laboratory II)
(Secretary)	Hitoshi	Watanabe	(Head, Material Processing and Qulification, Depertment of Fuels and Materials Research)

(4) Tandem Program Advisory Committee

(Chairman)	Mitsuhiko	Ishii	(Deputy Director, Department of Physics)
	Hirokazu	Umezawa	(Director, Department of Radioisotopes)
	Shoji	Izawa	(Chief, Radiantion Contorol Group, Department of Health Physics)
	Hitoshi	Watanabe	(Head, Material Processing and Qualification Laboratory)
	Hiroshi	Maeta	(Head, Atomic and Molecular Physics Laboratory, Department of Physics)
	Yuuki	Kawarasaki	(Head, Linac Laboratory, Department of Physics)
	Akira	Iwamoto	(Head, Nuclear Physics Laboratory)
	Yukio	Kazumata	(Head, Solid State Physics Laboratory I)
(Secretary)	Chiaki	Kobayashi	(Head, Accelerators Division, Department of Physics)
(Secretany)	Shiro	Kikuchi	(Accelerators Division, Department of Physics)
(Secretany)	Tadashi	Yoshida	(Accelerators Division, Department of Physics)

IX CO-OPERATIVE RESEARCHES

	Title	Contact person Organization
1.	Gamma-Ray Spectroscopy in the Neibour Nuclei of ^{100}Sn	Masao OGAWA Tokyo Institute of Technology
2.	Study of Reaction Mechanism Induced by Heavy Ions	Toru NOMURA Institute for Nuclear Study, University of Tokyo
3.	Study of Nuclear Interactions in Heavy-Ion Reaction	Takao NAKAJIMA Department of Physics, Kyushn University
4.	Theoretical Investigation of Nuclear Fission and Heavy-Ion Fusion Reaction	Noboru TAKIGAWA Department of Physics, Tohoku University
5.	Nucear Structure Analysis Based on the Interacting Boson Model	Takaharu OTSUKA Department of Physics, University of Tokyo
6.	Study of Higher-Order Effect in Nuclear Collective Motion through Coulomb Excitation	Hideshige KUSAKARI Faculty of Education, Chiba University
7.	A Development of Collimated Neutron Source and Its Application to a Study of Neutron Reaction Cross Sections	Kazusuke SUGIYAMA Faculty of Engineering, Tohoku University
8.	A Study of Fast-Neutron Induced Gamma-Ray Producrtion Cross Sections	Hideo KITAZAWA Research Laboratory for Nuclear Reactors, Tokyo Institute of Technology
9.	Basic Research on Free Electron Laser	Hirotada OHASHI Faculty of Engineering, University of Tokyo
10.	Irradiation Effect on Electrical Property of LiAl with Li and Other Heavy Ions.	Kazuo KURIYAMA Research Center of Ion Beam Technology, Hosei University.
11.	Surface Analysis of Functional Materials with High Energy Ions.	Sadae YAMAGUCHI Institute for Material Research, Tohoku University.

12.	Radiation Damage of Materials for Enviroment Resistance Devices.	Kazutoshi OHASHI Faculty of Engineering, Tamagawa University.
13.	Study of Ion-Irradiation Damage in Metals by Megnetic Method	Fumihisa ONO College of Liberal Arts and Science, Okayama University.
14.	Interaction Between Radiation Defects and Hydrogen Atoms in Metals.	Kohji YAMAKAWA Faculty of Engineering, Hiroshima University.
15.	Structure of Tracks and Cascades in Inorganic solids.	Chiken KINOSHITA Faculty of Engineering, Kysushu University.
16.	Atomic Collision Research Using Highly Charged Ions.	Ken-ichiro KOMAKI Institute of Physics, College of arts and Sciences, University of Tokyo.
17.	Ion-Beam Analysis of Fusion Reactor Materials.	Michitaka TERASAWA Faculy of Engineering, Himeji Institute of Technology.
18.	Mass Division Processes in Fissions of Actinide Elements.	Hiromichi NAKAHARA Faculty of Science, Tokyo Metropolitan University.
19.	A Research for the Production of Transuranium Elements.	Ichiro FUJIWARA Faculty of Economy, Otemon Gakuin University.
20.	A Study of Irradiation Behavior of Ceramic Breeders.	Hisayuki MATSUI Faculty of Engineering, Nagoya University.
21.	Study on Continuous Spectra of Emitted Particles Induced by 20-40 MeV Protons	Yukinori KANDA Departneut of Energy Conversion Engineering, Kyushu University.
22.	Giant Resonance in Highly Excited Nuclei	Jirouta KASAGI Department of Physics, Tokyo Institute of Technolegy
23.	Heavy-Ion Nuclear Reactions Near the Coulomb Barrier	Yoshihiro TAGISHI Department of Physics University of Tsukuba

24.	Response of Semiconductor Detectors on Heavy Ions	Itsurou KIMURA Faculty of Engneering, Kyoto University
25.	Radiation Effects of High T_c Materials	Hiroaki KUMAKURA National Research Institute for Metals